ELECTRON ATTACHMENT REACTIONS AND PHOTOCHEMISTRY OF TRANSITION METAL CARBONYLS IN THE GAS PHASE AND ON SURFACES.

Thesis by

Patricia Margaret George

In Partial Fulfillment of the Requirements

For the Degree of

Doctor of Philosophy

California Institute of Technology

Pasadena, California

1981

(Submitted October 23, 1980)

Dedicated to

Mum and Dad

Thanks for everything

ACKNOWLEDGMENTS

I would like to thank Glenn for all the support and encouragement he has given me throughout the years. Without him this thesis would not have been possible. Thanks, also, to Jack Beauchamp for his patience, encouragement and good cooking over the last four years. He has provided more than a firm foundation for all future research.

Thanks are also due to Harry Gray, Henry Weinberg, Ken Janda and Peter Dervan for providing stimulating and useful discussions at all times. I also appreciate the many graduate students who shared conversations and good times with me while at Caltech. This is especially true for all past and present members of the Beauchamp group. Thank you all very much.

I would like to thank Marc Nicolet, Jim Mayer and members of their group in Steele for their help in understanding Rutherford backscattering. I appreciate the use of the Kellogg Radiation Laboratory to carry out my experiments. Thanks also goes to the ESCA laboratory at JPL especially Paula Grunthaner who spent much time helping me.

I greatly appreciate the help from all the people in the Chemistry Department shops, especially Tom Dunn, Tony Stark, Bill Schuelke and Erich Siegel.

Last, but not least, I thank Henriette Wymar for her superb typing of this thesis.

Abstract

Mechanistic studies of photoassisted and electron-assisted deposition of thin metal films, from organometallic compounds at low pressures have been carried out. Various types of spectroscopy and microscopy are used to characterize the complex processes occurring during film formation. Chapter I gives an introduction emphasizing the importance of such an approach.

Chapter II details some of the experimental methods used in this study. The three major techniques which were used to evaluate metal films deposited in this manner were Rutherford backscattering spectrometry, X-ray photoelectron spectroscopy and energy dispersive X-ray microprobe analysis. A summary of the methodology associated with each is given and background information is supplied for necessary measurements and calculations.

Chapter III details the photoassisted mechanism which involves three stages: initiation, propagation and termination of film growth. Initiation is thought to occur primarily by the formation and subsequent reaction of photoelectrons and by photodecomposition. At low pressures formation and reaction of photoelectrons probably dominates while at higher pressures photodecomposition becomes increasingly important. The organometallic compounds are thought to react with electrons by dissociative electron capture, forming negative ions that decompose further to produce thin metal films. Propagation appears to involve a thermally active catalyst capable of effecting a number of turnovers in the dark before termination occurs. The limiting step appears to be

loss of remaining CO ligands and the metal species is on the surface.

Chapter IV examines the dissociative electron attachment reactions of transition metal carbonyls. Dissociative electron attachment rates are measured for the transition metal carbonyls $V(CO)_6$, $Cr(CO)_6$, $Fe(CO)_5$, $Ni(CO)_4$, $Mo(CO)_6$ and $W(CO)_6$. Rates are measured as a function of the pressure of CO_2 added to relax epithermal electrons. Derived thermal rate constants for the process $M(CO)_n \rightarrow M(CO)^-_{n-1} + CO$ are 0.6, 3.0, 2.0, 2.0, 1.3 and 1.2×10^{-7} cm^3 $molecule^{-1}$ s^{-1}, respectively. The differences in these rate constants may be attributed to the different stabilities of the molecular anion with regard to dissociation versus autodetachment. The measured rate of thermalization of electrons by CO_2 varies with the metal carbonyl used and depends on the variation of the dissociative electron capture cross section with electron energy. Each system is thus tightly coupled in that the electron energy distribution is determined not only by collisional processes involving CO_2 but varies as well with the energy dependent depletion of the distribution by reactant species.

TABLE OF CONTENTS

CHAPTER I

Introduction

Introduction

With the advent of microcircuits and the rapid growth in semiconductor devices interest in thin film deposition has grown enormously. Over the last few years the major challenge has been to deposit films with ever decreasing dimensions,[1] to do this routinely and then to try to reduce the size even further. Until now, most of the work has been empirical, in that many of the deposition processes are only well understood from the viewpoint of how well they work. Recently, however, basic research in these areas has begun to catch up with known deposition processes. The physics of these techniques, especially, is being examined. Currently, adsorption,[2] nucleation,[3] film growth and interfacial phenomena[4] are areas where the increase in knowledge over the last decade appears to be almost exponential. The chemistry of such processes, however, is not well studied. This is true even for depositions achieved via chemical reactions. Moreover, chemists are generally not exposed to such problems with the result that few have interest in entering the field of thin film research.

With this in mind, we attempted to approach thin film deposition processes from a new vantage point. As physical chemists, with a knowledge of gas phase reactions we proposed a new technique for depositing thin metal films at room temperature. This technique involves the generation of low energy electrons on a surface and their subsequent reaction with organometallic compounds. The organometallic compounds were hypothesized to form reactive intermediates which would be capable of strongly interacting with the surface to form a thin metal film on the surface. The electrons could be generated in a number

of ways. They could be formed in a low energy electron gun and beamed to the surface, formed on the surfaces as photoelectrons by the photoelectric effect or created as secondary electrons from a high energy electron beam.

Once deposition was achieved the mechanistic pathways by which it occurred were of interest. In an attempt to understand the overall processes involved, combinations of both gas phase metal carbonyl electron attachment reactions and photochemistry were studied. It was necessary to use techniques and experimental procedures from several areas of chemistry in order to provide the necessary information. This thesis, therefore, comprises the results from deposition experiments and from other experiments carried out in order to gain some insight into the mechanism of that process.

References

1. For example see A. N. Broers, W. W. Molzen, J. J. Cuomo and N. D. Wittels, App. Phys. Lett. 29(9) 596 (1976).
2. A. Clark, "The Theory of Adsorption and Catalysis", Academic Press, New York (1970).
3. B. Lewis and J. C. Anderson, "Nucleation and Growth of Thin Films", Academic Press, New York (1978).
4. Proceedings of the Symposium on Thin Film Phenomena - Interfaces and Interactions, J. E. Baglin and J. M. Poate, eds. The Electrochemical Soc., Princeton, New Jersey (1978).

CHAPTER II

Experimental Techniques

EXPERIMENTAL TECHNIQUES

Three major experimental techniques were used to evaluate metal films deposited by photoassisted decomposition of organometallic compounds. These are Rutherford backscattering spectrometry, X-ray photoelectron spectroscopy and energy dispersive X-ray microprobe analysis. This last technique is used in conjunction with scanning electron microscopy. Film deposition and a mechanistic study of the photoassisted process is described in Chapter III.

Each of the above techniques provides different, complementary information about the depth of the film and its composition. Rutherford backscattering spectrometry reflects the number of atoms per square centimeter in the film. Direct conversion to a depth measurement can easily be made if the atomic density of the sample is known. It is necessary to know the composition of the film in order to determine the atomic density. Energy dispersive X-ray microprobe analysis provides this knowledge. In addition, the scanning electron microscope can be used to identify the surface topography of a film. X-ray photoelectron spectroscopy in this case is used for chemical analysis of the species present. Oxidation states of the metals can be deduced from this and the presence of impurities detected. In addition, lighter elements, which can not be identified with the other techniques (for example, carbon and oxygen) can be monitored. These three methods are discussed further below.

1. Rutherford Backscattering Spectrometry

a) General Principles

Figure 1[1] shows a schematic of a backscattering spectrometer similar to the one in Kellogg Radiation Laboratory. A backscattered spectrum is obtained by allowing a beam of monoenergetic, collimated ^4He ions to impinge on a target. Charged particles, generated in an ion source, are accelerated to several MeV by a van der Graaff. The beam is collimated and filtered for a specific particle and energy. It enters a scattering chamber, which is at approximately 10^{-6} Torr, and impinges on the sample. If the sample is thick the majority of $^4He^+$ come to rest in the sample. However, those particles that are scattered backwards by angles greater than 90° can be detected. A silicon barrier detector can be used to energy analyze the backscattered particles and a spectrum of yield versus energy can be obtained. The target chamber and electronics are illustrated in Figure 2.

All of the samples in these experiments are of films composed of one or more metals on a soda-lime glass substrate. The beam consists of $^4He^+$ particles at 1.5 MeV.

The $^4He^+$ particles strike the sample and undergo elastic collisions. The kinematic ratio, K, of the projectile energy before and after collision, can be solved exactly for a particular scattering angle. There is a certain probability that a collision will result in a detected particle. This is found by integrating differential scattering cross-sections over the field of view of the detector and summing the scattering cross-section over all the atoms in a layer. The scattering probability

FIGURE 1. Schematic diagram of a typical backscattering spectrometry system. (Permission to reproduce has been requested from Publishers.)

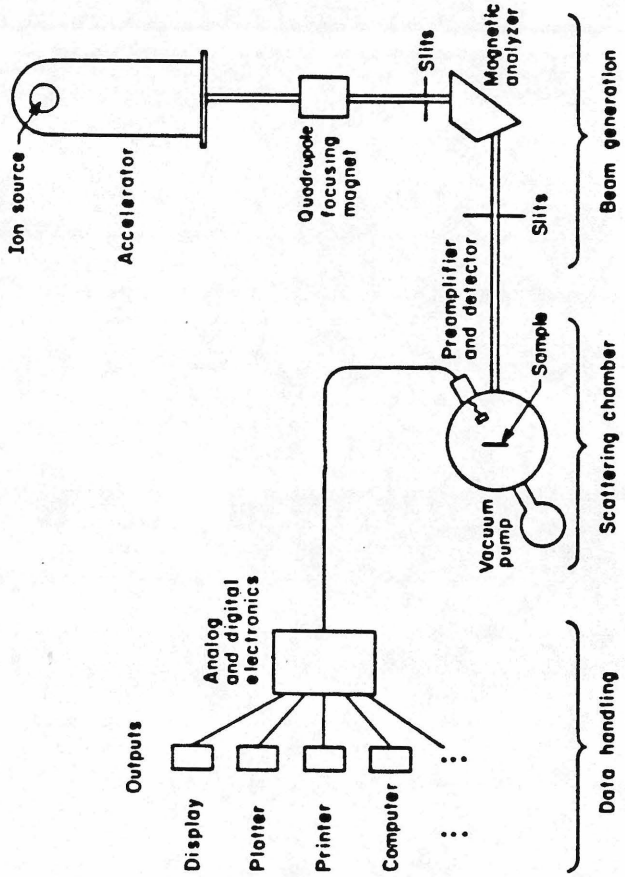
Ion source
Accelerator
Quadrupole focusing magnet
Slits
Magnetic analyzer
Slits
Beam generation
Preamplifier and detector
Sample
Vacuum pump
Scattering chamber
Analog and digital electronics
Outputs
Display
Plotter
Printer
Computer
Data handling

FIGURE 2. Layout of the target chamber and electronics of a backscattering system. The ions impinge on the target in the vacuum chamber. Backscattered particles are analyzed by the detector, and the detector signal is magnified and reshaped in the preamplifier. The electronic equipment in the rack provides power to the detector and preamplifier and stores the data generated by the detector in the form of the backscattering spectra. (Permission to reproduce has been requested from Publishers.)

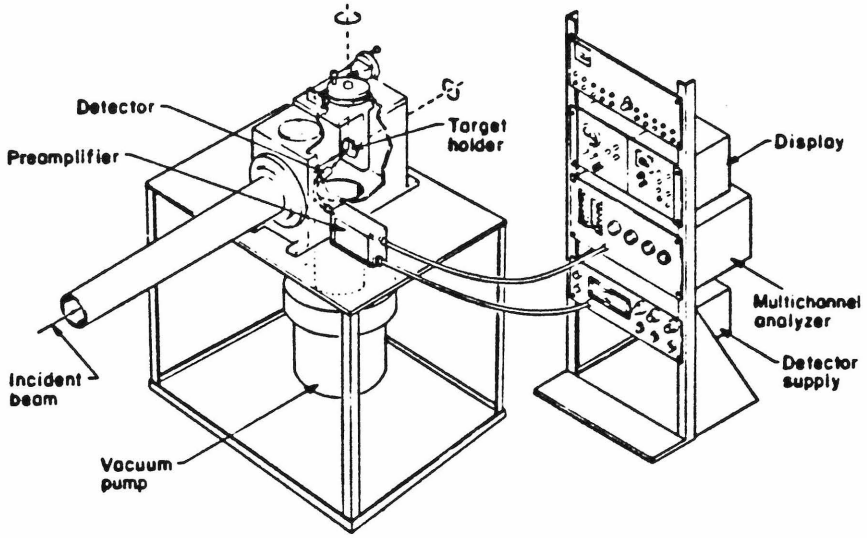
Detector
Preamplifier
Target holder
Display
Multichannel analyzer
Detector supply
Incident beam
Vacuum pump

at any depth is proportional to the number of particular atoms present. Thus for a given element the concentration profile is detected as a signal of specific height and decreasing energy. This follows from the fact that the scattering events are elastic and the particles back-scattered from the surface of the film have energies K_1E_0 while those from the back-face of the film have a lower energy K_1E_1, where K is the kinematic factor defined above. The finite energy width, therefore, reflects the energy loss that the particles undergo within the film. These can be calculated from the stopping cross sections, ϵ. For example, for a film of thickness t, the energy lost while the particle approaches the rear surface of the film is given by equation 1.

$$E_1 = \epsilon Nt \tag{1a}$$

where

$$\epsilon = \frac{1}{N}\left(\frac{dE}{dx}\right) \tag{1b}$$

and where N is the particular atomic density. These energy losses are of the order of keV. For particles scattered from the front and back face of the film the detected energy difference is given by equation 2.

$$\Delta E = Nt[\epsilon] \ , \tag{2}$$

where $[\epsilon]$, the stopping cross section factor is related to K and ϵ. For thin films there is only a small relative change in energy of the beam as it traverses the film. Thus the energy dependence of the stopping cross section can be replaced by a fixed value along the inward path and also one along the outer path. This leads to a linear relation-

ship between the energy ΔE and the depth at which scattering occurs. The accuracy of the thickness measurement is determined by the accuracy of the energy loss values used for analysis. For thin films measured in these experiments the surface energy approximation is used. Here $(\frac{dE}{dx})_{in}$ is evaluated at E_0 while $(\frac{dE}{dx})_{out}$ is taken at KE_0. Figure 3a gives an example of a spectrum obtained from Rutherford backscattering spectrometry for a thin film or iron and tungsten. Figure 3b[1] illustrates how the spectrum is interpreted. The masses of the two elements and their atomic numbers are important in that heavy masses go to high energy and light masses to low energy. The energy axis is the abscissa, while yield is the ordinate. In addition, elements with high atomic numbers give high yields and low atomic numbers give low yields. The relative concentration ratio of two elements is converted into relative yields by a ratio proportional to (Z_1/Z_2).[2] The depth in the film is translated into an energy interval. For a thin film both the front surface and the interfaces below are identifiable in the spectrum. The energy width, ΔE, together with the total number of counts each specify the number of atoms per unit area. which are contained in the film.[2,3] Backscattering spectra can therefore be though of as linear superpositions of signals obtained independently from each mass. To obtain good mass resolution the important factors are the primary energy, E_0, the projectile mass and the scattering angle.

Definitions, calculations and experimental conditions can be found in reference 1. The concepts of kinematic factor, scattering cross-

FIGURE 3a. Backscattering spectrum of tungsten-iron film. Ratio of iron to tungsten is 67:23.

FIGURE 3b. (a) Translation of concentration profiles to signals in a backscattering spectrum, demonstrated for the example of a thin homogeneous film of a binary compound with elements of a heavy M (solid line) and a light m (dashed line) atomic mass. (b) The atomic concentration profiles reappear as two separate signals. The conversion of the abscissa from depth to energy is generally not the same for the two signals, and the conversion is not exactly linear either. Usually, the nonlinearities are insignificant and the differences in the two scales is not more than 10%. (Permission to reproduce has been requested from Publishers.)

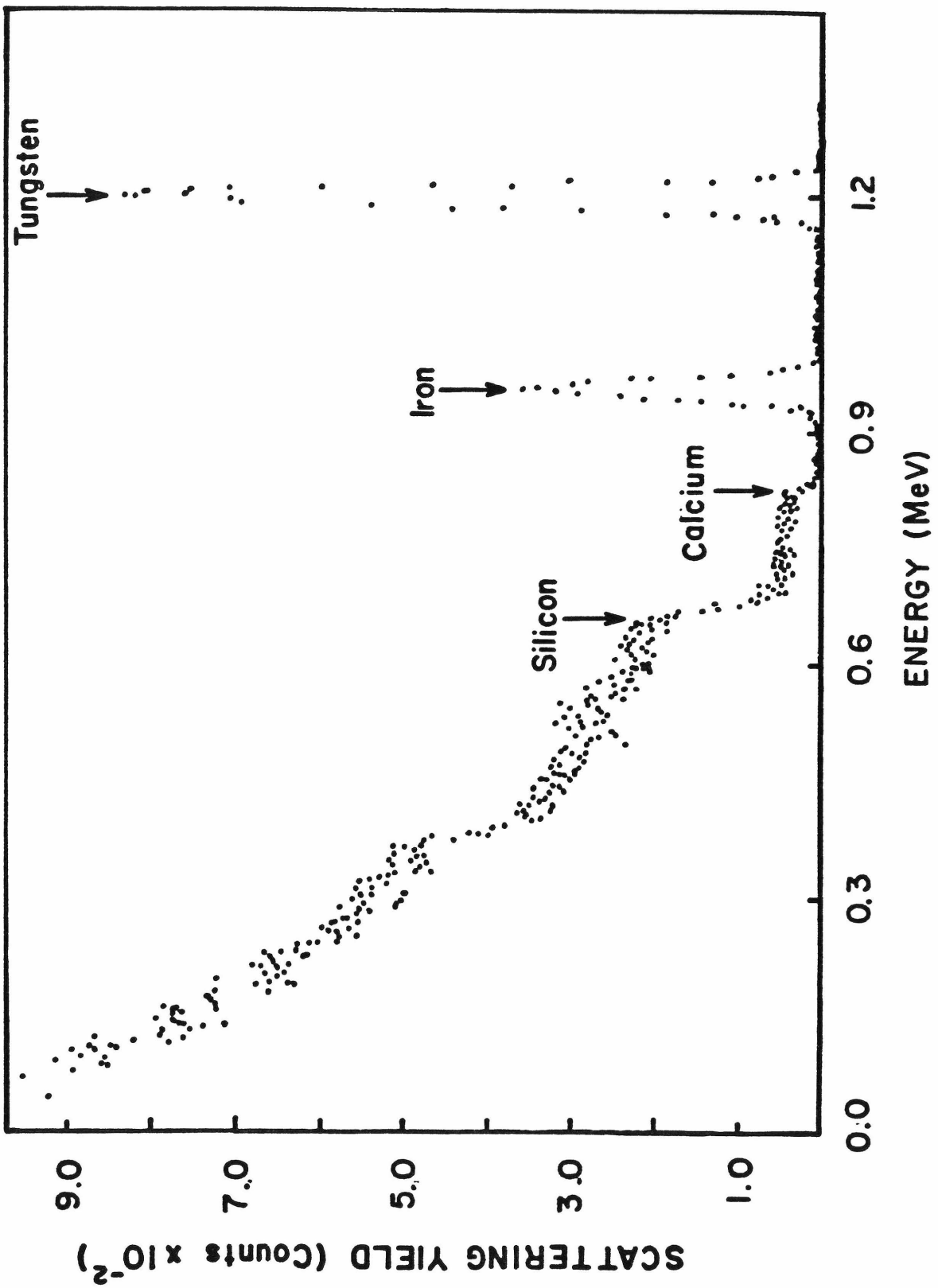
Tungsten
Iron
Calcium
Silicon
0.0
0.3
0.6
0.9
1.2
ENERGY (MeV)
1.0
3.0
5.0
7.0
9.0
SCATTERING YIELD (Counts x 10⁻²)

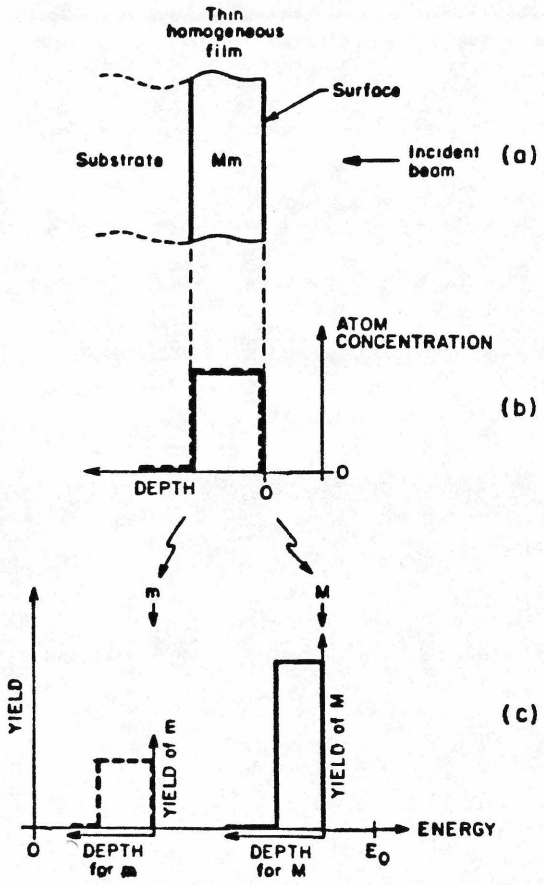
Thin
homogeneous
film
Surface
Substrate
Mm
Incident
beam
(a)
ATOM
CONCENTRATION
(b)
DEPTH
0
0
m
M
YIELD
YIELD of m
YIELD of M
(c)
0
DEPTH
for m
DEPTH
for M
E0
ENERGY

section and stopping cross section are defined and numerical values are given in appropriate tables. The following discussion outlines points specifically important in measuring the thin films described earlier.

A spectrum is interpreted in terms of H, the surface height at the high energy edge of an element. Since relationships between ΔE and mass are non-linear, approximations are used. As previously mentioned for thin films the surface energy approximation is used. This is usually accurate to within 10% and for very thin films provides even better approximation.

b. Calculation of film thickness.

To determine the film thickness on the soda-lime glass substrate the following procedure was followed using the thick target silicon signal from the glass as a reference. First, the empirical formula and molecular weight of the glass was found. This was done empirically, and theoretically, from the composition supplied by Corning for micro-slides # 2947. Agreement on the formula was within a few percent for the major elements. Bragg's rule was used to calculate ϵ_{in}^{glass}. This additivity rule says that "the energy loss in a medium composed of various atomic species is the sum of the losses in the constituent elements, weighted proportionally to the abundance in the compound".[1] For a molecule A_mB_n, therefore equation 3 holds.

$$\epsilon^{A_mB_n} = m\epsilon^A + n\epsilon^B \quad , \tag{3}$$

where ϵ^A and ϵ^B are the stopping cross sections of the atomic constituents A and B.

$(\frac{dE}{dx})_{in}$ can then be determined from equation 4.

$$(\frac{dE}{dx})_{in} = \frac{\epsilon_{in}^{glass} \rho_{glass} N_0}{MW_{glass}} = N\epsilon_{in}^{glass}, \tag{4}$$

where ρ_{glass} is the density of the glass, MW_{glass} is the molecular weight of the glass, N_0 is Avogadro's number and ϵ_{in}^{glass} is determined using Bragg's rule.

Using Bragg's rule ϵ_{out}^{glass} is also calculated, noting that equation 5 holds.

$$E_1 = KE_0, \tag{5}$$

where K is the kinematic factor for silicon as derived from tabulated values.[1] Using the surface energy approximation where $[S] = \Delta E/x$ is exact at one point, equation 6 is obtained.

$$[S_0]_{Si}^{glass} = K[\frac{dE}{dx}]_{in,Si}^{glass} + \frac{1}{\cos\theta}[\frac{dE}{dx}]_{out,Si}^{glass}, \tag{6}$$

where $\theta \sim 10°$ and $[\frac{dE}{dx}]_{in}$ is evaluated at E_0 and $[\frac{dE}{dx}]_{out}$ at KE_0. Each set of spectra are calibrated using known standards, for example, gold on silicon dioxide, germanium, etc. For calibration purposes K is plotted versus channel number. The slope of this graph yields δ, and multiplying by E gives δE in eV channel^{-1}. From this the quantity ζ can be found using equation 7.

$$\zeta = \frac{\delta E}{[\epsilon_0]^{glass}}, \tag{7}$$

where $[\epsilon_0]^{glass}$ is directly related to $[S_0]^{glass}$. For the bulk silicon equation 8 can be applied to calculated the height, H_i, of the edge.

$$H_i = \sigma(E_i)\,\Omega\,Q\,N\,\frac{\tau_i}{\cos\theta_1} \quad , \tag{8}$$

where $\sigma(E_i)$ is the scattering cross section, τ_i is the width of the slab, Q is the total number of particles incident on the sample, N is the atomic density and Ω is the solid angle spanned by the detector. For a thin iron film equation 9 is applied where A_{Fe} is total number of counts under the iron peak.

$$A_{Fe} = \sigma_{Fe}\,\Omega\,Q\,\frac{(Nt)_{Fe}}{\cos\theta_1} \quad . \tag{9}$$

Since $\cos\theta_1 \cong 1$, this can be simplified and, using the thick-target (glass) silicon signal as a reference, equation 10 results.

$$\frac{A_{Fe}}{H_{Si}} = \frac{\sigma_{Fe}\,\Omega\,Q\,(Nt)_{Fe}}{(1.2)\,\sigma_{Si}\,\Omega Q\,\dfrac{\epsilon}{[\epsilon_0]\cos\theta_1}} \quad , \tag{10}$$

where $\dfrac{\epsilon}{[\epsilon_0]\cos\theta_1}$ is substituted for $N\tau_i$ in equation 8 and the factor of 1.2 arises from the number of Si atoms in the empirical glass formula. Thus the number of iron atoms per square centimeter can be found from equation 11.

$$(Nt)_{Fe} = \frac{A_{Fe}}{H_{Si}}\,(1\cdot 2)\,\frac{\sigma_{Si}}{\sigma_{Fe}}\,\frac{\epsilon}{[\epsilon_0]} \quad . \tag{11}$$

Values of σ_{Si} and σ_{Fe} can be substituted by the ratio of their Z^2 terms since all other terms will cancel. The atomic density of iron can be found in tables and thus the thickness, t, of the film can be found from 12.

$$t = \frac{A_{Fe}}{H_{Si}^{glass}} (1.2) \left(\frac{Z_{Si}^2}{Z_{Fe}^2}\right) \frac{\zeta}{[\epsilon_0]_{Si}^{glass}} \frac{10^8}{N_{atomic\ Fe}} \text{Å} \qquad (12)$$

The area under the iron peak, A_{Fe}, is determined for each spectrum, the value of H_{Si}^{glass} is measured, and ζ is found from the slope of the calibration graph. Thus the thickness, t, of each film is easily determined from each spectrum. If more than one element is present in the film, similar calculations are performed since the elements can be treated independently.

2. X-Ray Photoelectron Spectroscopy

A schematic of an X-ray photoelectron spectrometer is shown in Figure 4.[4] A photoelectron spectrum is obtained by allowing a monoenergetic, collimated beam of photons to impinge on a sample. The photons excite electrons in the sample and the simplest spectrum is obtained when some of these electrons are emitted into the vacuum and their energy distribution is measured with an electron energy analyzer. There are three fundamental properties of each emitted photoelectron; its kinetic energy, angle of emission and the orientation of its spin. For the experiments described here only the kinetic energy at a fixed angle is examined.

In X-ray photoelectron spectroscopy the photons have high energy.

FIGURE 4. The prototype ESCA instrument with monochromatized AlKα radiation ($h\nu$ = 1486 eV; $\Delta h\nu$ = 0.2 eV). (Permission to reproduce has been requested from Publishers.)

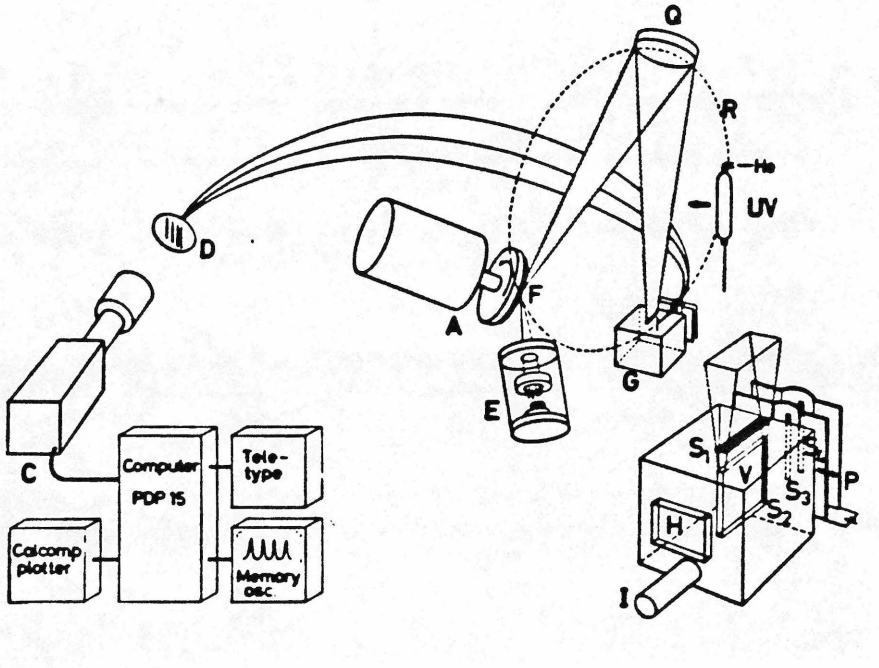
Q
R
He
UV
D
A
F
G
E
C
Computer
PDP 15
Tele-
type
Calcomp
plotter
Memory
osc.
S1
V
S3
S2
P
H
I

Usually excitation is provided by Mg K_α ($h\nu$ = 1253.6 eV) or Al K_α ($h\nu$ = 1486 eV) emission lines from X-ray tubes. The energetics of the process is defined by equation 13.

$$h\nu = I_j + E_j + \Phi, \tag{13}$$

where I_j is the ionization or binding energy of the electron for the j'th species, E_j is the kinetic energy with which such an electron is ejected by the photon, $h\nu$ and Φ is the work function. The bands in the energy distribution curves correspond to excitation of electrons from core shells.

XPS is especially useful for surface studies since the escape depth of the photoelectroscopy is in the range from 5-20 Å. It does not, however, give information on whether adsorbed species are on the surface or incorporated into the outer few layers unless the angle-resolved distributions are measured. The largest fraction of the photocurrent is associated with bulk states.

One problem that recurs in the use of XPS is the establishment of the zero of energies. In general the natural zero is the Fermi level of the sample holder which equals the Fermi level of the sample when good electrical contact exists. Since this is not always true, a secondary calibration measurement is usually made. Often this is the $Au_{f_{\frac{1}{2}}}$ line. The binding energy of this line is 84.0 ± 0.1 eV. For insulators and semiconductors this problem is compounded by positive charging of the samples as the electrons are emitted. The general method of coping with this is to flood the surface with low energy

electrons from an electron flood gun in order to discharge the sample.

Several reviews on XPS have appeared in the last few years[5-7] which contain details on instrumentation and the theory underlying photoelectron emission.

The samples studied by XPS were thin films of metals deposited on single crystal silicon and on glass surfaces. In this case, the glass was cut from microscope slide covers in order for the samples to be thin enough to fit in the sample holders of the modified Hewlett Packard 5950A XPS spectrometer[8,9] at JPL.

Spectra were recorded over both wide energy ranges and, with higher resolution (~ 0.2 V), over a narrower range. Two such spectra are shown in Figure 5. The main purpose of these spectra is to identify the chemical species present. Figure 5a is a spectrum of tungsten deposited on silicon. This illustrates the chemical species present in the sample while Figures 5b and 5c show the high resolution spectra taken for the carbon and tungsten region. The carbon region could be deconvoluted to exhibit three peaks, one large and two smaller peaks. No exact assignment was made for these peaks, but it was determined by comparison with published spectra that no tungsten carbide or tungsten carbonyl was present. The carbide species would have appeared at lower binding energy compared to the large peak ($\sim$282.5 eV)[10] while the carbonyl species would be found at much higher energies (291.2 eV).[11] The peak at $\sim$ 288 eV could possibly be due to a sub-carbonyl species or a carboxylic carbon. It is doubtful that it is a metal carbonyl species since the peak was also present in samples with

FIGURE 5. (a) XPS spectrum of thin tungsten film (~ 200 Å);
b) High resolution XPS spectrum of carbon region of tungsten film;
c) High resolution XPS spectrum of tunsten region of tungsten film.

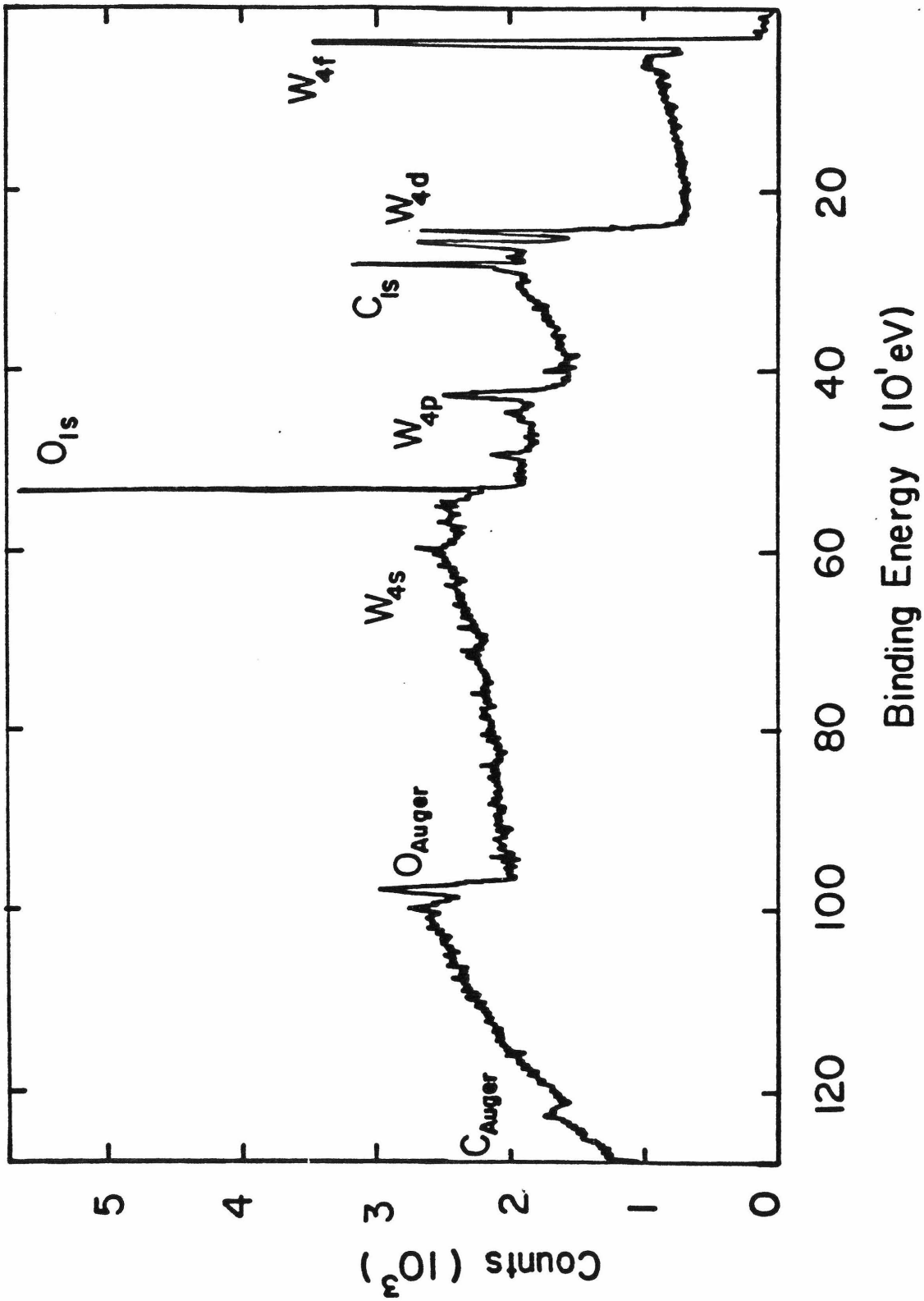
Counts (10^3)
0
1
2
3
4
5
120
100
80
60
40
20
Binding Energy (10'eV)
O_{1s}
W_{4s}
O_{Auger}
C_{Auger}
W_{4p}
C_{1s}
W_{4d}
W_{4f}

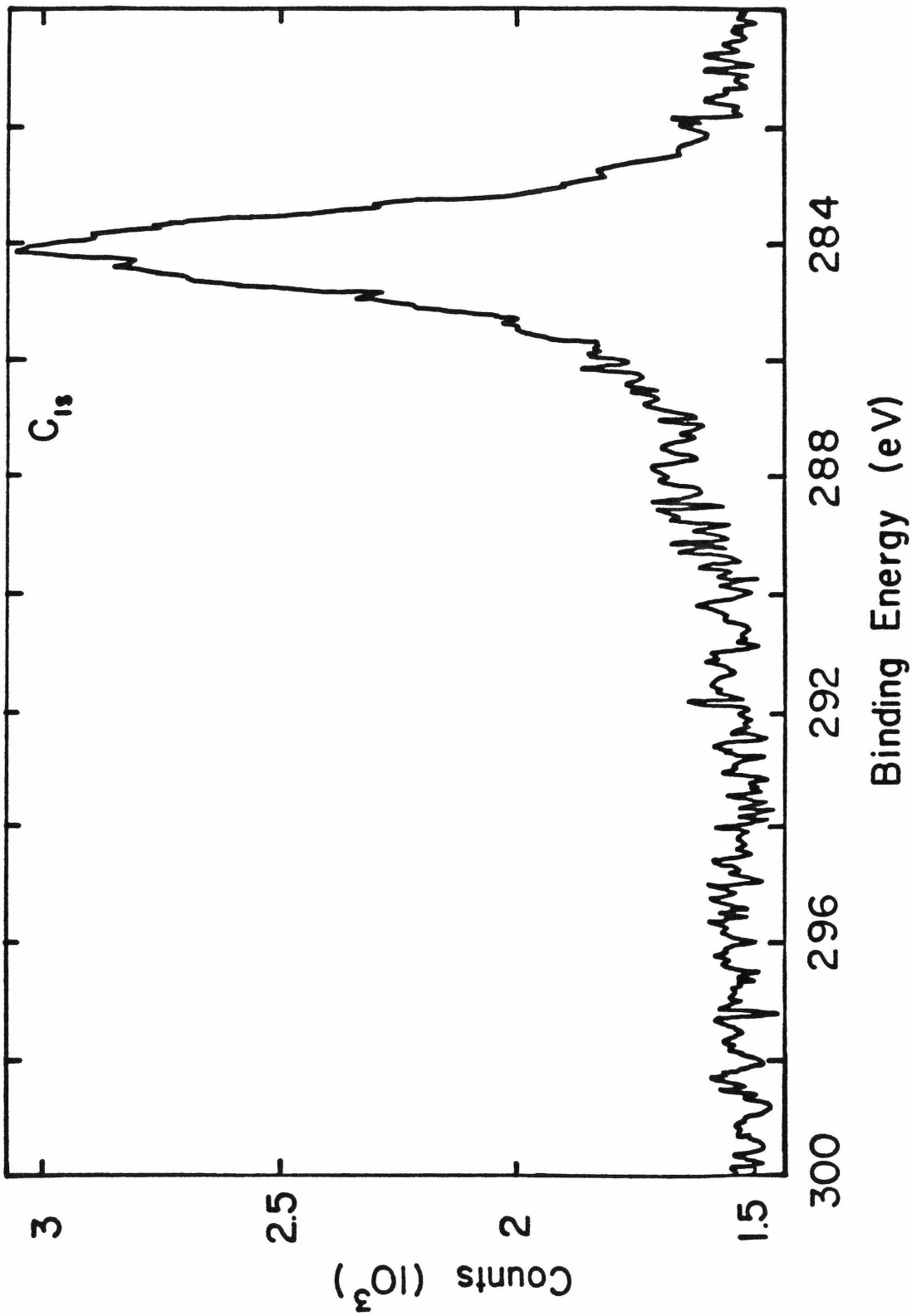
C1s
Counts (10³)
3
2.5
2
1.5
300
296
292
288
284
Binding Energy (eV)

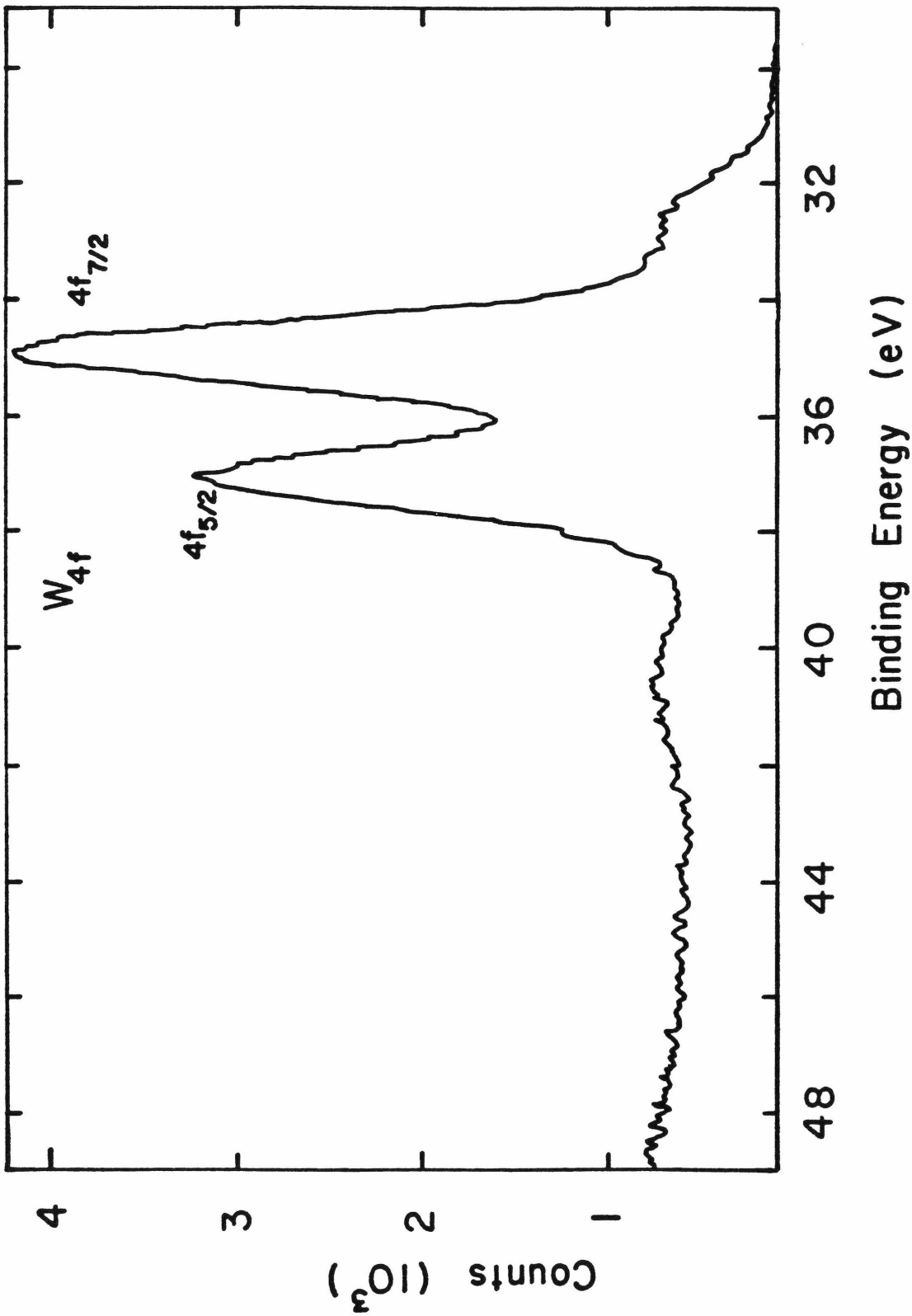
W_{4f}
$4f_{7/2}$
$4f_{5/2}$
Counts (10^3)
4
3
2
1
48
44
40
36
32
Binding Energy (eV)

no metal film. The major source of impurity appears to be the hydrocarbons from the vacuum system. This is determined from a number of control experiments and by argon sputtering. The drawbacks associated with argon sputtering have been discussed in detail.[12] The major problem for determining whether the carbon was a true film impurity or from the vacuum system was that the carbon, being a lighter element could be preferentially sputtered. However, the experimental results show that when 0.5 eV argon ions were used this was not a problem and, indeed, the carbon content in the film decreased by 60% before increasing again at the film-substrate interface.

Figure 5c, when compared to published data[12] corresponds to two oxidation species of tungsten, W(IV) and W(VI). By examining the oxygen peaks it was determined that these were WO_2 and WO_3 with small quantities of hydroxide present. All the assignments were relative to carbon 1s at 284.4 eV. This was particularly necessary in these experiments since charging of the samples was a problem. The silicon substrate, however, was far less of a problem.

The above data were helpful in determining the mechanism of photoassisted deposition, but it would be necessary to carry out in situ ultra-high vacuum XPS to accurately characterize the metal film.

3. X-Ray Microprobe Analysis

X-ray microprobe analysis is often employed in conjunction with a scanning electron microscope. The reason for this is that both techniques depend upon a beam of high energy electrons to obtain information from a substrate. Scanning electron microscopes monitor surface

topology and X-ray microprobe analysis determines the elemental composition of the irradiated area. The latter is achieved by providing a spectrum of emitted X-rays characteristic of the irradiated element.

A number of interactions occur when a beam of electrons strike a solid substrate. These are shown schematically in Figure 6.[13] Each of the illustrated events provide information on the specimen. X-ray microprobe analysis utilizes the X-rays generated within $\lesssim 10\,\mu m$ of the specimen by the high energy electron beam. The X-rays are characteristic of the atoms within the specimen in the irradiated region. Consequently, X-rays can be used to identify and quantify the elements present. Detectors collect the X-rays and the spectrum is displayed on a multichannel analyzer as X-ray yield versus energy. A schematic of this is shown in Figure 7.[13]

The type of detector used depends on the particular applications involved. In this case an energy dispersive analyzer (solid state detector) was used. An advantage of this detector is that it can be placed very close to the source of X-rays and thus can accept a wide angle of radiation. Consequently this increases the sensitivity of the detector. The energy resolution of a detector is defined as its ability to distinguish two adjacent peaks in the energy spectrum. Solid state detectors have a resolution of $\lesssim$ 150 eV at 5.9 keV. To obtain the maximum resolution the detector is maintained at liquid nitrogen temperature. This also effectively decreases the noise level.

Bombardment of the sample by the primary beam produces three major types of electron signal; the reflected electrons, low energy

FIGURE 6. The various effects of electron-specimen interaction. Light is emitted as visible fluorescence; elastically scattered electrons suffer no energy loss; inelastically scattered electrons lose some energy, and secondary electrons are of much lower energy than the primary electron beam. (Permission to reproduce has been requested from Publishers.)

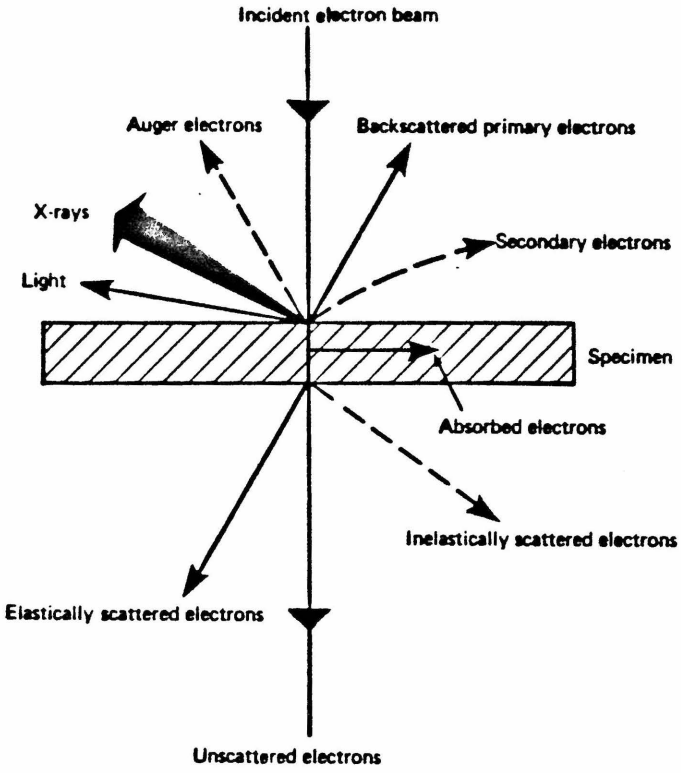
Incident electron beam
Auger electrons
Backscattered primary electrons
X-rays
Secondary electrons
Light
Specimen
Absorbed electrons
Inelastically scattered electrons
Elastically scattered electrons
Unscattered electrons

FIGURE 7. Typical arrangement for a scanning electron miscropscope (SEM) with a solid state detector attached. Microscopes can also be fitted with crystal spectrometers. (Permission to reproduce has been requested from Publishers.)

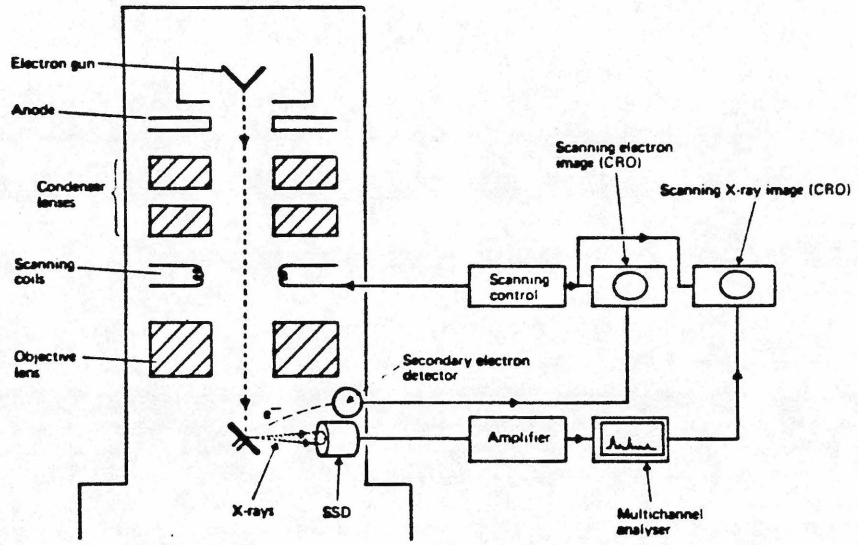
Electron gun
Anode
Condenser lenses
Scanning coils
Objective lens
Scanning electron image (CRO)
Scanning X-ray image (CRO)
Scanning control
Secondary electron detector
Amplifier
X-rays
SSD
Multichannel analyser

secondary electrons and the specimen current. The reflected electrons are scattered from the surface while the secondary electrons arise from just below the surface. Specimen current is the total net electron beam absorbed by the specimen. To obtain quantitative data the specimen current must remain constant for the counting period. The back-scattered electrons provide information on atomic number distribution within the specimen since the larger the atomic number the greater the degree of scattering and the brighter the image will appear on the oscilloscope.

Characteristic X-rays come from a pear-shaped volume below the surface of the specimen. The depth of this volume depends on the energy of the incident beam and on the specimen composition. For thin samples of metals the lateral diffusion of the electron beam is minimal at 15 keV and spatial resolution is about 1 μ. In addition, X-ray fluorescence and absorption are negligible.

For most experiments the energy range of the incident beam was 15 keV. As long as the metal film was ~ 200 Å charging of the substrate was not too much of a problem although in thinner samples this did create some difficulties. The MCA is programmed so that energy ranges can be adjusted and energy windows created. The spectrum is displayed on a CRO and photographs are taken as permanent records. Spectral lines are also identified by electronic marks on the screen.

Figure 8 shows a typical X-ray microprobe spectrum. Peak intensities are measured by integrating the area under the peak. Background intensities can be subtracted. Quantitative X-ray analysis is

FIGURE 8. X-ray microprobe spectrum of iron film (200 counts). Film is composed of iron and chromium and is ~ 200 Å thick.

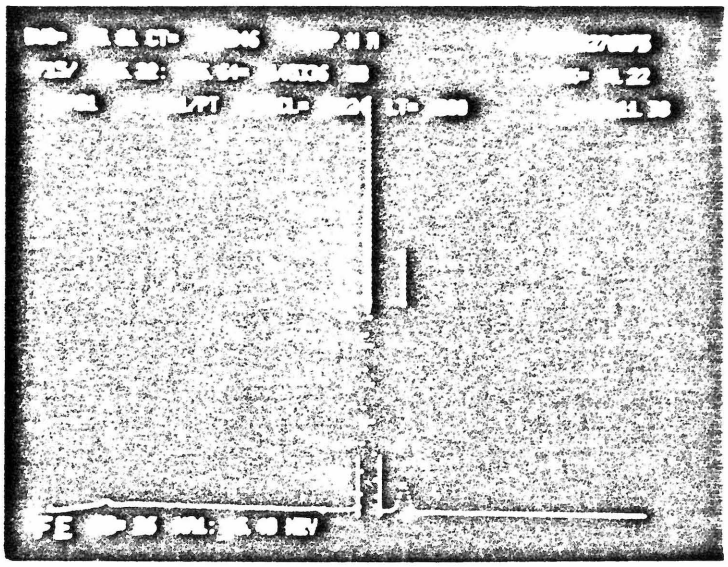

effected by using a standard. This is particularly necessary for comparing two elemental quantities. For instance, relative concentrations of iron and chromium were determined by the ratio method[13] using bulk standards. For this method the measured ratio, $\frac{I_{Fe}}{I_{Cr}}$, of X-ray intensities of iron and chromium is related to the mass concentration ratio ($\frac{M_{Fe}}{M_{Cr}}$) by equation 14

$$\frac{M_{Fe}}{M_{Cr}} = \frac{I_{Fe}}{I_{Cr}} \cdot \frac{Q_{Cr}}{Q_{Fe}} \cdot \frac{I'_{(Cr)}}{I'_{(Fe)}} \quad , \tag{14}$$

where Q_i is the ionization cross-section for electrons with incident beam energy, E_0 and I_i is the corrected X-ray intensity from pure bulk standards. In this case E_0 is 15 keV and the corrected ($\frac{Q_{Cr}}{Q_{Fe}}$) ratio was found to be 1.035. Thus the relative composition of thin film samples can easily be found from equation 14 by measuring peak intensities for bulk and thin film samples. It must be emphasized, however, that these measurements must all be carried out at constant specimen current. This is monitored on a Keithley electrometer and for these experiments was $\sim 10^{-9}$ amps.

REFERENCES

1. W-K. Chu, J. W. Mayer and M-A. Nicolet, "Backscattering Spectrometry", Academic Press, N.Y. (1978).
2. M-A. Nicolet, J. W. Mayer, I. V. Mitchell, Science, 177, 841 (1972).
3. W. K. Chu, J. W. Mayer, M-A. Nicolet, T. M. Buck, G. Amsel and F. Eicen, Semiconductor Silicon, 416 (1973).
4. K. Siegbahn, "Molecular Spectroscopy", Ch. 15, 227. Hayden and Son, Ltd., London (1977).
5. M. Cardona and L. Ley, in Topics in Applied Physics, Vol. 26, eds. M. Cardona and L. Ley, Springer-Verlag, N.Y. (1978).
6. C. S. Fadley, in "Electron Spectroscopy: Theory, Techniques and Applications, Vol. II, C. R. Brundle and A. D. Baker, eds. (1978).
7. "Handbook of X-Ray and Ultraviolet Photoelectron Spectroscopy", ed. D. Briggs, Hayden and Sons, Ltd. London (1977).
8. F. J. Grunthaner, NBS Spec. Publ. 400-23, ARPA-Workshop IV, Surface Analysis for Silicon devices, NBS, Gathersburg, Md.
9. B. F. Lewis, Rev. Sci. Inst., submitted.
10. Perkin-Elmer "Handbook of X-Ray Photoelectric Spectrscopy".
11. E. W. Plummer, W. R. Salanede and J. S. Miller, Phys. Rev. B. 18(4), 1673 (1978).
12. L. J. Colton and J. W. Rabalais, Inorg. Chem., 15(1), 236 (1976) and references therein.
13. J. A. Chandler, "X-Ray Microanalysis in the Electron Microscope", North-Holland Publishing Co., Amsterdam (1978).

CHAPTER III

Photoassisted Chemistry of Organometallic Compounds at Gas-Solid Interfaces: Formation of Thin Metal Films

Photoassisted Chemistry of Organometallic Compounds at Gas-Solid Interfaces: Formation of Thin Metal Films

Patricia M. George and J. L. Beauchamp

Contribution No. from the Arthur Amos Noyes Laboratory of Chemical Physics, California Institute of Technology, Pasadena, California 91125

(Received 1980)

Abstract: Thin metal films are formed on a variety of substrates by photoassisted and electron-assisted decomposition of organometallic compounds at low pressures. The organometallics studied include $Fe(CO)_5$, $Cr(CO)_6$, $Mo(CO)_6$, $W(CO)_6$, $(\eta^5\text{-}C_5H_4CH_3)Mn(CO)_3$, $(\eta^5\text{-}C_5H_5)Fe_2$ and $(\eta^5\text{-}C_5H_5)_2Ni$. Film deposition is examined primarily on soda-lime glass and to a lesser extent on SiO_2 and silver surfaces. A photoassisted mechanism is proposed which involves three states: initiation, propagation, and termination of film growth. Initiation is thought to occur primarily by the formation and subsequent reaction of photoelectrons and by photodecomposition. At low pressures formation and reaction of photoelectrons probably dominates while at higher pressures photodecomposition becomes increasingly important. The organometallic compounds react with electrons by dissociative electron capture, forming negative ions that decompose further to produce thin metal films. Propagation involves a catalytically active surface capable of effecting a number of turnovers in the dark before termination occurs. The limiting step appears to be loss of remaining CO ligands from the metal species on the surface.

Introduction

Deposition of thin metal films by irradiating organometallic compounds with UV light[1-4] or high energy electron beams has received sporadic attention in the past few years. The importance of forming dispersed transition metals for catalysis and the need for depositing metal films and structures with well-defined edge resolution at low temperature has led to renewed interest in these processes. Experimental methods employed in the past studies[1-4] were similar in that a substrate, under ~ 10 Torr of reactive gas, was placed in a static cell and irradiated with UV light from conventional arc lamps and laser sources. Irradiation through a mask or with a focused laser beam has yielded metal deposits with micrometer-size features.[3,4] In this paper we report a detailed mechanistic study of thin film deposition using low pressures ($\leq 10^{-2}$ Torr) of organometallic compounds irradiated by UV light under flow conditions.

At least three distinct stages can be identified in the photo-assisted decomposition of organometallic compounds at gas-surface interfaces. For purposes of discussion these are referred to as the initiation, propagation and termination stages of film growth. Initiation provides the primary reactive intermediates to the substrate throughout the irradiation period. Propagation is defined as the process occurring when metal is deposited and the film is growing. This stage may continue in the absence of light. Termination is considered as the cessation of film growth either by terminating irradiation, deactivation of the primary intermediates or, in the event of propagation in the dark, by poisoning of surface sites.

Initiation, which can occur in several ways, is illustrated in Figure 1. Elevated surface temperatures may lead to the occurrence of thermal decomposition processes (Figure 1a) if the photon energy flux is high enough. The calculated[5] increase in surface temperature varies from $\sim 8°$ C to $\sim 800°$ C as the photon energy flux increases from 4 W cm^{-2} to 4 W cm^{-2}. A focused laser system operating at 4 MW cm^{-2} can effect a temperature rise of over 5500° C.[5] At relatively high reactant gas pressures photodecomposition in the gas phase (Figure 1b) is important. In addition, highly specific photochemical processes may occur at the gas surface interface. Molecules in close contact with the surface have modified absorption spectra due to differential interactions of the ground and excited states with the surface sites. Changes which may occur include broadening and shifting of spectral features, modification of the extinction coefficients of absorption bands and the appearance of new absorption bands.[6,7] Photoexcited electron transfer from the surface to a molecular species may occur with high probability with the energetics of such processes being dependent on the donor-acceptor properties (work function and electron affinity) of the surface and the donor-acceptor properties (ionization energy and electron affinity) of the molecule. Photon absorption may lead to modification of surface charges or the production of free electrons which induce decomposition of gas phase species and eventually lead to the formation of metal deposits.

Eventually the substrate will develop a uniform thin film which has properties significantly different from the original surface. This condition persists during the propagation phase of film growth, which

FIGURE 1. Schematic representation of processes which may occur during initiation stage of deposition.

Initiation

a. thermal

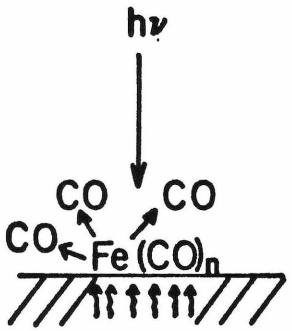

b. photodecomposition in the gas phase

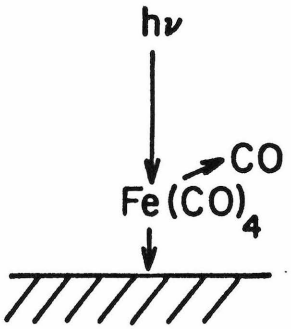

c. photodecomposition of adsorbed molecules

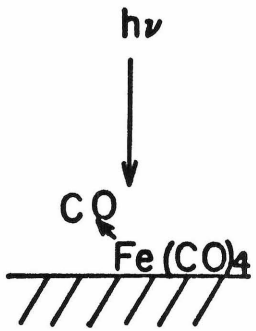

d. electron transfer

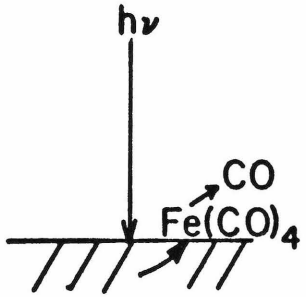

e. electron capture

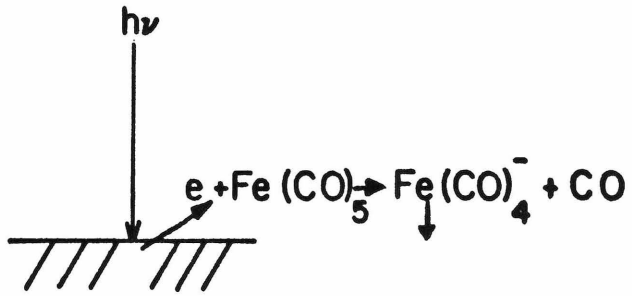

may be characterized by physical and chemical processes distinctly different from those which initiate film growth. For example, coordinately unsaturated metal sites may act catalytically to decompose additional organometallic molecules. Many turnovers may result, even in the dark, before surface sites are rendered inactive.

Metal carbonyls, such as iron pentacarbonyl and the Group VIB hexacarbonyls, were chosen for this investigation. A range of substrate materials were used, including various glasses, silver foil and single crystal silicon. Reactions were carried out in a vacuum system with a base pressure of $\sim 10^{-8}$ Torr. Monitoring of depositions was accomplished by work function and resistivity measurements, the former being highly sensitive to low densities of metallic species on insulating surfaces. Techniques used to examine film thicknesses and compositions include Rutherford backscattering spectrometry, X-ray photoelectron spectroscopy and energy dispersive X-ray microprobe analysis on a scanning electron microscope.

II. Experimental

1. Apparatus. Three somewhat different experimental arrangements were employed for these studies; one for photoelectric measurements, a second for photoassisted metal film deposition and another for metal deposition using low energy electrons generated by an electron gun. All were mounted in a stainless steel vacuum chamber evacuated to 10^{-8} Torr by a liquid nitrogen-trapped diffusion pump.

a. Extinction coefficients of metal carbonyls. Gas phase UV absorption data were recorded for the metal carbonyls and extinction coefficients calculated at 5.1 eV. For $Fe(CO)_5$ the absorption spectrum and extinction coefficients were measured from 220 nm to 350 nm. This was accomplished in two different ways. One method employed the vacuum system described in Figure 2. Two quartz windows allowed the UV beam to be transmitted and known pressures of $Fe(CO)_5$ were flowed through the beam at each wavelength. This corrected for any absorbance due to other species, e.g., $Fe_2(CO)_9$. The transmittance of the window was determined before and after each absorbance measurement to correct for deposition on the window. Changes in radiant power were monitored on a Model RK 3440 Laser Precision radiometer. Typical initial radiant powers were ~ 0.2 mW/cm^2. The other method involved filling a 20.75 cm gas cell fitted with quartz windows with pressures of $Fe(CO)_5$ ranging from 2×10^{-3} Torr to 9×10^{-2} Torr and recording the absorption spectrum from 220 nm to 350 nm on a Cary 17 spectrometer. Absorption spectra of the empty gas cell were recorded before and after the spectra were measured.

b. Photoelectric measurements. A high pressure 2.5 kW Xenon-mercury lamp dispersed with a Bausch and Lomb 0.25 m monochromator set for a 12 nm band pass was used to provide ultraviolet light. Quartz lenses focused this beam to an area of 0.25 cm^2 on the substrate through a suprasil window. Infrared radiation was removed

FIGURE 2. (a) Experimental apparatus for deposition of thin metal films using photoelectron, (b) low energy electron gun.

Experimental apparatus

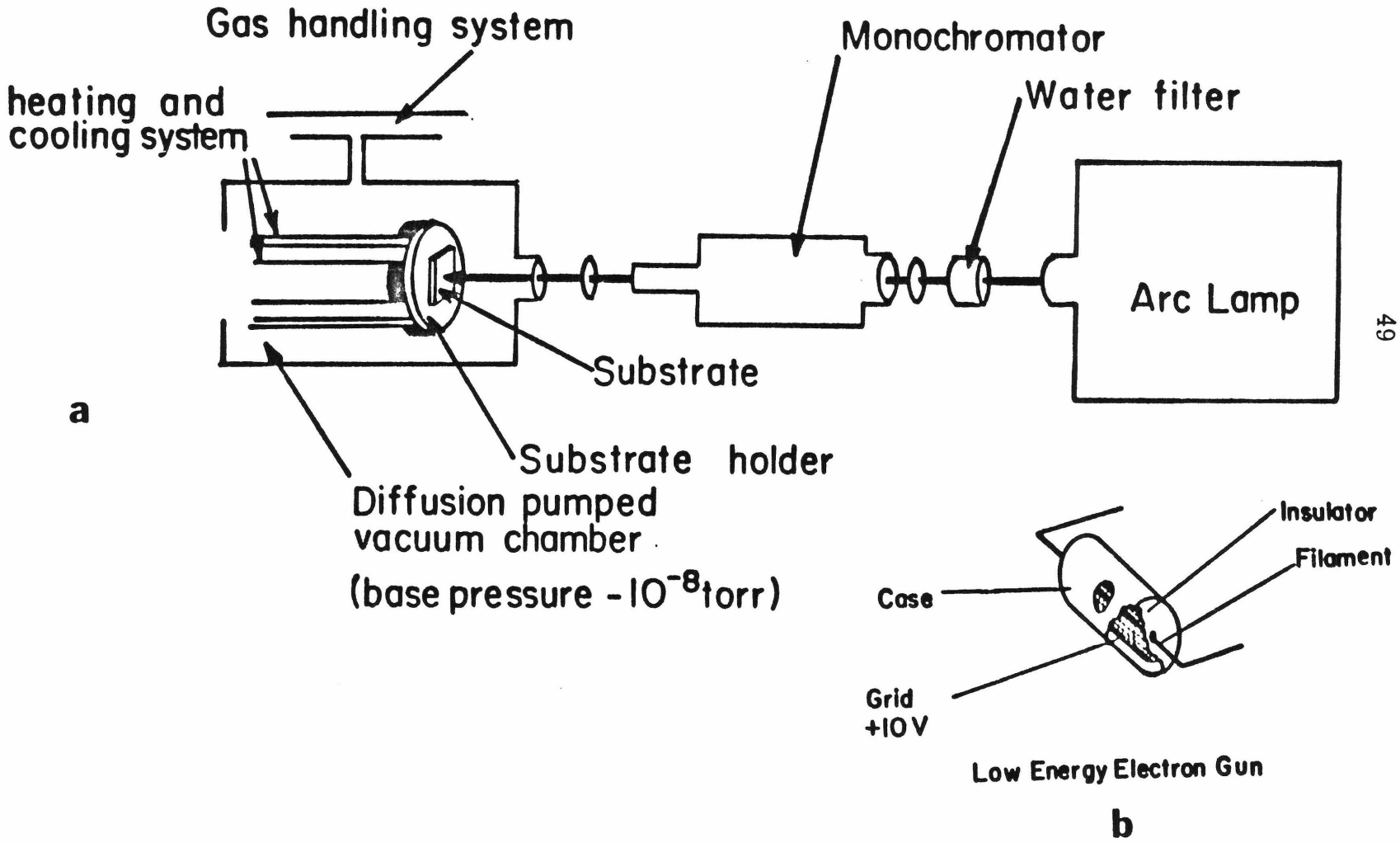

using a water filter. A standard photodiode arrangement was employed to measure photocurrents with the collector biased above the space-charge limit at 375 volts. Both electrodes of the photodiode were shielded with pyrex glass to avoid spurious signals and photocurrents were measured on a model 610A Keithley electrometer.

c. Substrates. Substrates included soda lime glass (1.2 cm^2 × 0.01 cm), silver foil (1.2 cm^2 × 0.003 cm) and single crystal silicon (1.2 cm^2 × 0.005 cm). Surface oxides were removed from the silver by abrasive cleaning and all substrates were cleaned with hexane and ethanol before heating in vacuum at 10^{-7} Torr.

2. Metal Film Deposition With UV Light. The experimental arrangement employed to achieve metal film deposition using UV light is illustrated in Figure 2. The UV light source and optics are identical to those used in photoelectric measurements. Substrates were mounted on a copper block which could be heated or cooled to liquid nitrogen temperatures. A calibrated W-5% Re versus W-26% Re thermocouple[8] was used to monitor temperature. Pressure measurements utilized a Bayard-Alpert ionization gauge (Veeco RG75K) below 10^{-4} Torr. At higher pressures a capacitance manometer (MKS Instruments, model 221) was employed. All organometallic compounds were from Alfa Products or Strem Chemicals. Most experiments were carried out using $Fe(CO)_5$ with limited data being obtained for $Mo(CO)_6$,$Cr(CO)_6$, $W(CO)_6$, $(\eta^5\text{-}C_5H_4CH_3)Mn(CO)_3$, $(\eta^5\text{-}C_5H_5)_2Fe$, and $(\eta^5\text{-}C_2H_5)_2Ni$. Prior to use these were freed from non-condensable

impurities by repeated freeze-pump-thaw cycles at liquid nitrogen temperatures. Deposition of metal films on the inside of the window became a problem when film thicknesses on the substrate exceeded ~ 200 Å. This could be avoided by using a flow of argon to keep reactive species away from the window or by using a molecular beam arrangement to direct reactive species at the substrate.

3. Metal Film Deposition With Low Energy Electrons From an Electron Gun. Additional deposition experiments were carried out using only low energy electrons. Substrates were irradiated by a diffuse beam of low energy electrons emitted from an electron gun (Figure 2b). The electron gun, mounted on a 2.75-in flange, is comprised of a Re filament, electrically isolated from a metal grid which was biased at +10 V. The filament can be negatively or positively biased in order to increase the electron yield or reduce the emission to zero. Currents of up to 10^{-8} A ($\sim 10^{11}$ electrons s^{-1}) impinged on the substrate which was located 2.5 cm away from the electron gun. Cooling the substrate corrected for any thermal radiation effects from the filament. In addition, control experiments were performed by positively biasing the filament so that no electrons were emitted.

4. Film Analysis. In situ film monitoring was limited to photoelectric work function and two-probe resistivity measurements. The metal films were analyzed by energy dispersive X-ray microprobe analysis on an ISI model SMS2-2 scanning electron microscope equipped with a United Scientific X-ray analyzer. Chemical composition of the film was determined using a modified Hewlett-Packard 5950A

XPS spectrometer.[9] The backscattering spectrometer[10] facility in Kellogg Radiation Laboratory at Caltech was used to measure film thickness and metal composition.

III. Results

1. Photoelectric Yield of Substrates. Figure 3 illustrates the photoelectric yield per radiant energy flux as a function of photon energy for two substrates soda lime glass and silver. A sharp threshold at 4.2 eV is observed for silver. The photocurrent from glass increases slowly over the photon energy range, the threshold being less well defined. At 5.12 eV the quantum yield for soda lime glass is 6×10^{-7} electrons photon^{-1}. Irradiation at this energy with a photon flux of $\sim 5 \times 10^{15}$ photons cm^{-2} s^{-1} gives an electron flux of 3×10^{9} electrons cm^{-2} s^{-1}.

2. Photoelectric Yields of Films. UV irradiation of the glass substrate in the presence of $\leq 10^{-2}$ Torr metal carbonyl yields a thin conducting metal film. Since a majority of the experiments involve iron, deposited from $Fe(CO)_5$ on soda lime glass, detailed results are given for this system. Except as specifically noted, similar results are obtained from the molybdenum, chromium and tungsten carbonyls.

Photoelectric yields were periodically measured during the course of iron deposition (Figure 4). Continuous monitoring was not performed to avoid possible effects of the electric field on the deposition process. Curve 1 in Figure 3 represents the clean soda-lime glass substrate, while curves 2, 3 and 4 illustrate the photo-yields after 5, 30 and 75 minutes of deposition, respectively. After

FIGURE 3. (a) Plot of photocurrent versus photon energy for soda-lime glass and silver, (b) Gas phase absorption spectrum of $Fe(CO)_5$ at 5×10^{-3} Torr.

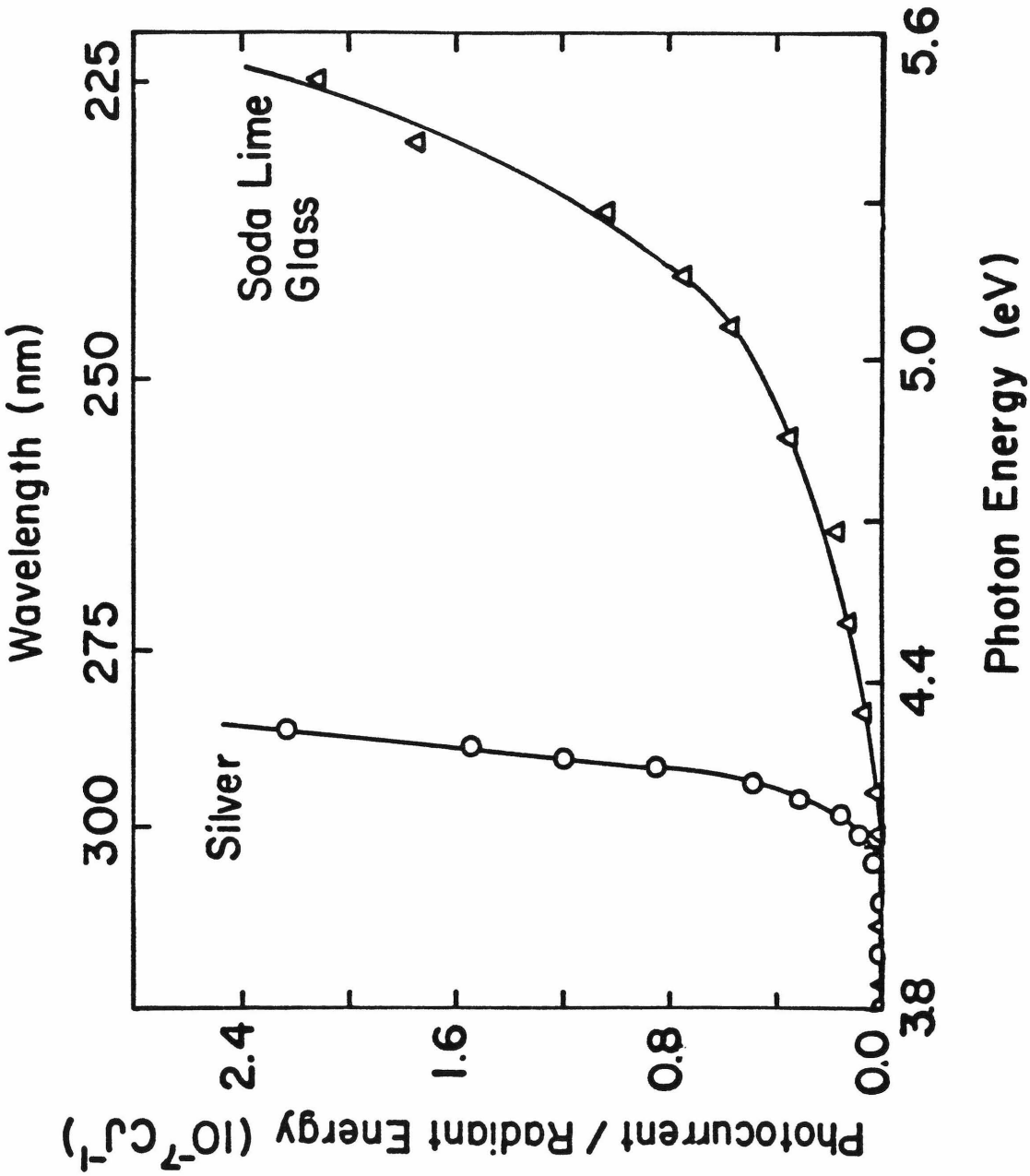
Wavelength (nm)
225
250
275
300
Photon Energy (eV)
5.6
5.0
4.4
3.8
Photocurrent / Radiant Energy (10^{-7} CJ^{-1})
2.4
1.6
0.8
0.0
Soda Lime Glass
Silver

a.

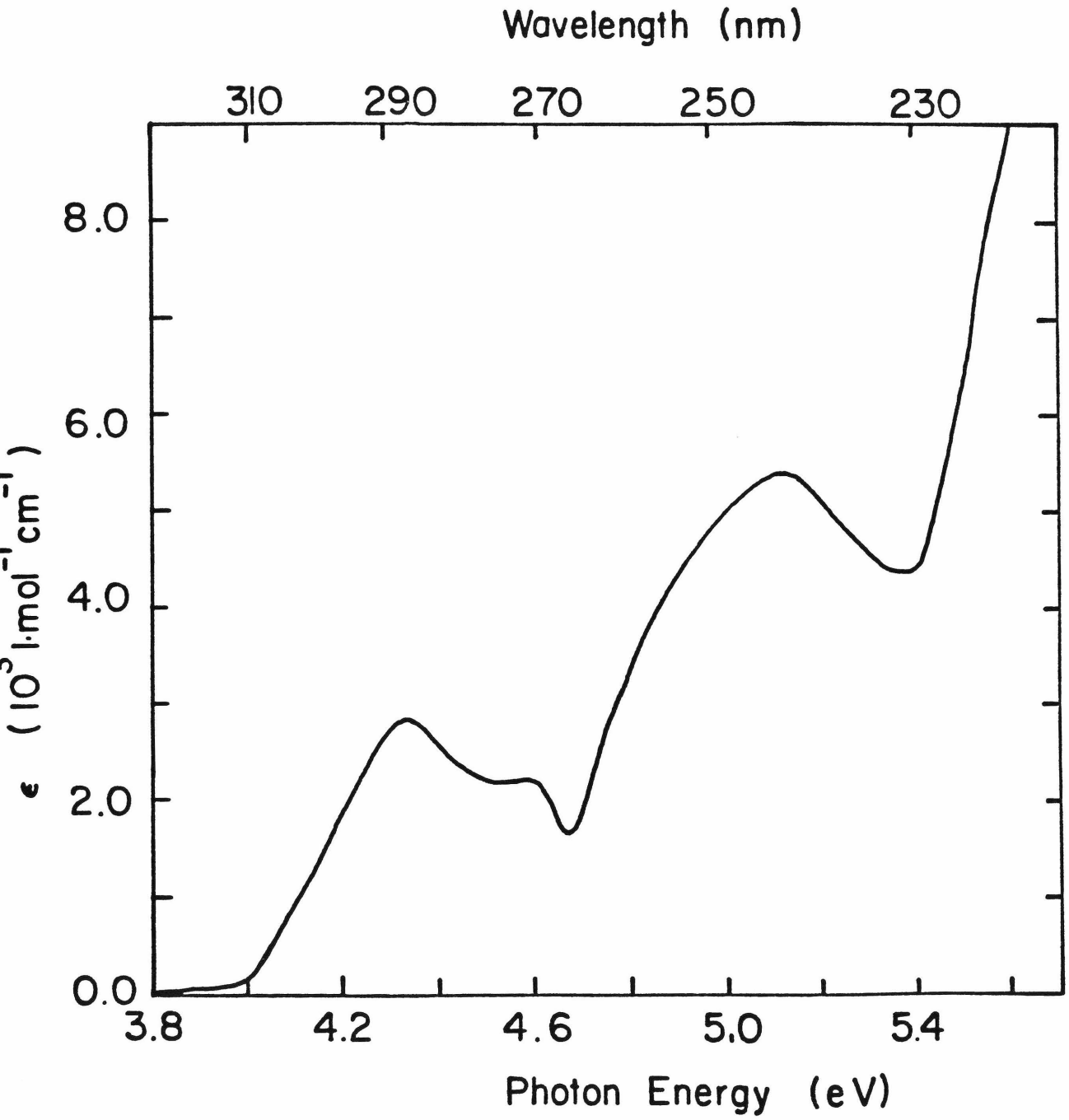
Wavelength (nm)
310
290
270
250
230
8.0
6.0
4.0
2.0
0.0
ε (10³ l·mol⁻¹cm⁻¹)
3.8
4.2
4.6
5.0
5.4
Photon Energy (eV)

b.

FIGURE 4. Plot of photocurrents versus photon energy for an iron film growing on a soda-lime glass substrate. The film was grown by irradiating the substrate at 5.1 eV in the presence of 10^{-2} Torr $Fe(CO)_5$. No bias was applied during deposition.

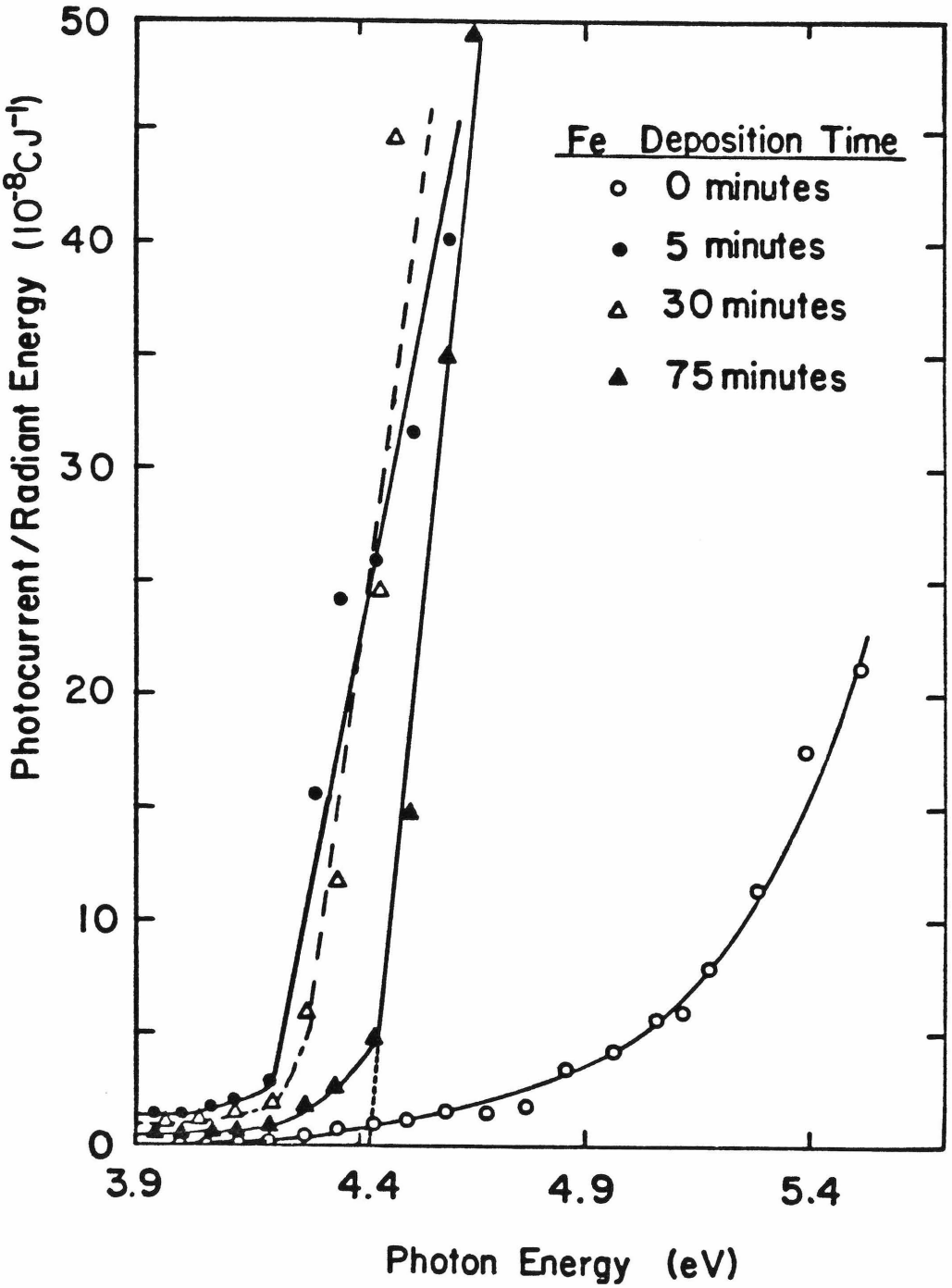
Photocurrent / Radiant Energy (10^{-8}CJ^{-1})
50
40
30
20
10
0
3.9
4.4
4.9
5.4
Photon Energy (eV)
Fe Deposition Time
0 minutes
5 minutes
30 minutes
75 minutes

only a few minutes the growing film enhances photoelectric yield to 3×10^{11} electrons cm^{-2} s^{-1} at 5.1 eV. These additional electrons may be attributed to photoemission from the iron since the irradiating photon energy is also above the photoemission threshold for iron. The photoelectric yield curve becomes progressively metallic in nature.

Work functions of the growing films are determined by making use of the graphical techniques[11] based on Fowler's theory.[12] In this analysis the quantity $Y^{\frac{1}{2}}$ is plotted versus $h\nu$, where Y is the quantum yield of electrons and $h\nu$ is the photon energy. For thicker films (≤ 100 Å) these result in a straight line which intercept the $h\nu$ axis to give the work function. Straight lines were not obtained for soda lime glass and films ≤ 100 Å, presumably due to surface inhomogeneities.[13] This is interpreted as the growth of iron clusters which eventually coalesce to form thin conducting iron films. The work function increases until it attains a maximum value of 4.4 eV (Figure 5). Since work functions increase considerably on annealing[14] this value compares well with the 4.7 eV obtained for films annealed at 373 K.[15]

3. Film Composition. Initially the films are highly reflecting and metallic, but upon exposure to air they are readily oxidized. These observations are supported by XPS data and resistivity measurements. Table I lists the XPS data for iron films, tungsten films and iron/tungsten films on a silicon substrate. Predominant iron species in films containing iron are Fe(III) and Fe(II) in the form of oxides, probably Fe_2O_3 and Fe_3O_4.[16] The presence of a second oxygen peak at higher binding energies, however, indicates that hydroxyls are also

Table 1. XPS Binding Energy (eV)

	O_{1s}		Fe_{2p}		W_{4f}		
	1	2	1	2	1	2	3
Iron	530.0(2.7)[a]		724.5	710.8			
Sputtered iron	529.9(1.5)	531.3(1.5)	724.0	710.8			
Tungsten	530.5(1.9)	532.0(5)			37.0	35.0	33.0
Sputtered tungsten	530.7(1.6)	532.0(5.5)			37.2	35.1	33.1
Iron/Tungsten	529.9(1.5)	531.2(1.5)	724.6	711.0	36.8	34.7	33.1(5)
Sputtered iron/tungsten	529.9(1.4)	531.3(1.4)	724.3	710.9	36.8	34.6	-

a) Values in parentheses refer to FWHM.

FIGURE 5. Plot of photoemission threshold as a function of time during growth of iron film. Deposition conditions are the same as in Figure 3. Threshold values were determined from Fowler plots.

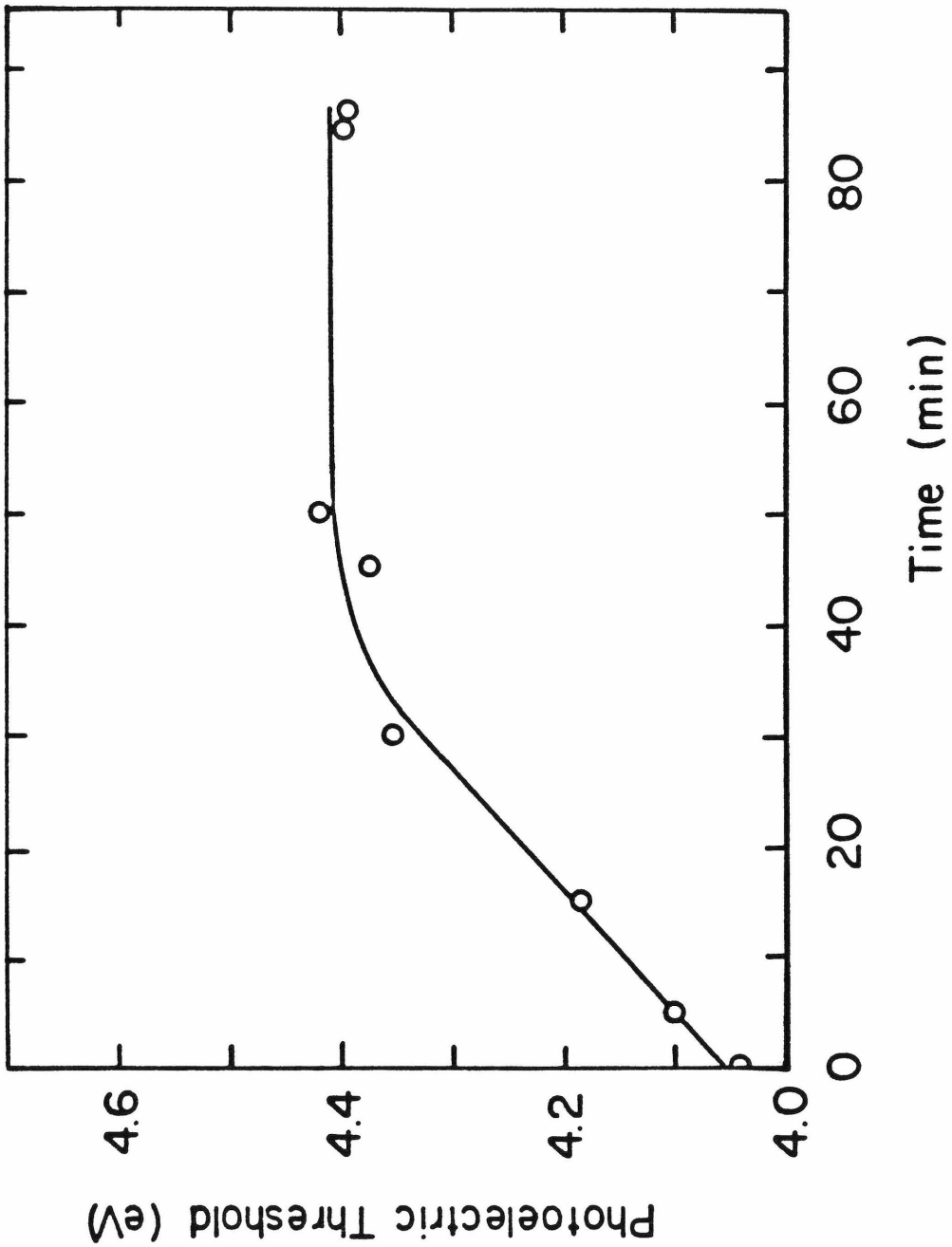
Photoelectric Threshold (eV)
4.0
4.2
4.4
4.6
0
20
40
60
80
Time (min)

formed when the film is exposed to air. This is also true for the tungsten-containing films, although much smaller amounts of hydroxyl are observed to be associated with this metal. In the latter case, WO_2 and WO_3 are the major products.[17] Assignments are based on literature binding energies, peak widths and satellite positions. The C_{1S} peak is referred to 284.4 eV. Most of the carbon impurity appears to be contamination from the vacuum system as the carbon content was found to be consistent with or without metal carbonyls present. In addition, films sputtered with 0.5 keV argon ions showed a decrease in carbon content of $\sim 60\%$ towards the center of the film (relative to the surface value). An increase was again noted at the film-substrate interface. No evidence for iron pentacarbonyl, tungsten carbonyl or their respective carbides was found.

In situ resistivity measurements were found to vary with deposition rate. For example, a 180 Å iron film has a resistivity of $\sim 3 \times 10^{-2}$ ohm cm when deposited at 4 Å min^{-1}. After exposure to air, however, the resitivity increased to that of the oxide, $\sim 6 \times 10^{2}$ ohm cm. The resistance of an iron film as a function of time for a deposition rate of 1 Å min^{-1} is shown in Figure 6.

Electron micrographs of the metal films showed they were smooth and uniformly dispersed. Similar observations were made when substrates were scored and broken to examine the cross section of the film by electron microscopy.

4. Mechanistic Studies with $Fe(CO)_5$. Studies of deposition under a variety of conditions were undertaken in an attempt to clarify and understand the mechanisms involved in film formation. Figure 7

FIGURE 6. (a) Plot of resistance versus time for iron films deposited at ~ 1 Å min^{-1}, (b) Expansion of (a) to show period of growth after light was removed.

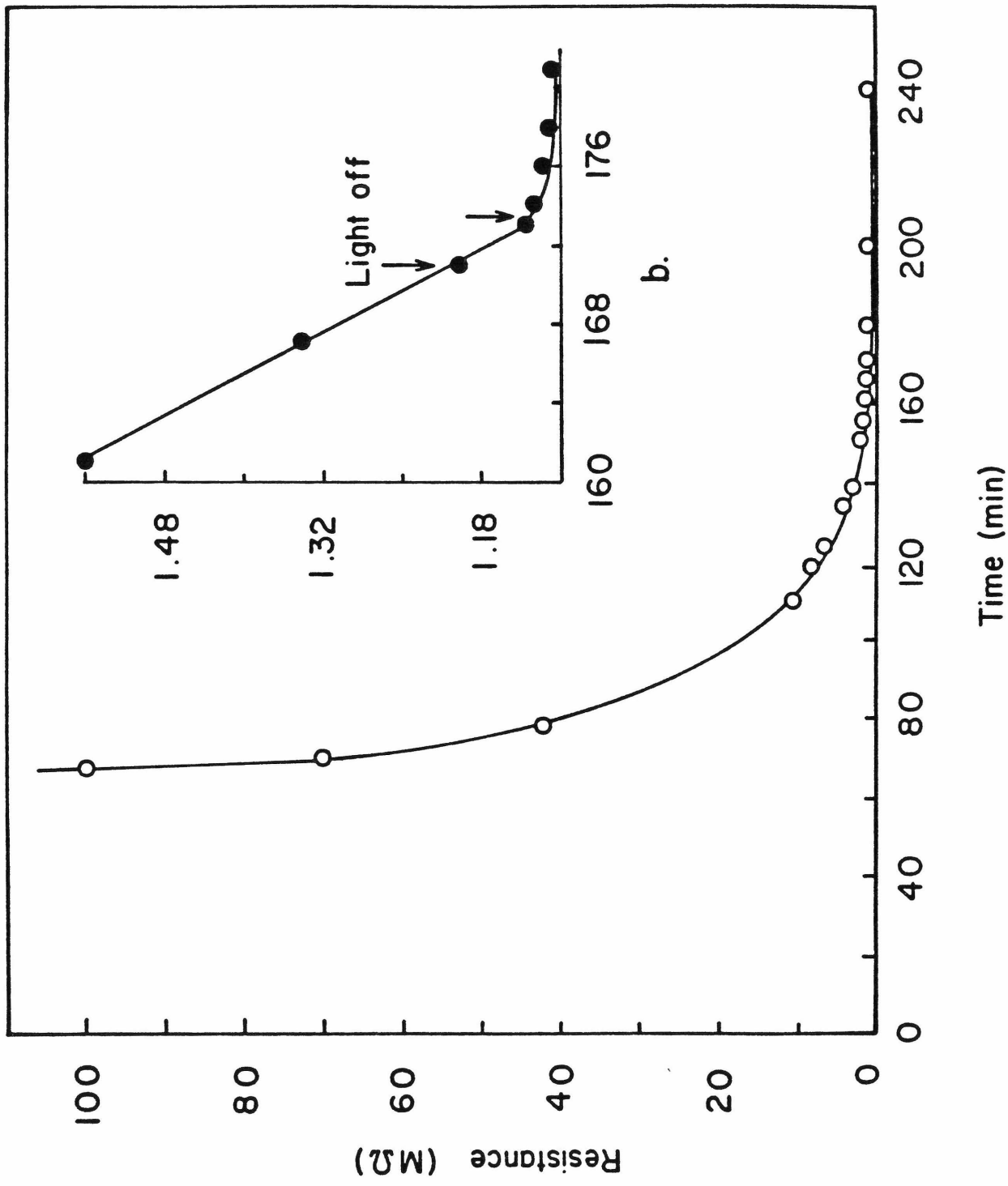
Resistance (MΩ)
0
20
40
60
80
100
0
40
80
120
160
200
240
Time (min)
a.
Light off
1.48
1.32
1.18
160
168
176
b.

FIGURE 7. Plot of iron film thickness versus photon energy. Thickness has been corrected to photon flux. Soda-lime glass substrates were irradiated in the presence of 10^{-2} Torr $Fe(CO)_5$ for 90 min. Dotted line indicates projected film thickness calculated from 4 Å/min if window had not prevented growth.

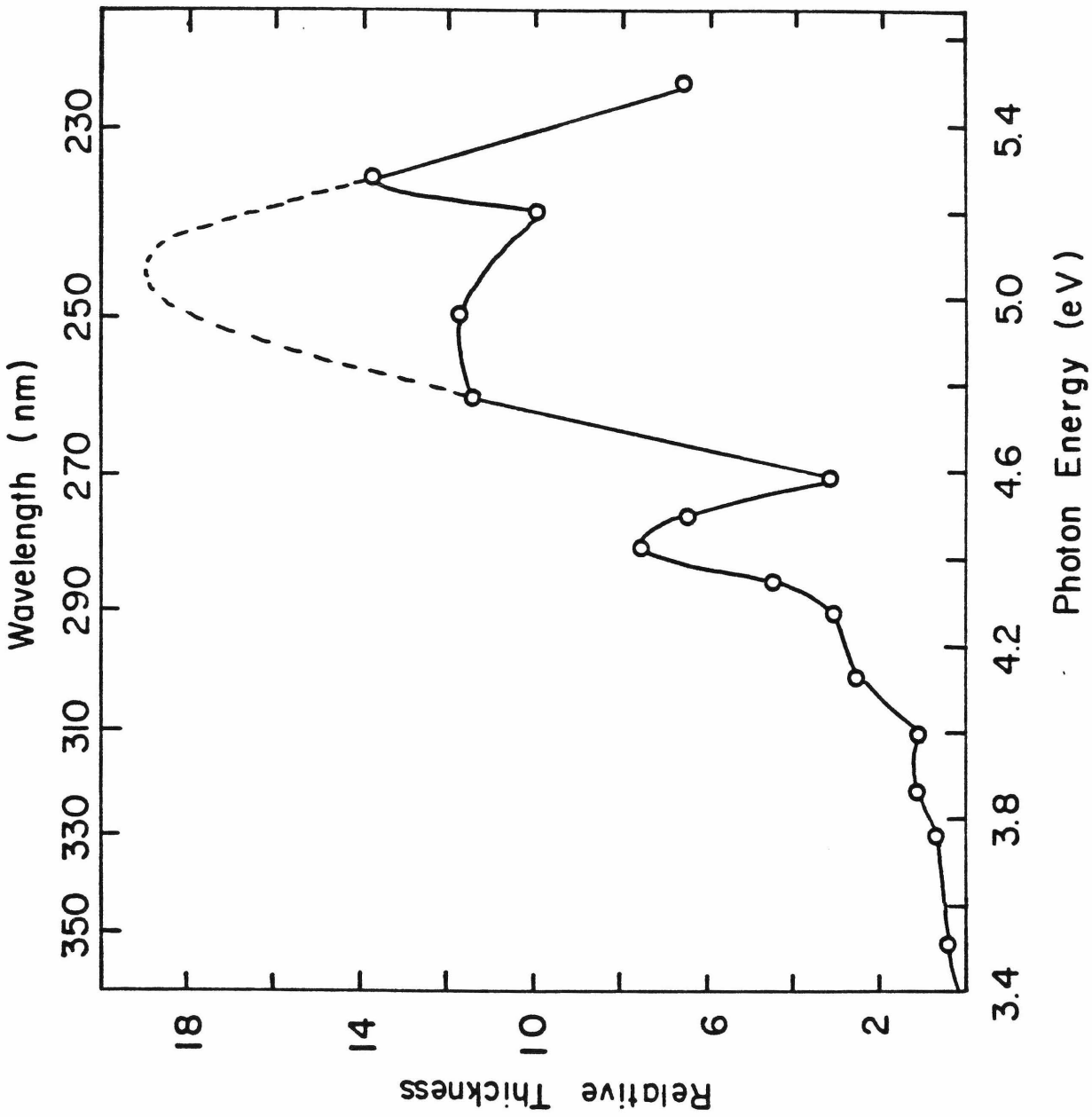
Wavelength (nm)
350 330 310 290 270 250 230
Photon Energy (eV)
3.4 3.8 4.2 4.6 5.0 5.4
Relative Thickness
2 6 10 14 18

illustrates how the thickness of the iron film changes with photon energy at 273° K. In all cases the substrate was irradiated in the presence of 10^{-2} Torr $Fe(CO)_5$ for 90 minutes. Throughout these experiments no change in temperature was registered by the thermocouple. At a photon energy of 5.12 eV and with 10^{-2} Torr $Fe(CO)_5$ a constant deposition rate of 4 Å min^{-1} was measured. Varying the metal carbonyl pressure at 297° K resulted in an increase in deposition (Figure 5) but the relationship is non-linear and no simple function could be fit to the data. Film thickness did, however, vary linearly with photon flux, at 10^{-2} Torr $Fe(CO)_5$.

Effects of adding bath gases were studied at 297° K with photon fluxes and irradiation times reduced from above. Carbon dioxide, argon, carbon monoxide and dimethylphenylphosphine were chosen. CO_2 and argon were not expected to inhibit film growth while CO and the phosphine could react with metal species possibly inhibiting film growth. The results showed that a 40 Å iron film was formed at 1×10^{-2} Torr $Fe(CO)_5$ alone. When an equal amount of CO was admitted this value dropped to 30 Å, and decreased further to 25 Å when the CO pressure was doubled. Addition of 2×10^{-2} Torr dimethylphenylphosphine resulted in a film thickness of only 11 Å in contrast to the 40 Å obtained with $Fe(CO)_5$ alone. The opposite effect was observed when CO_2 was introduced: 2×10^{-2} Torr CO_2 doubled the film thickness to 80 Å. Little effect was observed with argon; addition of 1×10^{-2} Torr increased the thickness by 10% while 2×10^{-2} Torr decreased it by 15%. These results are discussed further in the next section.

Experiments which would distinguish between photodecomposition

FIGURE 8. Plot of iron film thickness as a function of $Fe(CO)_5$ pressure. Soda-lime glass substrates were irradiated at 5.1 eV photon energy for 90 min in (a) and for 30 min in (b).

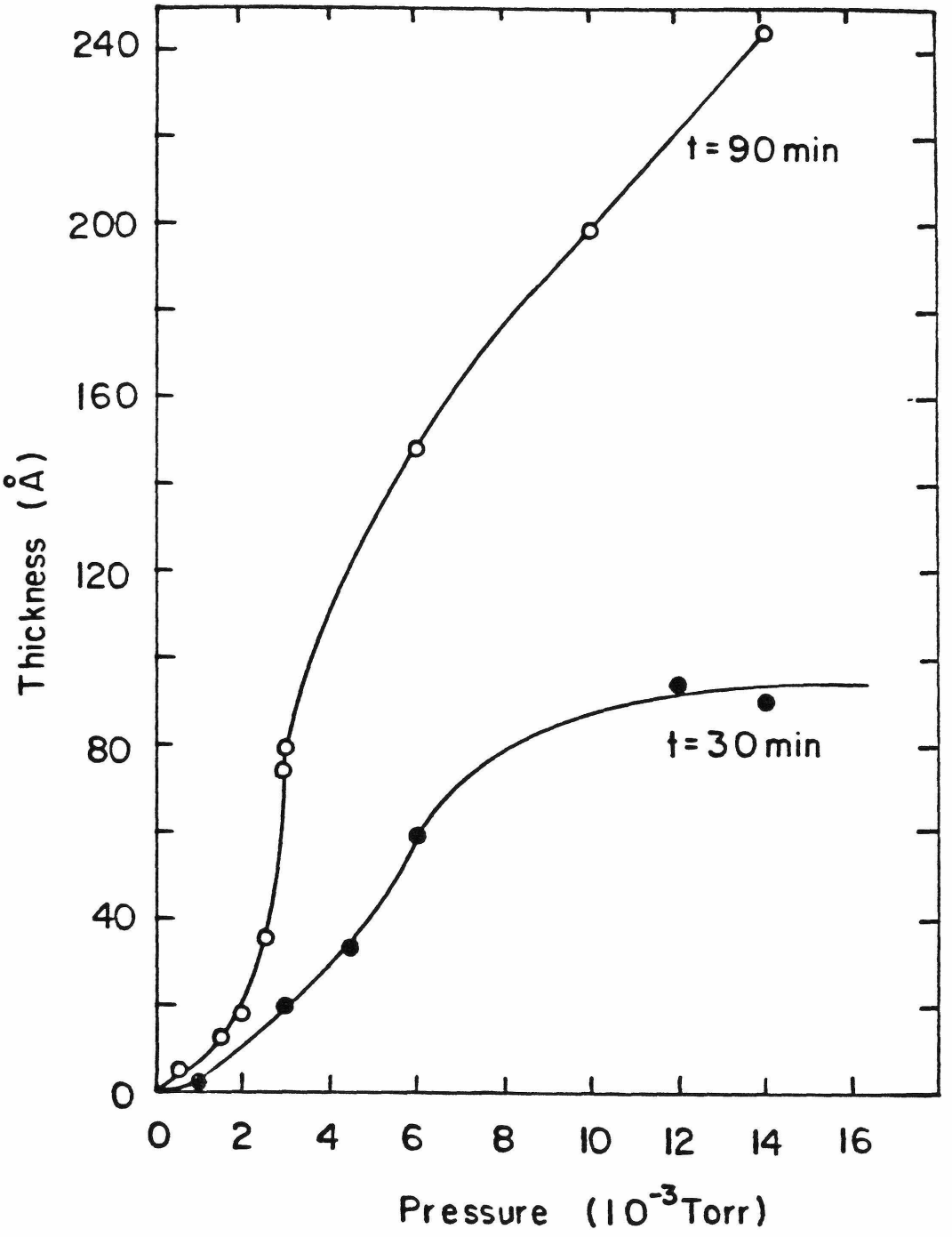
240
200
160
120
80
40
0
Thickness (Å)
t = 90 min
t = 30 min
0
2
4
6
8
10
12
14
16
Pressure (10⁻³Torr)

in the gas phase and surface photoprocesses were difficult to devise. The gas phase absorption spectrum of $Fe(CO)_5$ is shown in Figure 3. At 9×10^{-2} Torr of $Fe(CO)_5$ in a static gas cell this spectrum was very similar to the solution phase spectrum[18] although the extinction coefficients were a factor of three lower at 5.1 eV. At lower pressures, however, in both the gas cell and with better resolution in the flow system, structure was observed in the absorption spectrum. Distinct peaks were visible at ~ 245 nm and ~ 285 nm. This may be attributed to the fact that the concentration of photodecomposition products is very low at these pressures, especially in the flow system where products are continually removed from the light path.

At 10^{-2} Torr $Fe(CO)_5$ there are $\sim 3 \times 10^{14}$ molecules cm^{-3} with a mean free path of 7×10^{-2} cm. An absorbance of 5×10^{-4} cm^{-1} is calculated at 4.3 eV. With a photon flux of $\sim 6 \times 10^{15}$ photons cm^{-2} s^{-1} at this energy approximately 10^{12} molecules cm^{-2} s^{-1} could reach the surface in a static system, assuming unity quantum yield for photodecomposition. If photodecomposition in the gas phase is the major pathway then equal amounts of deposition would be expected on a glass surface as on a silver surface, discounting differences due to reflectivity and sticking probabilities. Simultaneous irradiation of adjacent samples of silver and glass at 4.31 eV resulted in an observable film on the silver only. X-ray microprobe analysis reveals a 15:1 preference for deposition of iron on the silver. It is of interest to note, however, that this preference does correlate with 45:1 ratio of photoelectrons at this energy (see Figure 3) when the effect of the film electron yield is considered.

5. Mechanistic Studies With Other Organometallic Compounds. $Mo(CO)_6$ has a greater range of thermal stability[19] than does $Fe(CO)_5$. Consequently molybdenum deposition was studied as a function of temperature. Figure 9 shows that a plot of film thickness versus temperature yields a straight line. Again it is noted that the yield of photoelectrons for the glass and the growing film also increases with temperature. Below $\sim 5°$ C the $Mo(CO)_6$ pressure dropped rapidly, indicating that $Mo(CO)_6$ condensed on the cooled surfaces.

No deposition was observed when ferrocene or nickelocene was used as the reactive organometallic compound. Irradiation with $(\eta^5\text{-}C_5H_4CH_3)Mn(CO)_3$ present led to formation of manganese films, but these were found to be non-conducting.

Composition of mixed metal films on a single substrate were also studied in an attempt to probe mechanistic pathways. Equal mixtures of two metal carbonyls with different extinction coefficients were used.[20] Table 2 gives the percentage composition of each found in the mixed films and the extinction coefficients measured in the gas phase at 5.1 eV. The composition was determined from RBS data, an example of which is shown in Fig. 10 for iron and tungsten. These compositions were reproducible to within $\sim 5\%$. The order, in decreasing amounts present in the films, is Fe > Mo > Cr > W.

6. Deposition With Low Energy Electrons Generated From an Electron Gun. The possibility that low energy electrons incident on a surface could induce deposition was investigated. In these experiments low energy electrons directed at a soda-lime glass substrate in the presence of 10^{-2} Torr $Fe(CO)_5$ lead to formation of a thin iron film.

i) Percent Composition of Binary Films[a]

	Fe	Mo	Cr
W	67 / 33	94 / 6	90 / 10
Cr	82 / 18	60 / 40	
Mo	59 / 41		

ii)

Metal Carbonyl	Extinction Coefficient at 5.1 eV[b]
$Fe(CO)_5$	5.5×10^3
$Cr(CO)_6$	1.9×10^4
$Mo(CO)_6$	1.3×10^4
$Co(CO)_6$	1.0×10^4

a) Formed by irradiation of a 1:1 mixture of the corresponding carbonyls at 5:1 eV.

b) Units are ℓ $mole^{-1}$ cm^{-2}.

FIGURE 9. Plot of molybdenum film thickness as a function of substrate temperature. Soda-lime glass substrates were irradiated in the presence of 5×10^{-3} Torr $Mo(CO)_6$ for 60 min.

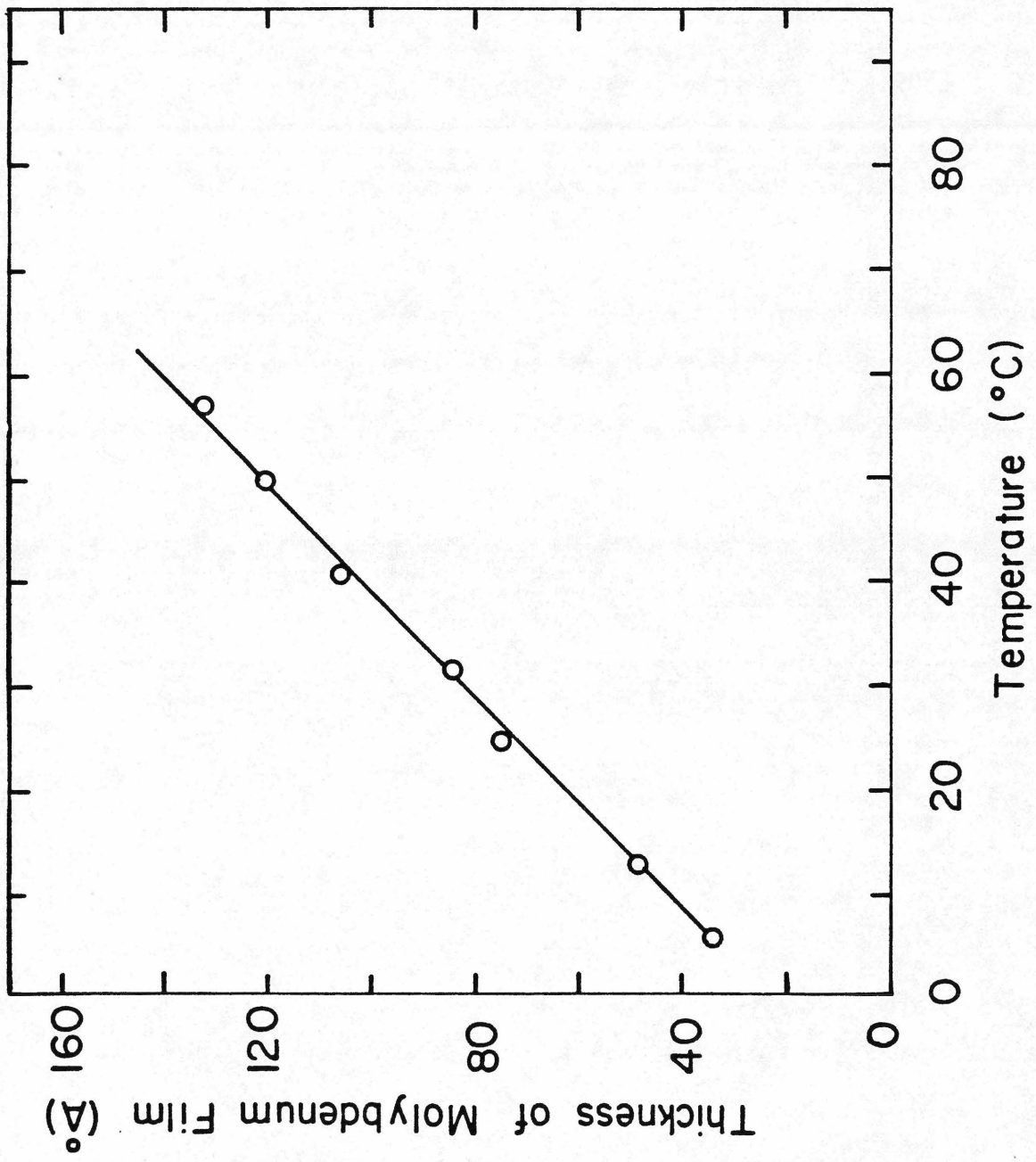
Thickness of Molybdenum Film (Å)
160
120
80
40
0
0
20
40
60
80
Temperature (°C)

When the filament was positively biased to prevent electron emission no metal atoms were detected. The substrate temperature did rise to $\sim 40^\circ$ C, which is still too low for thermal decomposition. However, to prevent any contamination by thermal products, the substrate was cooled to 22° C. No change in deposition was observed. For a 1:1 mixture of $Fe(CO)_5$ and $Mo(CO)_6$ RBS data show that the film was composed of 79% iron and 21% molybdenum. This compared with 59% iron and 41% molybdenum obtained in the photoassisted deposition.

7. Photolysis at Low Temperatures. Additional experiments were carried out to investigate the photolysis of adsorbed metal carbonyl species at low temperature. As mentioned above, when the substrate was cooled below 5° C $Mo(CO)_6$ adsorbed on the cold surfaces. 1.2×10^{-2} Torr $Mo(CO)_6$ was admitted to the vacuum chamber and the substrate temperature lowered with the pump closed. After $Mo(CO)_6$ condensed all remaining gases were pumped out. The pump was closed and the sample irradiated at 5.1 eV photon energy for 30 minutes at 200° K. The pump remained closed while the substrate was allowed to warm up. Trace amounts of Mo were detected on the substrate. A similar experiment was performed with $Fe(CO)_5$ at 185° K, but this time the pump was kept open all the time and a constant flow of $Fe(CO)_5$ was maintained, until irradiation was complete. The resulting iron film was ~ 6 monolayers thick. These observations agree with those obtained in matrix isolation experiments[21] where CO is lost during UV photolysis. Upon warming, however, the subcarbonyl species recombines in the presence of CO to reform the carbonyl. Since recombination was possible in the $Mo(CO)_6$ experiment less than a

FIGURE 10. Rutherford backscattering spectrum showing the composites of an iron/tungsten film. The composition was calculated using the height of the silicon edge as a reference.[12]

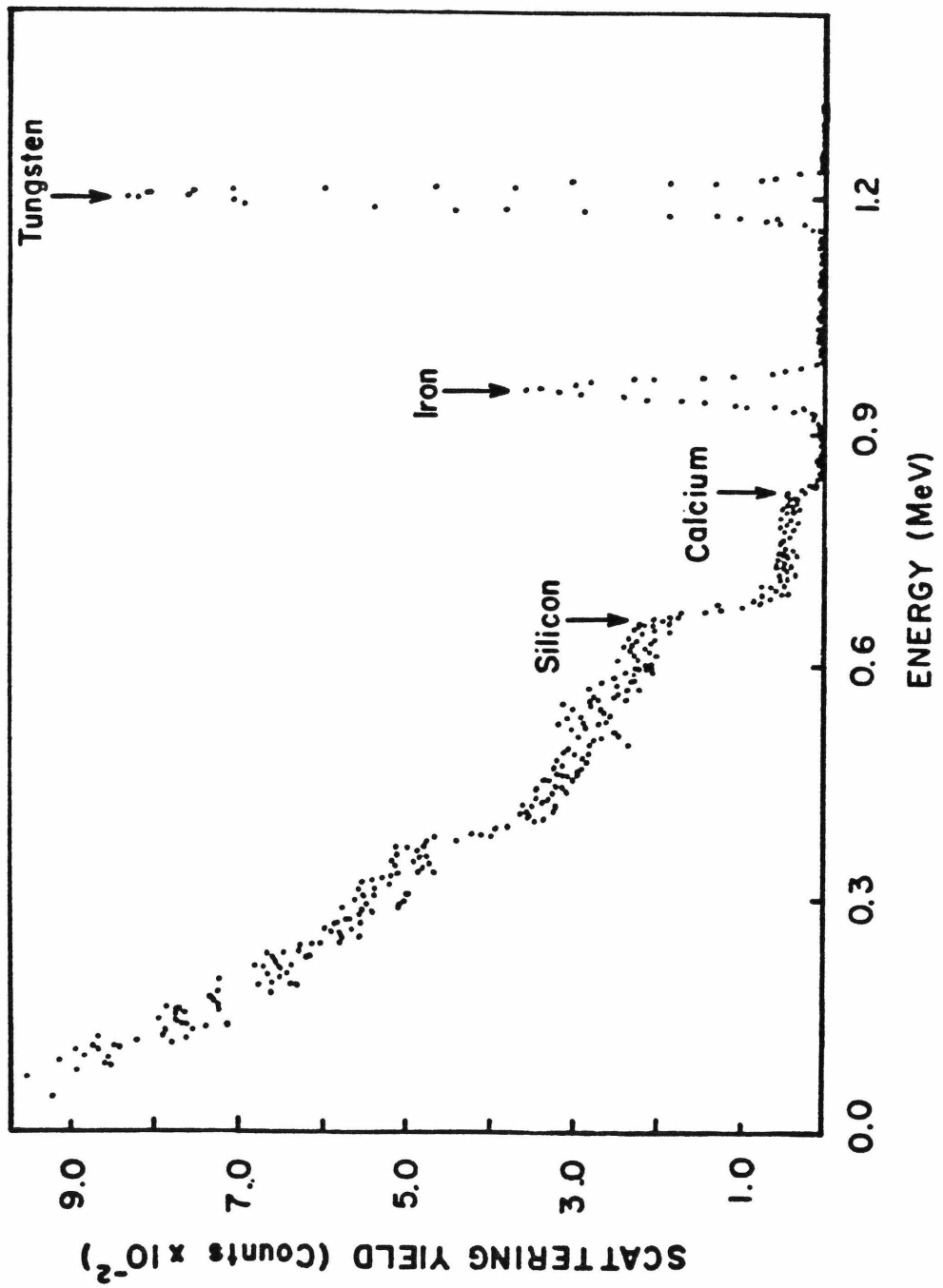
Tungsten
Iron
Calcium
Silicon
SCATTERING YIELD (Counts x 10^{-2})
9.0
7.0
5.0
3.0
1.0
0.0
0.3
0.6
0.9
1.2
ENERGY (MeV)

monolayer of metal was detected, but when the CO was removed (as in the $Fe(CO)_5$ experiment) a larger yield was obtained.

IV. Discussion

The results of these experiments show that organometallic compounds can be selectively decomposed by both UV light and low energy electrons.

1. Deposition With Low Energy Electrons. Low energy electrons can react with the organometallic compounds by a mechanism involving dissociative electron attachment. The coordinately-unsaturated anion can interact strongly with a surface, thus enabling further decomposition to occur. This is illustrated in Scheme 1, in which S in the surface.

Scheme 1

$$e(S) + h\nu \rightarrow e \quad \text{(a)}$$

$$M(CO)_x + e \rightarrow M(CO)^-_{x-1} + CO \quad \text{(b)}$$

$$M(CO)^-_{x-1} + S \rightarrow M(CO)_{x-1} - S + e(S) \quad \text{(c)}$$

$$M(CO)_{x-1} - S \rightarrow M - S + (x-1)\,CO \quad \text{(d)}$$

We have also investigated the gas phase reactions of metal carbonyls with thermalized electrons, using the techniques of ion cyclotron resonance spectroscopy.[22] These show that rate constants for reaction

(b) in Scheme 1 are $\sim 2 \times 10^{-7}$ cm^3 mol^{-1} s^{-1} for all the metal carbonyls studied here. Cross sections for the formation of $Fe(CO)_4^-$ have been examined by Compton and Stockdale.[23] Onset of $Fe(CO)_4^-$ production occurs at zero electron energy, rises to a maximum at ~ 0.5 eV and decreases rapidly at higher energies. The electrons, therefore, have to be close to thermal energies before dissociative electron capture can take place.

2. Deposition With UV Light. Film thickness, after correction for photon flux, is found to be dependent on photon energy. No temperature increase was observed during the deposition process. This is consistent with calculations (based on the analysis of Lichtman et al.[5]) of the maximum temperature rise on surfaces which are irradiated by a given photon flux density. The maximum radiant power used in these experiments was 6 mW cm^{-2} and most experiments were carried out with less than 4 mW cm^{-2} at photon energies of between 4 eV to 5.2 eV. Since the emissivity of glass is 0.8 in this region, a maximum increase of 8° C is expected for a 4 mW cm^{-2} beam focused on the glass substrate. This would not increase substantially for the beam focused on a thin metal film. Therefore, the photoassisted deposition process is thought to be a true quantum effect and not a thermal process.

Figure 11 illustrates the thickness of iron film divided by photon flux, quantum yield of photoelectrons, and the extinction coefficients of $Fe(CO)_5$, versus photon energy. It can be seen that both photoelectric yield and extinction coefficients increase with energy. The thickness,

however, does not parallel either one individually. Deposition appears to be a composite of the two processes. In addition, the quantum yield is greater than one, indicating that the amount of deposited material exceeds that available by photodecomposition and dissociative electron attachment. To assist in evaluating the important stages in the deposition process, a detailed kinetic analysis was performed. This is presented in the appendix and a summary of the salient points are discussed below.

As previously mentioned, a useful way to understand photoassisted deposition of metals from organometallic compounds is to examine it in three stages: initiation, propagation and termination of film growth. The initiation stage has been shown to depend upon photons and photoelectrons. No evidence is found for thermal initiation or photodecomposition of adsorbed species. Equations 1 and 2 describe initiation where $h\nu$ is the energy of the irradiating light and S is the surface site. Initially, S represents a site on the clean substrate but this rapidly becomes a metal site as the film grows. An electron within the allowed energy range for dissociative electron capture by $Fe(CO)_5$ is given as e^-_{th}.

$$Fe(CO)_5 + h\nu \underset{k_{-1}}{\overset{k_1}{\rightleftharpoons}} Fe(CO)_4 + CO \qquad (1)$$

$$Fe(CO)_5 + e^-_{th} \underset{k_{-2}}{\overset{k_2}{\rightleftharpoons}} Fe(CO)_4^- + CO \qquad (2)$$

$$Fe(CO)_4^- + S \underset{k_{-3}}{\overset{k_3}{\rightleftharpoons}} Fe(CO)_4S + e^- \qquad (3)$$

$$Fe(CO)_4 + S \underset{k_{-4}}{\overset{k_4}{\rightleftharpoons}} Fe(CO)_4S \qquad (4)$$

The absorption spectrum (Figure 3) and kinetic data[22] for reactions (1) and (2) are known. At 5.1 eV in 10^{-2} Torr $Fe(CO)_5$ photodecomposition in the gas phase is estimated at 1×10^{13} cm^{-3} s^{-1}. This is derived by assuming a quantum yield of unity for photodecomposition and calculating a value of 3×10^{-3} cm^{-1} for absorbance. This, however, represents an upper bound on the process, since the irradiating area is ~ 0.25 cm^2 and the residence time in the vacuum system < 0.5 s. Consequently it is highly probable that only a fraction of the molecules which are photodecomposed within the mean free path of the substrate (7×10^{-2} cm), reach the surface. It is known that $Fe(CO)_4$ reacts with $Fe(CO)_5$, presumably in a 3-body process, to form $Fe_2(CO)_9$. This is supported by the gas phase absorption spectrum of $Fe(CO)_5$. At high pressures the spectrum closely resembles the solution phase spectrum.[18] However, at low pressures (10^{-2} Torr), spectral features are resolved[24] and the spectrum can be identified as that of the D_{3h} $Fe(CO)_5$ molecules[25] with little or no contamination from photoproducts. At higher pressures the spectrum gives evidence of a second species, which may be small amounts of $Fe_2(CO)_9$.

Equation 2 describes the reaction of photoelectrons with $Fe(CO)_5$. This can occur via the mechanism shown in Scheme 1. Photoelectrons are generated within a range of energies depending on the irradiating

photon energy. Epithermal electrons must underg energy loss prior to attachment; at low pressures this is the rate limiting step in the attachment process.[22] At 5.1 eV the yield of photoelectrons after only a few minutes of deposition (Figure 4) is 3×10^{11} electrons cm^{-2} s^{-1}. Again, the irradiating area is 0.25 cm^2. It would appear that this yield is the limiting factor in the formation of $Fe(CO)_4^-$. However, this may not be the case since introduction of CO_2 doubled the film thickness. It is known that CO_2 effectively thermalizes electrons via a temporary attachment process.[26] Consequently, this suggests that production of photoelectrons per se is not the limiting step, but that production of photoelectrons within the necessary energy range for attachment is critical. The important observation, however, is that this doubling of film thickness by CO_2, and the slight enhancement by low pressures of argon, indicate that the electron attachment and photodecomposition initiation steps are occurring at competitive rates.

The remaining steps (3) and (4) are difficult to probe. Since cross-sections for electron capture are so large it is highly probable that the $Fe(CO)_4^-$ species is formed within 20-30 Å of the surface. This charged $Fe(CO)_4^-$ species would be strongly attracted to the surface by formation of an image charge, while the neutral $Fe(CO)_4$ would not. This would be especially true for those species formed some distance from the surface.

The propagation steps can be described by equations 5-7.

$$Fe(CO)_4\,S \underset{k_{-5}}{\overset{k_5}{\rightleftharpoons}} \overset{(CO)_n}{\underset{\diagdown}{Fe}} - S + (4-n)CO \qquad (5)$$

$$\overset{(CO)_n}{\underset{\diagdown}{Fe}} - S + h\nu \underset{k_{-6a}}{\overset{k_{6a}}{\rightleftharpoons}} FeS + n\,CO \qquad (6a)$$

$$\overset{(CO)_n}{\underset{\diagdown}{Fe}} - S \underset{k_{-6b}}{\overset{k_{6b}}{\rightleftharpoons}} FeS + n\,CO \qquad (6b)$$

$$FeS + Fe(CO)_5 \xrightarrow{k_7} \overset{(CO)_m}{\underset{\diagdown}{Fe}} - FeS + (5-m)CO \qquad (7)$$

To be quite general the process of ligand removal has been divided into two steps, reactions 5 and 6a/6b. To understand these processes it is instructive to examine the thermodynamics of the initiation process.

Reaction (2) is approximately thermoneutral[27] but reaction (3) is exothermic. This can be crudely determined from electron affinity and photoelectric threshold (E_t) data. The electron affinity of $Fe(CO)_4$ is ~ 2.4 eV[27] and E_t can be taken as ~ 4.2 eV, resulting in a ΔH of

$$\Delta H = EA[Fe(CO)_4] - E_t \qquad (8)$$

~ -1.8 eV for this reaction. Since the remaining Fe-CO bonds are relatively weak[27] this would imply that two or three metal-ligand bonds could be broken in the adsorption process.

Similarly, once $Fe(CO)_4$ reaches the surface, formation of $Fe(CO)_4S$ is exothermic by the $Fe(CO)_4$–S bond energy. On the glass surface this may be relatively low, although the value would depend on the specific surface site. The exothermicity is estimated as ~ 0.8 eV if this is a

metal site.[28] Consequently, the propagation steps may be different depending on the source of $Fe(CO)_4S$. In neither case is the exothermicity large enough to account for loss of all the ligands. Thus there are two possibilities for complete removal of CO. The first involves a thermal mechanism, whereby once one ligand is lost the remaining CO ligands are lost in rapid succession. This is supported by evidence from Brenner et al.[29] They observe in temperature programmed decomposition (TPDE) studies that all ligands in Group VIB hexacarbonyls on silica are lost in rapid succession, yielding a single peak in the TPDE spectrum. The authors attribute this to one of two reasons: either loss of the initial ligands is the rate determining step, that is, the first ligands have stronger bonds, or all the ligands have approximately the same activation energy for bond cleavage. This would account for the fact that no CO is observed in the films. When $(\eta^5\text{-}C_5H_4CH_3)Mn(CO)_3$ is the reactant organometallic a non-conducting film is formed, yet X-ray microprobe analysis shows that large quantities of manganese are present. The CO bond strengths in this compound are similar to those in $Fe(CO)_5$ and Group VIB hexacarbonyls, but the $(\eta^5\text{-}C_5H_4CH_3)$-Mn bond strength is much greater.[27] Thus it is likely that this stronger bond is not broken in the propagation step and the film is composed of manganese atoms surrounded by organic moieties.

A second possibility, which is not mutually exclusive, is that the ligands remaining after adsorption of the iron carbonyl species are

removed by a quantum photodesorption process (reaction 6a). The cross-section for a similar reaction is shown to increase sharply above ~ 4 eV[30] although the quantum yield in general is very small (10^{-9} - 10^{-7} molecules cm^{-2} s^{-1}). Thus photodesorption could enhance the rate of ligand removal.

Examination of data in Figure 6b suggests that another process, which continues in the dark, may be occurring. The rapid decrease in film resistance continues for approximately two minutes after removal of light. At the end of this time, however, the surface is apparently poisoned so that termination of growth occurs. The time could be interpreted as that required to poison the surface by residual vacuum gases such as H_2O, O_2, CO, etc. at a base pressure of 10^{-8} Torr. This would imply that film growth is autocatalytic and equation 7 describes a process whereby the coordinately-unsaturated metal sites may decompose metal carbonyls. Many turnovers may result before the surface sites are rendered inactive. It is, however, evident that some other process is necessary to keep the surface active.

Termination steps are described by equations (9)-(11).

$$\text{Fe - S + M} \underset{k_{-8}}{\overset{k_8}{\rightleftharpoons}} \text{MFe - S} \tag{9}$$

$$\text{M + Fe(CO)}_4 + \text{Fe(CO)}_5 \underset{k_{-9}}{\overset{k_9}{\rightleftharpoons}} \text{Fe}_2\text{(CO)}_9 + \text{M} \tag{10}$$

$$\text{M + Fe(CO)}_4 \underset{k_{-10}}{\overset{k_{10}}{\rightleftharpoons}} \text{M - Fe(CO)}_4 \tag{11}$$

Here M represents an impurity in the system or a buffer gas. For

example, the presence of any large buffer gas could enhance reaction (10), while only reactive gases could affect reactions (9) and (11). The overall effect of a buffer gas on the deposition process, however, can only be determined by examining the overall rate equations.

For the initiation process the overall rate equation for formation of $Fe(CO)_4S$ in the absence of a buffer gas is derived in the Appendix. The result is given by equation (12)

$$[Fe(CO)_4S] = \frac{I[S]}{k_{-4}+k_5}\left(k_3 k_F k_0 [Fe(CO)_5] + \frac{k_1 k_4 [Fe(CO)_5]}{k_{-1}[CO]+k_4[S]+k_9[Fe(CO)_5]^2}\right) \tag{12}$$

where I is the light intensity, k_F the rate constant for thermalizing electrons by iron pentacarbonyl. It is evident from equation (12) that formation of $[Fe(CO)_4S]$ is directly proportional to light intensity as long as the photon energy exceeds the photoelectric threshold. In the absence of photoelectrons, formation of $[Fe(CO)_4S]$ depends only on the second term in equation (12), giving equation (13)

$$[Fe(CO)_4S] = \frac{I[S]k_1 k_4 [Fe(CO)_5]}{(k_{-4}+k_5)(k_{-1}[CO]+k_4[S]+k_9[Fe(CO)_5]^2} \tag{13}$$

This also represents photoassisted deposition at higher pressures since the first term in equation (12) is limited by production of electrons in the appropriate energy range for attachment. Consequently increasing $[Fe(CO)_5]$ would disproportionally increase the photodecomposition term, although formation of $Fe_2(CO)_9$ tends to mediate this increase

($k_9[Fe(CO)_5]^2$ term in the denominator). Raising the temperature of the substrate only increases the photoelectric term in equation (12) since production of photoelectrons from the substrate and the film increases rapidly with temperature. The rate constants k_3 and k_4 may decrease with increasing substrate temperature.

The effect of adding a buffer gas on the initiation process is determined by examining equation 14 (22b in the Appendix).

$$[Fe(CO)_4S] = \frac{[S]}{k_{-4} + k_5} \{k_0 k_3 I(k_m[M] + k_F[Fe(CO)_5]) + k_4\left(\frac{k_1 I[Fe(CO)_5] + k_{-10}[Fe(CO)_4M]}{k_{-1}[CO] + k_4[S] + (k_9[Fe(CO)_5] + k_{10})[M]}\right)\} . \quad (14)$$

Introducing a bath gas in all cases is seen to decrease the photodecomposition term quite dramatically, especially if reactive species such as CO or Me_2PhP are used. Such reactive molecules have no effect on the photoelectric term since $Fe(CO)_4^-$ does not react with either CO or Me_2PhP. However, CO_2 increases the photoelectric term by thermalizing electrons, thus increasing the yield of coordinately-unsaturated anions. The effect of argon depends on which of the competing initiation processes is dominating. At low pressures argon causes a small increase in the photoelectric term resulting in a larger deposition yield while at higher pressures the decrease in photodecomposition offsets this and less deposition occurs. For these reactions to be

competing the photoelectric and photodecomposition terms must be approximately equal in numerical values. Thus we can get an approximate yield of $\sim 10^{11}$ $Fe(CO)_4S$ molecules per second. Over the course of 10^4 seconds this provides only a monolayer of iron. Since we observe over 200 Å there must be considerable enhancement during the propagation stage.

The above discussion refers only to the initiation process. However, to understand the overall deposition process it is necessary to examine equation 15 governing formation of $Fe(CO)_m$-Fe-S (equation 26 in the Appendix).

$$\frac{d[\overset{(CO)_m}{\overset{|}{Fe\text{-}FeS}}]}{dt} = \frac{k_7 (k_{6a}I + k_{6b})(k_3 k_F k_0 I[S] + \dfrac{k_4 I[Fe(CO)_5]}{k_{-1}[CO] + k_4[S]} + k_9[Fe(CO)_5])}{k_{-6}[CO]^n + k_7[Fe(CO)_5]} [Fe(CO)_5] \tag{15}$$

Thus the deposition process is found to be a complicated function of $Fe(CO)_5$ pressure, in agreement with experimental results. Equation 15 predicts that the rate of $Fe(CO)_m$-FeS production is a non-linear function of light intensity. However, thickness was found to be directly proportional to light intensity. Consequently reaction 6a may not be an important step.

Figure 9 shows the constant increase of film thickness with temperature. This suggests that one of two reactions may, in fact, be a rate limiting step. Production of photoelectrons and reaction 6b both increase

with temperature. Reaction 6b, however, is thought to be the rate determining step since propagation does continue in the dark.

Since expression 15 is so complex it is not surprising that the deposition order of Fe > Cr > Mo > W does not correspond to the order expected from simple photodecomposition (Cr > Mo > W > Fe, or electron attachment reactions (Cr ~ Fe ~ Mo ~ W).[22] From the above discussion, however, the ordering may reflect the kinetics of breaking the remaining CO bonds. This was also shown earlier to be the limiting thermodynamic step for formations of metal atoms on the substrate. It is known that the average bond strengths of $Mo(CO)_6$ and $W(CO)_6$ are much stronger than those of $Cr(CO)_6$ and $Fe(CO)_5$,[28] although no individual bond data are available except for those species derived from $Fe(CO)_5$.[27] Heats of desorption for CO on metal films also yield little information since the mechanisms for CO adsorption differ for each of the metals considered.

V. Conclusion

The mechanisms involved in the UV deposition of thin metal films from organometallic compounds at low pressures have been investigated. Three stages are involved: initiation, propagation and termination of film growth. Initiation can occur via dissociative electron attachment and gas phase photodecomposition. Propagation is effected via removal of CO ligands from the film with subsequent decomposition of the organometallic by surface metal sites. Termination can occur by deactivation of a primary intermediate or deactivation of a surface site. Continual

irradiation, however, prevents inhibition of the deposition process. Larger yields than those obtained here can be achieved by increasing either the photon flux or substrate temperature, or both.

Low energy electrons alone can induce metal film decomposition from organometallic compounds on glass substrates. This methodology can be easily extended to include deposition of non-metallic species since the only requirement is that the molecules dissociatively attach low energy electrons. For example, silicon could be deposited from silicon tetrachloride and silicon etching may be possible using NF_3. It is anticipated that slow secondary electrons generated by a high energy electron beam can similarly effect reactions on surfaces. There is potential for applying both this technique and the photoassisted deposition in a number of areas, most notably those of device fabrication and catalyst formation. Further studies under ultra-high vacuum conditions would be necessary to evaluate the properties of these metal films and to determine the effect of contaminants on the film structure.

APPENDIX

Kinetic Scheme to Describe Photoasisted Deposition of Iron Pentacarbonyl

The following equations are used to describe the photoassisted deposition of iron pentacarbonyl in the presence of a buffer gas, M, and surface site, S.

a) Initiation

$$Fe(CO)_5 + h\nu \underset{k_{-1}}{\overset{k_1}{\rightleftharpoons}} Fe(CO)_4 + CO \qquad (A\text{-}1)$$

$$Fe(CO)_5 + e^- \underset{k_{-2}}{\overset{k_2}{\rightleftharpoons}} Fe(CO)_4^- + CO \qquad (A\text{-}2)$$

$$Fe(CO)_4^- + S \underset{k_{-3}}{\overset{k_3}{\rightleftharpoons}} Fe(CO)_4S + e^- \qquad (A\text{-}3)$$

$$Fe(CO)_4 + S \underset{k_{-4}}{\overset{k_4}{\rightleftharpoons}} Fe(CO)_4S \qquad (A\text{-}4)$$

b) Propagation

$$Fe(CO)_4S \underset{k_{-5}}{\overset{k_5}{\rightleftharpoons}} \overset{(CO)_n}{\diagdown}Fe{-}S + (4-n)CO \qquad (A\text{-}5)$$

$$\overset{(CO)_n}{\diagdown}Fe{-}S + h\nu \underset{k_{-6a}}{\overset{k_{6a}}{\rightleftharpoons}} FeS + n\,CO \qquad (A\text{-}6a)$$

$$\overset{(CO)_n}{\diagdown}Fe{-}S \underset{k_{-6b}}{\overset{k_{6b}}{\rightleftharpoons}} FeS + n\,CO \qquad (A\text{-}6b)$$

$$Fe{-}S + Fe(CO)_5 \xrightarrow{k_7} \overset{(CO)_m}{\diagdown}Fe{-}Fe{-}S + (5-m)CO \qquad (A\text{-}7)$$

c) Termination

$$Fe{-}S + M \underset{k_{-8}}{\overset{k_8}{\rightleftharpoons}} M{-}Fe{-}S + h\nu \qquad \text{(A-8)}$$

$$M + Fe(CO)_4 + Fe(CO)_5 \underset{k_{-9}}{\overset{k_9}{\rightleftharpoons}} Fe_2(CO)_9 + M \qquad \text{(A-9)}$$

$$M + Fe(CO)_4 \underset{k_{-10}}{\overset{k_{10}}{\rightleftharpoons}} M - Fe(CO)_4 \qquad \text{(A-10)}$$

Equation A-2 represents an attachment process, which is preceded by reactions A-2a and A-2b, where e* are epithermal electrons within a particular energy range.

$$M + e^* \xrightarrow{k_m} e_{th} + M \qquad \text{(A-2a)}$$

$$Fe(CO)_5 + e^* \xrightarrow{k_F} e_{th} + Fe(CO)_5 \quad . \qquad \text{(A-2b)}$$

Initially electrons are formed with a range of energies depending on the wavelength of exciting light. The rate of dissociative electron attachment is limited by thermalization of these electrons.[22] The final process, equation A-2, has a rate equal to $k_2[Fe(CO)_5][e_{th}]$ which is described by A-2c, where $[e^*] = k_0 I[S]$,

$$\{k_2[Fe(CO)_5]\}[e_{th}] = \{k_m[M] + k_F[Fe(CO)_5]\}[e^*] \; . \qquad \text{(A-2c)}$$

The kinetics may be deduced by applying steady state approximations to $Fe(CO)_4$, $Fe(CO)_4^-$, $Fe(CO)_4S$ and $\overset{(CO)_n}{\underset{Fe-S}{\swarrow}}$

$$\frac{d[Fe(CO)_4]}{dt} = 0 = k_1 I[Fe(CO)_5] - k_{-1}[Fe(CO)_4][CO] - k_4[Fe(CO)_4][S] +$$

$$k_{-4}[Fe(CO)_4S] - k_9[Fe(CO)_4][Fe(CO)_5][M] + k_{-9}[M][Fe_2(CO)_9]$$

$$- k_{10}[M][Fe(CO)_4] + k_{-10}[Fe(CO)_4M] \qquad \text{(A-11)}$$

$$\frac{d[Fe(CO)_4^-]}{dt} = 0 = k_2[Fe(CO)_5][e_{th}] - k_{-2}[Fe(CO)_4^-][CO] - k_3[Fe(CO)_4^-][S] +$$

$$k_{-3}[Fe(CO)_4S] \qquad \text{(A-12)}$$

Substituting equation A-2c for $k_2[Fe(CO)_5][e_{th}]$ gives A-13.

$$0 = \{k_m[M] + k_F[Fe(CO)_3]\} \quad \{k_0 I[S]\} - k_{-2}[Fe(CO)_4^-][CO]$$

$$-k_3[Fe(CO)_4^-][S] + k_{-3}[Fe(CO)_4S].$$

$$\frac{d[Fe(CO)_4S]}{dt} = 0 = k_3[Fe(CO)_4^-][S] - k_{-3}[Fe(CO)_4S] + k_4[Fe(CO)_4][S]$$

$$-k_{-4}[Fe(CO)_4S] + k_{-5}[\overset{(CO)_n}{\diagup}Fe-S][CO]^{4-n} - k_5[Fe(CO)_4S] \qquad \text{(A-13)}$$

$$\frac{d[\overset{(CO)_n}{\diagup}Fe-S]}{dt} = 0 = k_5[Fe(CO)_4S] - k_{-5}[\overset{(CO)_n}{\diagup}Fe-S][CO]^n - k_6 I[\overset{(CO)_n}{\diagup}Fe-S] +$$

$$k_{-6}[Fe-S][CO]^n \qquad \text{(A-14)}$$

$$\frac{d[Fe\text{-}S]}{dt} = 0 = k_{6a} I[\overset{(CO)_n}{\overset{/}{Fe}}\text{-}S] - k_{-6a}[Fe\text{-}S][CO]^n - k_7[Fe\text{-}S][Fe(CO)_5]$$

$$+ k_{-7}[\underset{(CO)_m}{\overset{\backslash}{Fe}}\text{-}Fe\text{-}S][CO]^{5-m} + k_{-8} I[M\text{-}Fe\text{-}S] - k_8[Fe\text{-}S][M]$$

$$+ k_{6b}[\overset{(CO)_n}{\overset{|}{Fe}}\text{-}S] - k_{-6b}[FeS][CO]^n \qquad \text{(A-15)}$$

Consequently, the rate of formation of the species of interest is given by A-16.

$$\frac{d[\overset{(CO)_m}{\overset{/}{Fe}}\text{-}FeS]}{dt} = k_7[Fe\text{-}S][Fe(CO)_5] - k_{-7}[\overset{(CO)_m}{\overset{|}{Fe}}\text{-}Fe\text{-}S][CO]^{5-m} . \qquad \text{(A-16)}$$

Solving the above equations leads to equations A-17-A-21.

$$[Fe(CO)_4] = \frac{k_1 I[Fe(CO)_5] + k_{-4}[Fe(CO)_4S] + k_{-9}[M][Fe_2(CO)_9] + k_{-10}[Fe(CO)_4M]}{k_{-1}[CO] + k_4[S] + k_9[Fe(CO)_5][M] + k_{10}[M]}$$

(A-17)

$$[Fe(CO)_4^-] = \frac{(k_m[M] + k_F[Fe(CO)_5])(k_0 I[S]) - k_{-3}[Fe(CO)_4S]}{k_{-2}[CO] + k_3[S]}$$

(A-18)

$$[Fe(CO)_4S] = \frac{k_3[Fe(CO)_4^-][S] + k_4[Fe(CO)_4][S] + k_{-5}[\overset{(CO)_n}{\overset{|}{Fe}}\text{-}S][CO]^{4-n}}{k_{-3} + k_{-4} + k_5}$$

(A-19)

$$[\overset{(CO)_n}{\diagup}\!\!\!\diagdown \text{Fe - S}] = \frac{k_5[Fe(CO)_4S] + (k_{-6a} + k_{-6b})[Fe - S][CO]^n}{k_{-5}[CO]^n + k_6 I} \qquad (A\text{-}20)$$

$$[FeS] = \frac{(I+1)(k_{6a} + k_{6b})[\overset{(CO)_n}{\diagup}\!\!\!\diagdown \text{Fe - S}] + k_{-7}[\overset{(CO)_m}{\diagup}\!\!\!\diagdown \text{Fe - Fe - S}][CO]^{5-m} + k_{-8} I[M\text{-Fe-S}]}{k_{-6b}[CO]^n + k_{-6a}[CO]^n + k_7[Fe(CO)_5] + k_8[M]} \qquad (A\text{-}21)$$

Substituting in these five equations and simplifying and solving for $[Fe(CO)_4S]$, $[\overset{(CO)_n}{\diagup}\!\!\!\diagdown \text{Fe–S}]$ and [Fe—S] results in equations A-22 to A-25. Simplification involves examination of the equations and rates in the initiation and propagation steps. For instance the back reactions in equations A-2, A-3, A-5 and A-9 can be considered:

$$[Fe(CO)_4S] = \left(\frac{\{k_{-1}[CO] + k_4[S] + k_9[Fe(CO)_5][M] + k_{10}[M]\}(k_{-4} + k)}{\{k_{-1}[CO] + k_4[S] + k_9[Fe(CO)_5][M] + k_{10}[M]\}(k_{-4} + k_{-5}) - k_4 k_{-4}[S]} \right)$$

$$\frac{k_3}{k_{-4} + k_5} \{(k_m[M] + k_F[Fe(CO)_5]\}\{k_0 I[S]\}$$

$$+ \left(\frac{k_4[S]}{k_{-4} + k_5} \right) \frac{k_1 I[Fe(CO)_5] + k_{-10}[Fe(CO)_4 M]}{k_{-1}[CO] + k_4[S] + \{k_9[Fe(CO)_5] + k_{10}\}[M]} \qquad (A\text{-}22a)$$

This is further simplified by noting that k_{-4} is small in comparison with the remaining denominator in the first multiplicative term. Thus

equation A-22a becomes equation A-22b

$$[Fe(CO)_4S] = \frac{k_3}{k_{-4}+k_5}\left(\{k_m[M]+k_F[Fe(CO)_5]\}\,k_0 I[S]\right) \qquad \text{(A-22b)}$$

$$\frac{k_4}{k_{-4}+k_5}[S]\left(\frac{k_1 I[Fe(CO)_5]^{+} + k_{-10}[Fe(CO)_4M]}{k_{-1}[CO]+k_4[S]+k_9[Fe(CO)_5]+k_{10}[M]}\right).$$

In order to simplify these equations let

$$A = \{k_m[M]+k_F[Fe(CO)_5]\}\,k_0 I[S]$$

and

$$B = [S]\left(\frac{k_1 I[Fe(CO)_5] + k_{-10}[Fe(CO)_4M]}{k_{-1}[CO]+k_4[S]+\{k_9[Fe(CO)_5]+k_{10}\}[M]}\right).$$

Equation A-22b becomes equation A-22c.

$$[Fe(CO)_4S] = \frac{k_3A + k_4B}{k_{-4}+k_5} \qquad \text{(A-22c)}$$

$$[\overset{(CO)_n}{\underset{}{Fe}}\!-\!S] = \frac{k_5\left[\frac{k_3A+k_4B}{k_{-4}+k_5}\right] + (k_{-6a}+k_{-6b})[Fe-S][CO]^n}{k_{6b}+k_{6a}I} \qquad \text{(A-23)}$$

$$[Fe-S] = \frac{k_5\left[\frac{k_3 A + k_4 B}{k_{-4} + k_5}\right] + k_{-8} I[M-Fe-S]}{k_{-6b}[CO]^n + k_{-6a}[CO]^n + k_7[Fe(CO)_5] + k_8[M]} = C \quad (A-24)$$

Therefore the rate of formation of $(\overset{(CO)_m}{Fe-FeS})$ is given by equations A-25 and A-26

$$\frac{d[\overset{(CO)_m}{Fe-FeS}]}{dt} = k_7(C)[Fe(CO)_5] \quad (A-25)$$

In the absence of a buffer gas this becomes equation (A-26)

$$\frac{d[Fe-FeS]}{dt} = \frac{k_7(k_{6a} I + k_{6b}) k_5\left[\frac{k_3 A + k_4 B}{k_{-4} + k_5}\right][Fe(CO)_5]}{(k_{-6a} + k_{-6b})[CO]^n + k_7[Fe(CO)_5]} . \quad (A-26)$$

To simplify A-26 it is reasonable to assume $k_{-4} \ll k_5$. In addition, let $(k_{-6}a + k_{-6b})$ equal k_{-6}. Thus equation A-27 represents the production of $\overset{(CO)_m}{Fe-FeS}$.

$$\frac{d[\overset{(CO)_m}{Fe-FeS}]}{dt} = \frac{k_7(k_{6a} I + k_{6b})(k_3 A + k_4 B)[Fe(CO)_5]}{k_{-6}[CO]^n + k_7[Fe(CO)_5]} \quad (A-27)$$

substituting for A and B results in equation A-28

$$\frac{d[\overset{(CO)_m}{/}Fe-FeS]}{dt} = \frac{k_7(k_{6a}I + k_{6b})(k_3 k_F k_0 I[S] + \left\langle \frac{k_4 I[Fe(CO)_5]}{k_{-1}[CO] + k_4[S] + k_9[Fe(CO)_5]} \right\rangle [Fe(CO)_5]}{k_{-6}[CO]^n + k_7[Fe(CO)_5]} \quad \text{(A-28)}$$

References and Notes

(1) J. B. Nagy, N. Van Eenoo and E. G. Derouane, J. Catalysis, 58, 230 (1979).

(2) C. Jonah, P. Chandra and R. Bersohn, J. Chem. Phys., 55, 1903 (1971).

(3) M. W. Jones, L. J. Rigby, and D. Ryan, Nature, 212, 177 (1960).

(4) T. E. Deutsch, D. J. Ehrlich and R. M. Osgood, Jr., App. Phys. Lett., 35(2),175 (1979).

(5) G. W. Fobel, S. M. Cox, and D. Lichtman, Surface Science, 40, 571 (1973).

(6) C. H. Nicholls and P. A. Leermakers, in "Advances in Photochemistry," vol. 8, p. 315; J. N. Pitts, Jr., G. S. Hammond and W. A. Noyes, Jr., eds., Wiley and Sons, N.Y. (1971).

(7) A. Terenin, Advan. Catal., 15, 227 (1964).

(8) D. R. Sandstrom and S. P. Withrow, J. Vac. Sci. Technol. 14(2), 748 (1977).

(9) F. J. Grunthaner, NBS Spec. Publ. 400-23, ARPA-Workshop IV Surface Analysis for Silicon Devices, Gathersburg, Md. Ap 23-24, 1975; B. Lewis, Rev. Sci. Inst., submitted.

(10) W. K. Chu, J. W. Mayer, and M.-A. Nicolet, "Backscattering Spectrometry," Academic Press, N.Y. (1978).

(11) F. Wooten and R. N. Stuart, Phys. Rev. 186(2), 592 (1969).

(12) R. H. Fowler, Phys. Rev., 38, 45 (1931).

(13) a) J. S. Anderson, E. A. Faulkner, and D. F. Klemperer, Aust. J. Phys., 12, 49 (1969).

b) B. G. Baker, B. B. Johnson and J. L. C. Maire, Surface Science, 24, 572 (1971).

References (continued)

(14) R. Bowman and W. M. H. Sachtler, Surface Science, 24, 350 (1971).

(15) V. R. Suhrman and G. Wedler, Z. Angew. Phys., 14, 70 (1962).

(16) C. R. Brundle, T. J. Chuang, and K. Wandelt, Surface Sci., 68, 459 (1971) and references therein.

(17) a) R. J. Colton and J. W. Rabalais, Inorg. Chem., 15(1), 236 (1976);

b) J. T. Yates, T. E. Madey, and N. E. Erickson, Chem. Phys. Lett., 39(1) (1976).

(18) M. Dartinguenave, Y. Dartinguenave, and H. B. Gray, Bull. Soc. Chim., 12, 4223 (1969).

(19) F. A. Cotton and G. Wilkinson, "Advanced Inorganic Chemistry," p. 684, John Wiley and Sons, N.Y. (1972).

(20) N. A. Beach and H. B. Gray, J. Am. Chem. Soc., 90, 5713 (1968).

(21) J. K. Burdett, J. M. Grzybowski, R. N. Perutz, M. Poliakoff, J. J. Turner, and R. F. Turner, Inorg. Chem., 17(1), 147 (1978).

(22) P. M. George and J. L. Beauchamp, submitted to J. Chem. Phys.

(23) R. N. Compton and J. A. D. Stockdale, Int. J. Mass Spectros. and Ion Phys. 22, 47 (1976).

(24) P. M. George and J. L. Beauchamp, submitted to J. Am. Chem. Soc.

(25) K. F. Purcell and J. C. Katz in "Inorganic Chemistry", W. B. Saunders Co., Philadelphia (1977).

(26) L. G. Christophorou, "Atomic and Molecular Radiation Physics," Wiley and Sons, N.Y. (1971).

References (continued)

(27) P. C. Engelking and W. C. Lineberger, J. Am. Chem. Soc., 101, 5569 (1979).

(28) This is the average metal bond strength found in $Fe_2(CO)_9$ and $Fe_3(CO)_{12}$ as determined by J. A. Connor, Topics in Current Chemistry, 71, 71 (1977).

(29) A. Brenner, D. A. Hucul and S. J. Hardwick, Inorg. Chem. 18(6), 1478 (1979).

(30) B. E. Koel, J. M. White, J. L. Erskine and P. R. Antoniewicz, in "Interfacial Processes: Energy Conversion and Synthesis," M. S. Wrighton, ed. Adv. In Chem. #184. ACS (1980).

(31) E. K. Von Gustorf and F.-W. Grevels, Fortsch. der Chem. Forsch. 13, 366 (1969).

CHAPTER IV

Dissociative Electron Attachment Reactions of Transition Metal Carbonyls and Their Apparent Influence on the Thermalization of Electrons by CO_2

Dissociative electron attachment reactions of transition metal carbonyls and their apparent influence on the thermalization of electrons by CO_2[a]

Patricia M. George and J. L. Beauchamp

Arthur Amos Noyes Laboratory of Chemical Physics,
California Institute of Technology, Pasadena, California 91125

(Received)

Abstract

Dissociative electron attachment rates are measured for the transition metal carbonyls $V(CO)_6$, $Cr(CO)_6$, $Fe(CO)_5$, $Ni(CO)_4$, $Mo(CO)_6$ and $W(CO)_6$. Rates are measured as a function of the pressure of CO_2 added to relax epithermal electrons. Derived thermal rate constants for the process $M(CO)_n \rightarrow M(CO)_{n-1}^- + CO$ are 0.6, 3.0, 2.0, 2.0, 1.3 and 1.2×10^{-7} cm^3 $molecule^{-1}$ s^{-1}, respectively. The differences in these rate constants may be attributed to the different stabilities of the molecular anion with regard to dissociation versus autodetachment. The measured rate of thermalization of electrons by CO_2 varies with the metal carbonyl used and depends on the variation of the dissociative electron capture cross section with electron energy. Each system is thus tightly coupled in that the electron energy distribution is determined not only by collisional processes involving CO_2 but varies as well with the energy dependent depletion of the distribution by reactant species.

---

a) Contribution No.

I. INTRODUCTION

Traditionally, electron-molecule interactions have been important in studying reactions occurring in electric discharges and in planetary and stellar atmospheres. However, it is becoming increasingly essential to expand our knowledge of these processes by examining electron-molecule reactions on a broader scope. This is particularly true when trying to unravel the complexities of plasma deposition and plasma etching. Recent interest has also focused on the problem of electron cooling in gas lasers and the operation of the electron-capture detector (ECD).

The electron capture rates for many molecules are extremely high. For example organohalogen compounds, which are the main electron-capture detection agents, have rate coefficients often reaching $\sim 2 \times 10^{-7}$ cm^3 molecule^{-1} s^{-1}. Thus direct measurement of such processes is difficult. For instance, at 1 Torr pressure the number density of molecules is 3×10^{16} molecules cm^{-3}, which results in a reaction rate of 10^{10} s^{-1}. Consequently, direct monitoring of electron capture processes at 1 Torr requires experiments with picosecond time resolution and indirect methods are usually employed. Lower pressures increase the time scale of the experiment, making it possible to use a variety of techniques to directly monitor electron capture processes. For example, at 10^{-8} Torr attachment is complete in ~10 ms and direct investigations of such processes can be effected in this pressure range with instruments having millisecond time resolution.

A particularly useful technique in this regard is that of ion cyclo-

tron resonance spectrometry. The ICR cell serves as a highly efficient electromagnetic bottle in which electrons can be trapped and cooled with 100% efficiency. The detection time in such a system is ~1-2 ms in order to have reasonable mass resolution. Thus experiments with molecular densities in the 10^9 cm^{-3} range are extremely well-suited to study by ICR techniques. Specifically, this methodology has been useful for investigating pathways which involve radiative and collisional stabilization.[1,2] In addition, it has been observed that dissociative electron attachment occurs at low pressures with nearly the same facility as high pressures because no stabilization is required.[3] No systematic study, however, has been undertaken to investigate these dissociative electron attachment processes at such low pressures.

The mechanism describing dissociative electron attachment is illustrated in Scheme 1. Electrons, with a distribution of energies,

Scheme 1

$$(e^-)^* \xrightarrow{k_1[M]} e^-_{th} + A \underset{k_i}{\overset{k_f}{\rightleftharpoons}} [A^-]^* \xrightarrow{k_d} B^- + C$$

$$(e^-)^* \xrightarrow{k_2[A]} e^-_{th}$$

are thermalized either by the reacting species, A, or a buffer gas, M. Subsequent attachment by molecule A leads to the formation of $[A^-]^*$, which can dissociate to form a neutral and a negative ion or autodetach the electron. In general the lifetime associated with $[A^-]^*$ is too short to observe the species spectroscopically.

The process of electron thermalization is, surprisingly, still not

well characterized, even though many experiments are carried out in excess of buffer gas in order to thermalize the electrons. For instance, studies by electron cyclotron resonance use ~ 5 Torr of a buffer gas such as CO_2 or CH_4. Some attempts, however, have been made to experimentally determine thermalization times as a function of electron energy.[3,4]

The data obtained in swarm experiments by Christophorou and coworkers[3] are illustrated in Figure 1. The thermalizing gas in this case is CO_2, and the rate constant for electron thermalization is plotted versus the mean electron energy. It can be seen that the CO_2 relaxation rate is found to increase to $\sim 3.8 \times 10^{-10}$ cm^3 molecule^{-1} s^{-1} at an average electron energy of ~ 0.8 eV. Warman and Sauer[4] also investigated CO_2 thermalization by studying the process under conditions where the timescale of thermalization was comparable with that of attachment of electrons to CCl_4, i.e., they used the CCl_4 reaction to monitor the CO_2 relaxation rate. They derive a thermalization rate constant of 5.8×10^{-9} cm^3 molecule^{-1} s^{-1}. In this case it appears that the electrons had a wide range of initial energies.

The interest in CO_2 for thermalizing electrons stems from observations that CO_2 is highly efficient at this process. This is due to the fact that CO_2 exhibits temporary non-dissociative electron attachment behavior at low energies. Electron capture occurs into discrete but short-lived autodetaching states of CO_2^-. Autodetachment leaves vibrationally excited CO_2 and an electron with lower energy.[5] Thus CO_2 is found to be efficient at relaxing the electron energy distribution.

FIGURE 1. Thermalization rate constants as a function of mean electron energy for CO_2. Data are taken from ref. 3.

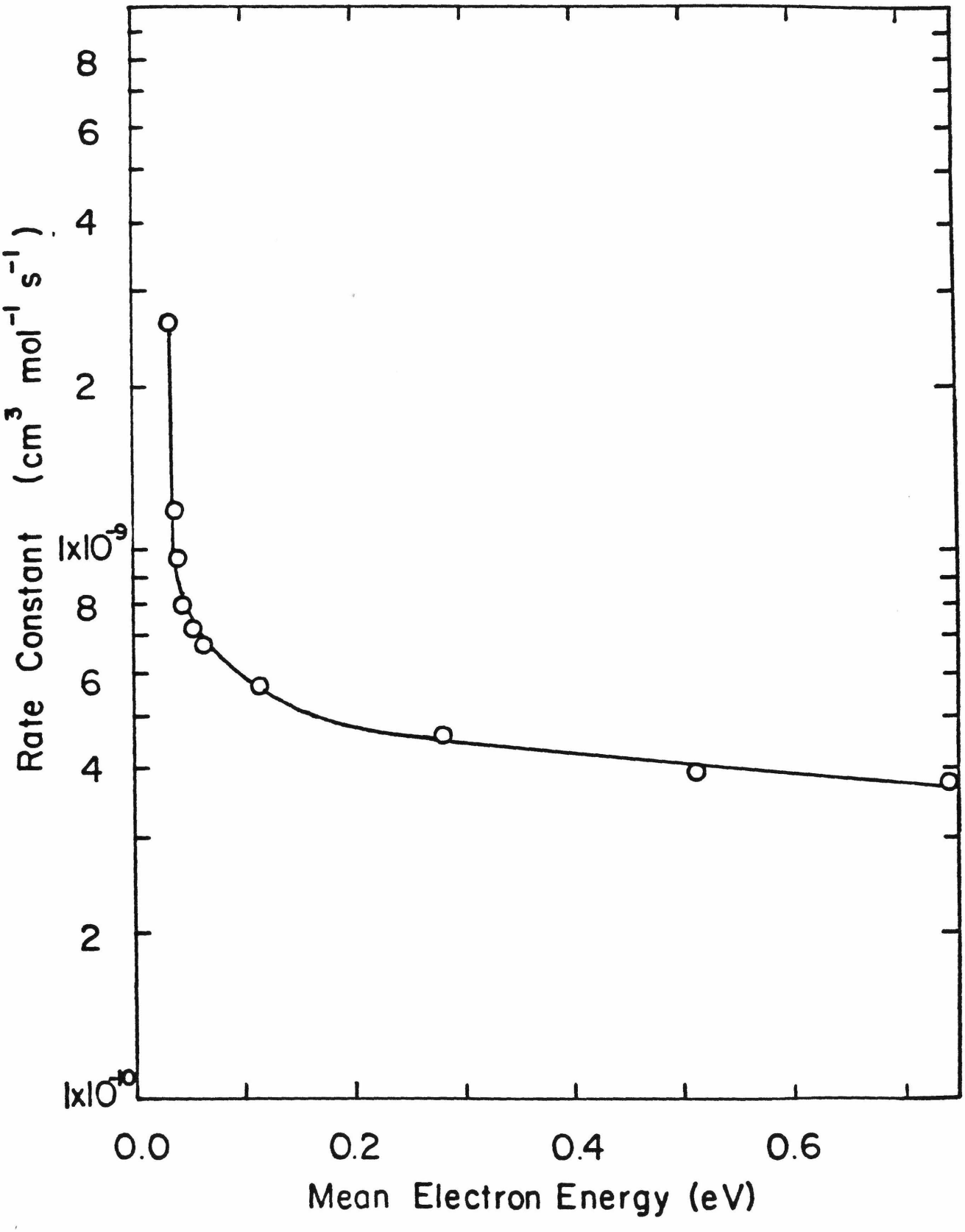
Rate Constant (cm³ mol⁻¹ s⁻¹)
8
6
4
2
1x10⁻⁹
8
6
4
2
1x10⁻¹⁰
0.0
0.2
0.4
0.6
Mean Electron Energy (eV)

This paper presents a study of dissociative electron attachment to transition metal carbonyls. Dissociative attachment rates are measured as a function of CO_2 pressure. By increasing the CO_2 concentration both low and high pressure rates can be found. In addition, the effect of different anionic species on the apparent relaxation rate of epithermal electrons by CO_2.

The carbonyls studied include $V(CO)_6$, $Cr(CO)_6$, $Fe(CO)_5$, $Ni(CO)_4$, $Mo(CO)_6$ and $W(CO)_6$. Negative ion formation from these species has been previously investigated in varying detail. Unimolecular decomposition has been studied by mass spectrometry.[6-9] Parent negative ions are not observed except in $V(CO)_6$.[9] In this particular case the extra electron can occupy a bonding orbital. The dissociative products of $Fe(CO)_5$ and $Ni(CO)_4$ have been examined at higher resolution in gas-phase collision experiments.[10] Onset for formation of both $Fe(CO)_4^-$ and $Ni(CO)_3^-$ occurs at 0 eV but $Ni(CO)_3^-$ peaks at thermal energies while $Fe(CO)_4^-$ continues to increase with electron energy until it reaches a maximum at ~ 0.5 eV. The potential energy surfaces involved for $Fe(CO)_4^-$ production from $Fe(CO)_5$ is illustrated in Figure 2. It can be seen in this case that the process shown in equation 1 is approximately

$$Fe(CO)_5 + e \rightarrow Fe(CO)_4^- + CO \qquad (1)$$

thermoneutral, with the electron affinity of $Fe(CO)_4$ obtained by photoelectron spectroscopy[11] being approximately equal to $D[Fe(CO)_4\text{-}CO]$.

FIGURE 2. Potential energy surfaces involved in formation of $Fe(CO)_4^-$ from $Fe(CO)_5$. Dissociation attachment transitions are allowed only for electron energies between E_1 and E_2.

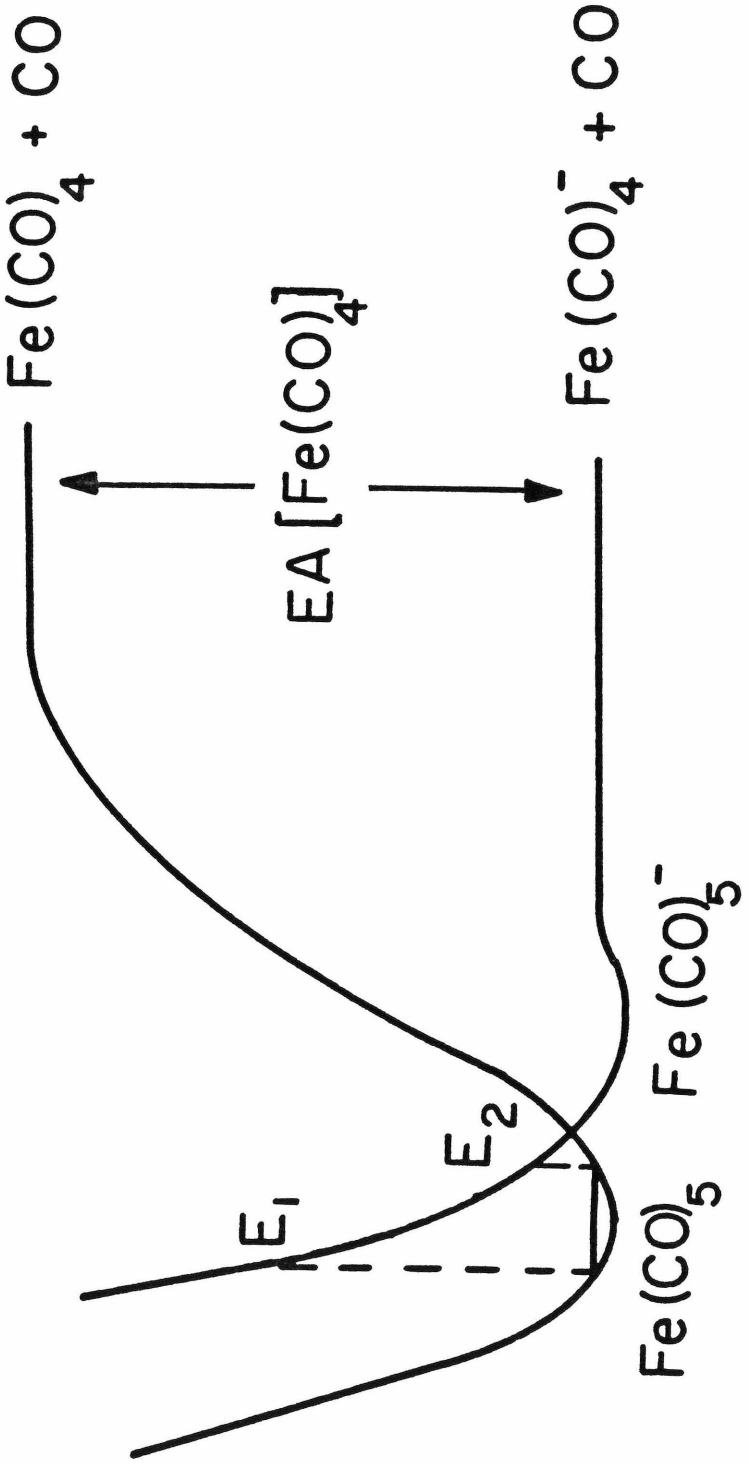
Fe(CO)4 + CO
EA [Fe(CO)4]
Fe(CO)4- + CO
E1
E2
Fe(CO)5
Fe(CO)5-

II. EXPERIMENTAL

The ICR spectrometer used in these studies was built by Caltech shops. It utilizes a 15-in magnet with a maximum field of 23.4 kG, flat three-section ICR cell and standard marginal oscillator detector. Trapped ion ICR techniques have been described elsewhere in detail.[12] Electrons are supplied to the source region of the ICR cell by an initial 3 ms, 70 eV electron beam pulse. The scattered electrons in this region exhibit kinetic energies up to $\sim 0.9\ V_t$ in the direction of the magnetic field, where V_t is the applied trapping voltage. These electrons are constrained to remain on an equipotential of the applied field. They may then react with neutral species to form negative ions which can be trapped in the cell by applied electrostatic fields. Detection is effected after a suitable delay by drifting the ions from the source to the analyzer region where they are observed using a marginal oscillator.

Absolute pressure measurements were made using a Schulz-Phelps ion gauge, calibrated against an MKS Baratron, model 90H1-E capacitance manometer. Overall accuracy in pressure measurements is approximately ± 20% which represents the major source of error in reaction rate constants. All experiments were conducted at ambient temperature (298 K).

Chemicals were obtained commercially and used without further purification. Non-condensible impurities were removed by several freeze-pump-thaw cycles at liquid nitrogen temperatures. Metal carbonyl vapor pressures ($>10^{-2}$ Torr) were found to be adequate for all present experiments and impurities were negligible as determined by mass spectrometry.

III. RESULTS

Dissociative electron attachment processes were observed for all the transition metal carbonyls studied. Typical trapped ion data for formation of $Cr(CO)_5^-$ is shown in Fig. 3. Similar results were obtained for $Fe(CO)_4^-$, $Mo(CO)_5^-$, $W(CO)_5^-$, $V(CO)_5^-$ and $Ni(CO)_3^-$.

Electron attachment rate constants were measured in the same way as previously described for SF_6[1] and fluorinated hydrocarbons.[2] Shortly after termination of the electron beam pulse the curve in Fig. 1 can be represented by an exponential, Eq. 2.

$$[M^-] = [M^-]_\infty \{1 - \exp(-k_{app}[M]t)\} , \qquad (2)$$

where $[M^-]_\infty$ is the anion abundance at long times and k_{app} is the apparent bimolecular rate constant. The initial period of slower dissociative electron attachment is followed by rapid $M(CO)_n^-$ formation with limiting slope, k_{app} (Fig. 4). Since the rate limiting step at low pressures in relaxation of the electron energy distribution,[2] k_{app} is found to decrease with increasing trapping voltage. Figure 5 illustrates this for $Cr(CO)_5^-$ and $Fe(CO)_4^-$. The apparent attachment rate varies with trapping voltage. Since trapped electrons have energies from 0 eV to 0.9 V_t, increasing the trapping voltage increases the average electron energy. The curve for formation of $Fe(CO)_4^-$ agrees very well with that obtained by Compton and Stockdale[10] (see Figure 5b). A trapping voltage -1.5 eV was chosen for all further experiments, corresponding to electron energies in the range 0-1.3 eV.

FIGURE 3. Typical trapped ion data for dissociative electron attachment to $Cr(CO)_6$. The trap is fitted with electrons by a 3 ms electron beam pulse. $Cr(CO)_6$ pressure is 2.7×10^{-8} Torr.

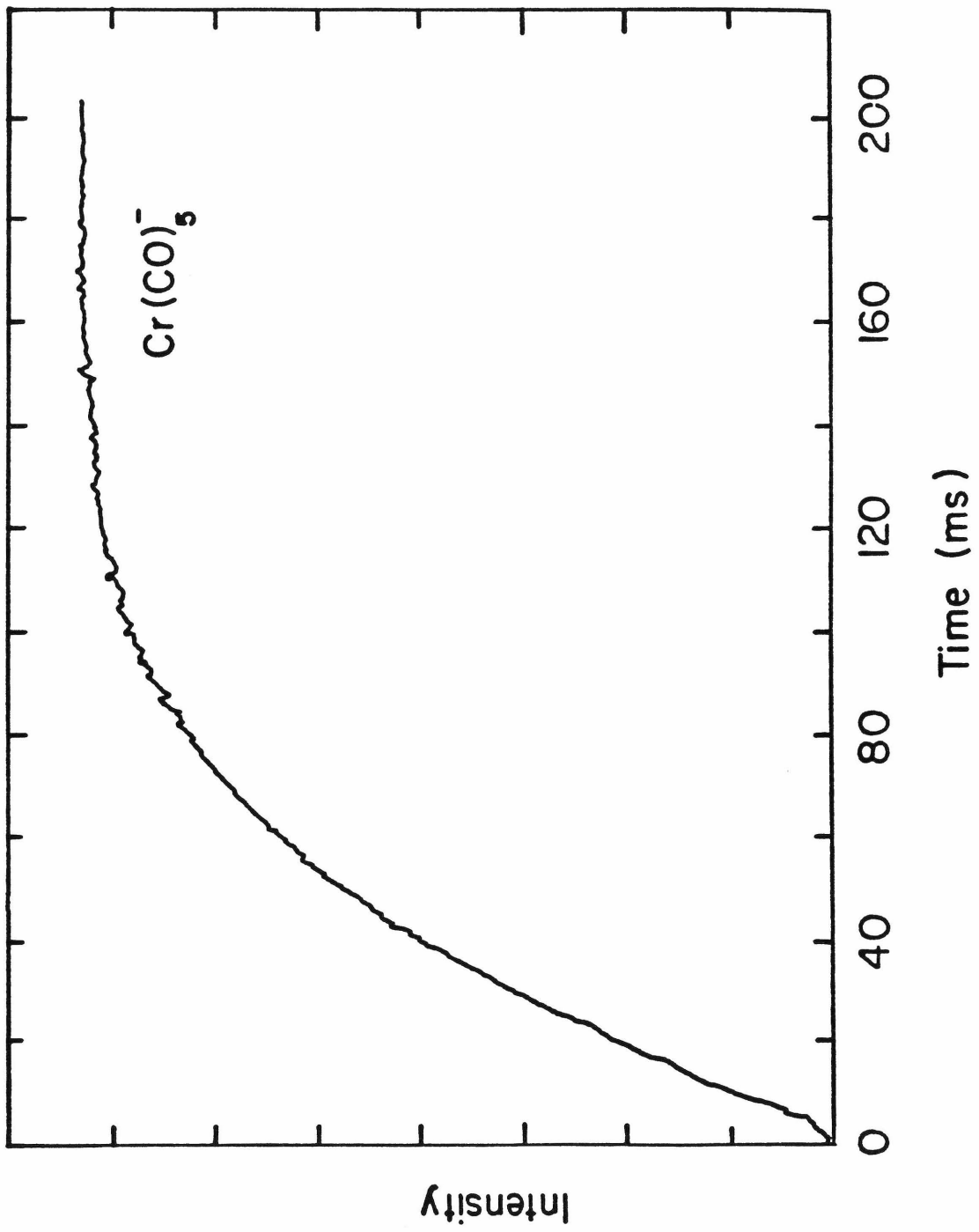
Cr(CO)$_5^-$
Intensity
0
40
80
120
160
200
Time (ms)

FIGURE 4. Effect of trapping voltage on dissociative electron attachment to $Fe(CO)_5$. Trapping voltages are negative for negative ions. $[Fe(CO)_4^-]_\infty$ is the ion abundance of $Fe(CO)_4^-$ when all the electrons have been attached and is equal to the number of scattered electrons produced during the electron beam pulse.

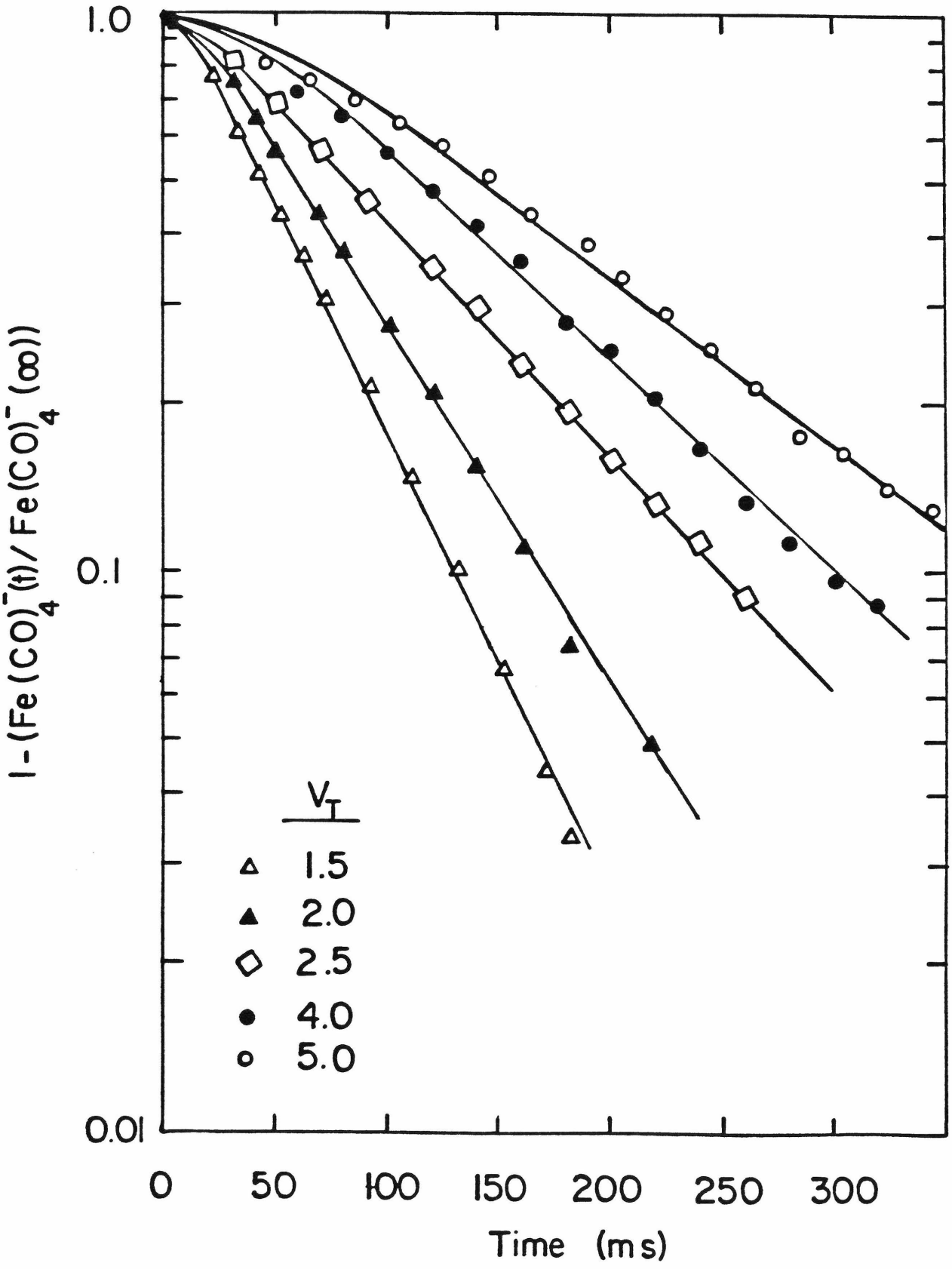
1.0
0.1
0.01
0
50
100
150
200
250
300
Time (ms)
1-(Fe(CO)4-(t)/Fe(CO)4-(∞))
VT
1.5
2.0
2.5
4.0
5.0

FIGURE 5a. The effect of trapping voltage on the low pressure dissociative attachment rate constant, k_{app}, for $Cr(CO)_5^-$ and $Fe(CO)_4^-$. Energy of scattered electrons varies as a function of trapping voltages V_t, thus the indices represent ion formation as a function of electron energy (lower scale).

FIGURE 5b. Yield of $Fe(CO)_4^-$ and $Fe(CO)_3^-$ as a function of electron energy. Data from reference 10.

a.

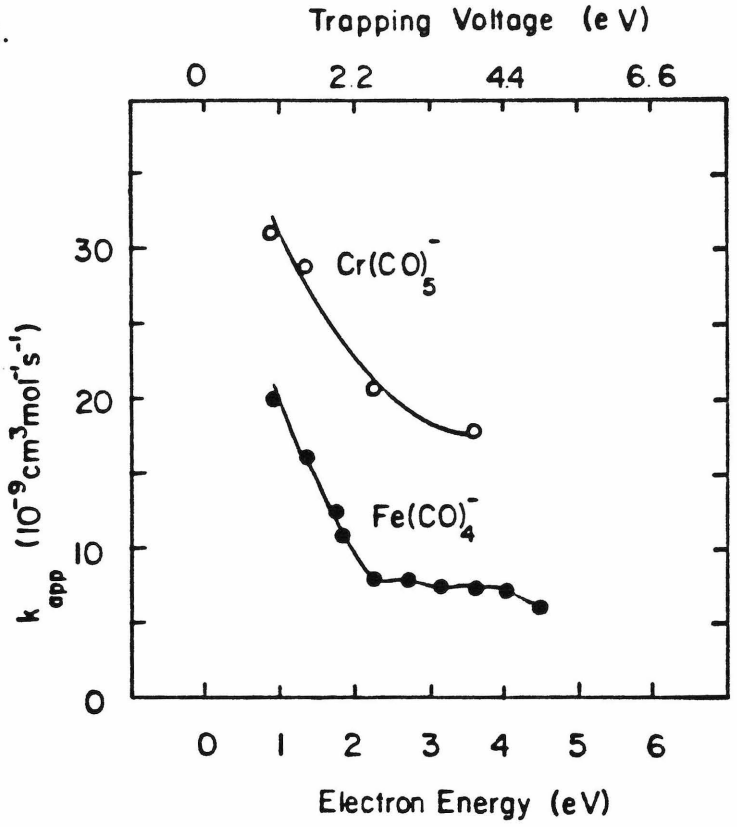
Trapping Voltage (e V)
0
2.2
4.4
6.6
30
20
10
0
k_{app} (10^{-9} cm^3 mol^{-1} s^{-1})
$Cr(CO)_5^-$
$Fe(CO)_4^-$
0 1 2 3 4 5 6
Electron Energy (eV)

b.

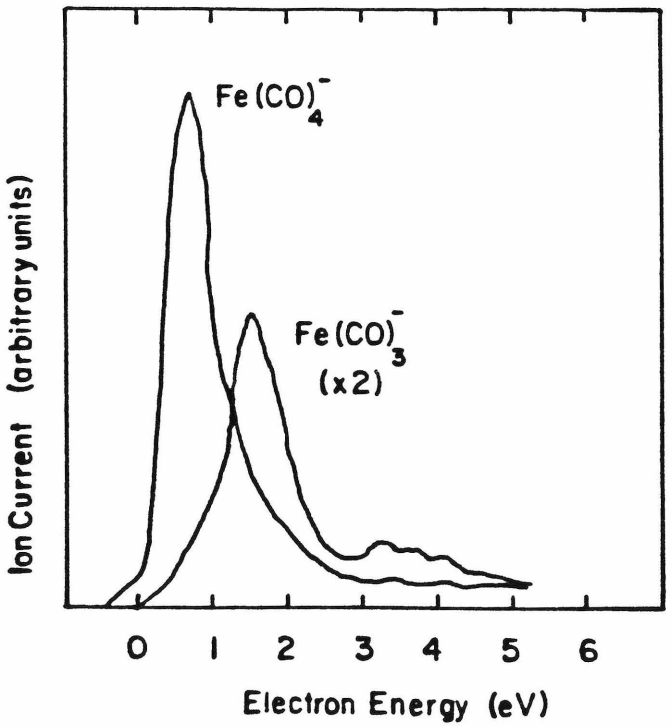
$Fe(CO)_4^-$
$Fe(CO)_3^-$
(x2)
Ion Current (arbitrary units)
0 1 2 3 4 5 6
Electron Energy (eV)

The attachment rates vary linearly with pressure of metal carbonyl up to 10^{-7} Torr (Fig. 6). The slope of Fig. 6 directly yields the apparent electron attachment rate constant and shows that it is independent of the pressure of the metal carbonyl. The apparent attachment rate does, however, vary with the pressure of added CO_2 buffer gas. To measure high pressure attachment rates, increasing pressures of CO_2 were added to 3×10^{-8} Torr metal carbonyl. These results are shown for all of the metal carbonyls in Figs. 7a-f. Attachment rates are proportional to CO_2 pressure until the high pressure limit is reached. From the slope of the linear portion of each curve a rate constant for the apparent relaxation of 0-1.3 eV electrons by CO_2 can be calculated. These values are given in Table 1 along with the high pressure limits for a relaxed thermal electron distribution.

IV. DISCUSSION

With the exception of $V(CO)_6$, the high pressure dissociative attachment rate constants are all in the same range, from 1×10^{-7} to 3×10^{-7} cm^3 $molecule^{-1}$ s^{-1}. This is in good agreement with the observations of Compton and Stockdale[10] that very large ion currents were obtained for $Fe(CO)_4^-$, $Fe(CO)_3^-$ and $Ni(CO)_3^-$ which were comparable to SF_6^- currents under equivalent conditions. The rate constant for SF_6^- is also in the above range.[13] The reason that dissociative electron attachment rates for formation of $V(CO)_5^-$ and $V(CO)_4^-$ are much lower can be attributed to the fact that the molecular anion is stable[8] and consequently the lifetime of the intermediate $V(CO)_6^{-*}$ is likely to be much

TABLE I.

Ion	k_{app} [a]	k_m [b]	k_{CO_2} [b]
$V(CO)_5^-$	5.7×10^{-8}	1.6×10^{-8}	2.0×10^{-10}
$V(CO)_4^-$	4.0×10^{-8}	2.2×10^{-8}	5.7×10^{-10}
$Cr(CO)_5^-$	3.2×10^{-7}	2.8×10^{-8}	9.1×10^{-10}
$Fe(CO)_4^-$	2.0×10^{-7}	1.1×10^{-8}	3.1×10^{-10}
$Fe(CO)_3^-$	1.7×10^{-7}	5.5×10^{-8}	3.2×10^{-8}
$Ni(CO)_3^-$	2.0×10^{-7}	1.8×10^{-8}	3.1×10^{-10}
$Mo(CO)_5^-$	1.3×10^{-7}	2.0×10^{-8}	3.1×10^{-10}
$W(CO)_5^-$	1.2×10^{-7}	2.0×10^{-8}	1.4×10^{-11}

[a] All rate constant units are cm^3 $molecule^{-1}$ s^{-1}.

[b] k_m = metal carbonyl electron capture rate constant;
k_{CO_2} = apparent CO_2 thermalization rate constant.

FIGURE 6. Dissociative attachment rates as a function of $Fe(CO)_5$ pressure with no CO_2 present.

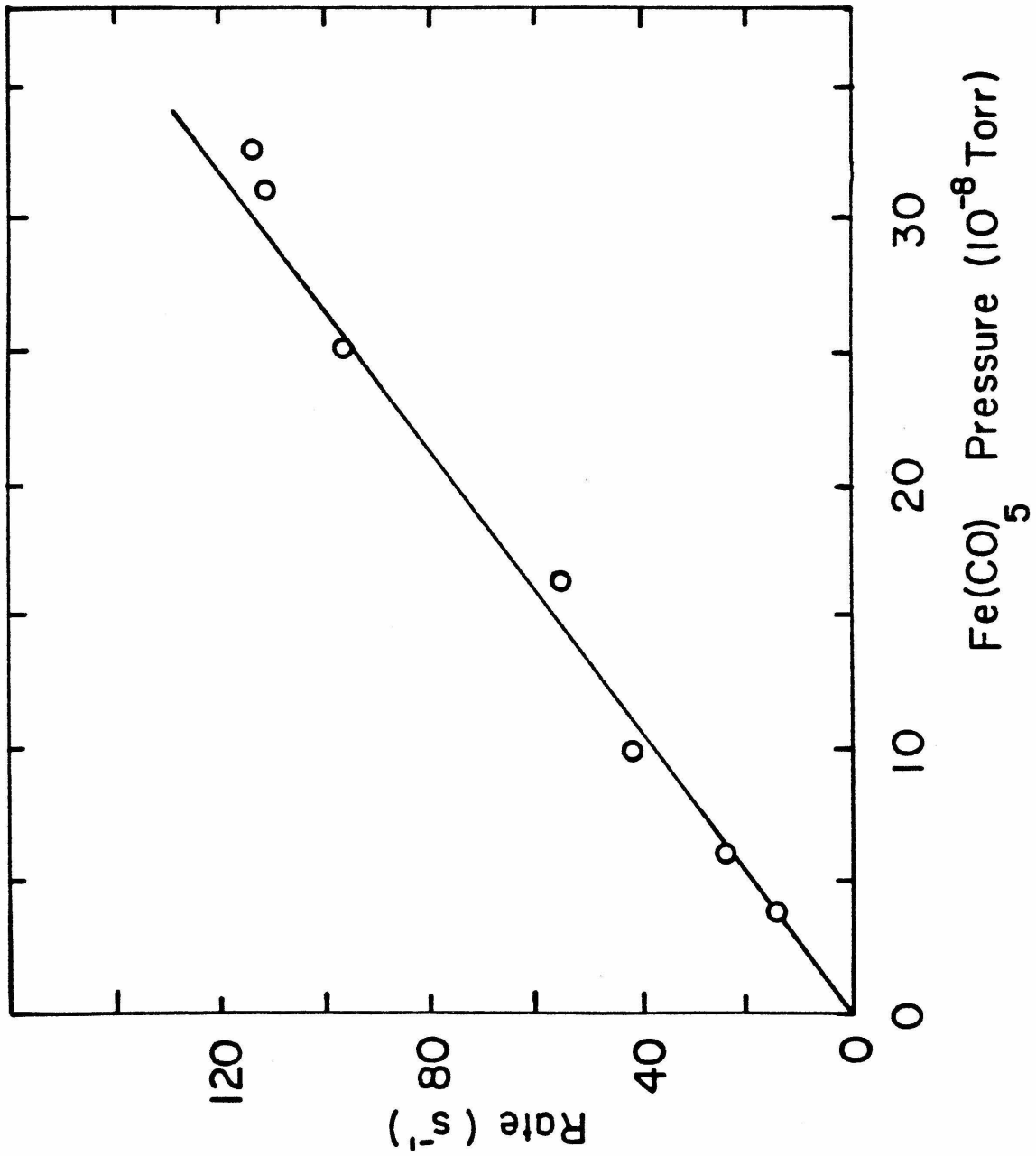
Rate (s^{-1})
0
40
80
120
0
10
20
30
$Fe(CO)_5$ Pressure (10^{-8} Torr)

FIGURE 7. Dissociative electron attachment rate constants as a function of CO_2 pressure for a) $V(CO)_6$, b) $Cr(CO)_6$, c) $Fe(CO)_5$, d) $Ni(CO)_4$, e) $Mo(CO)_6$ and f) $W(CO)_6$.

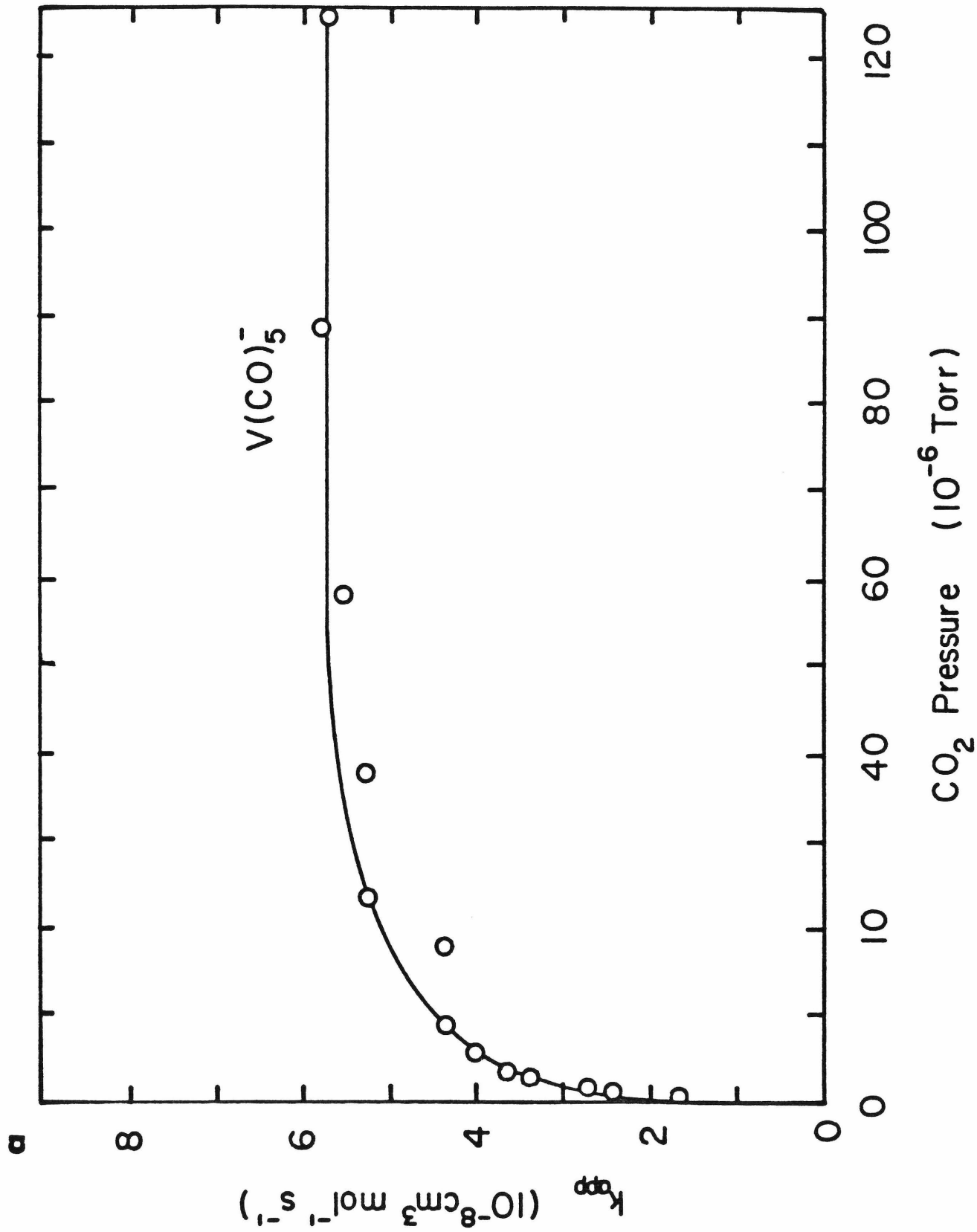
$V(CO)_5^-$
k_{app} (10^{-8} cm^3 mol^{-1} s^{-1})
CO_2 Pressure (10^{-6} Torr)
0
2
4
6
8
0
10
40
60
80
100
120

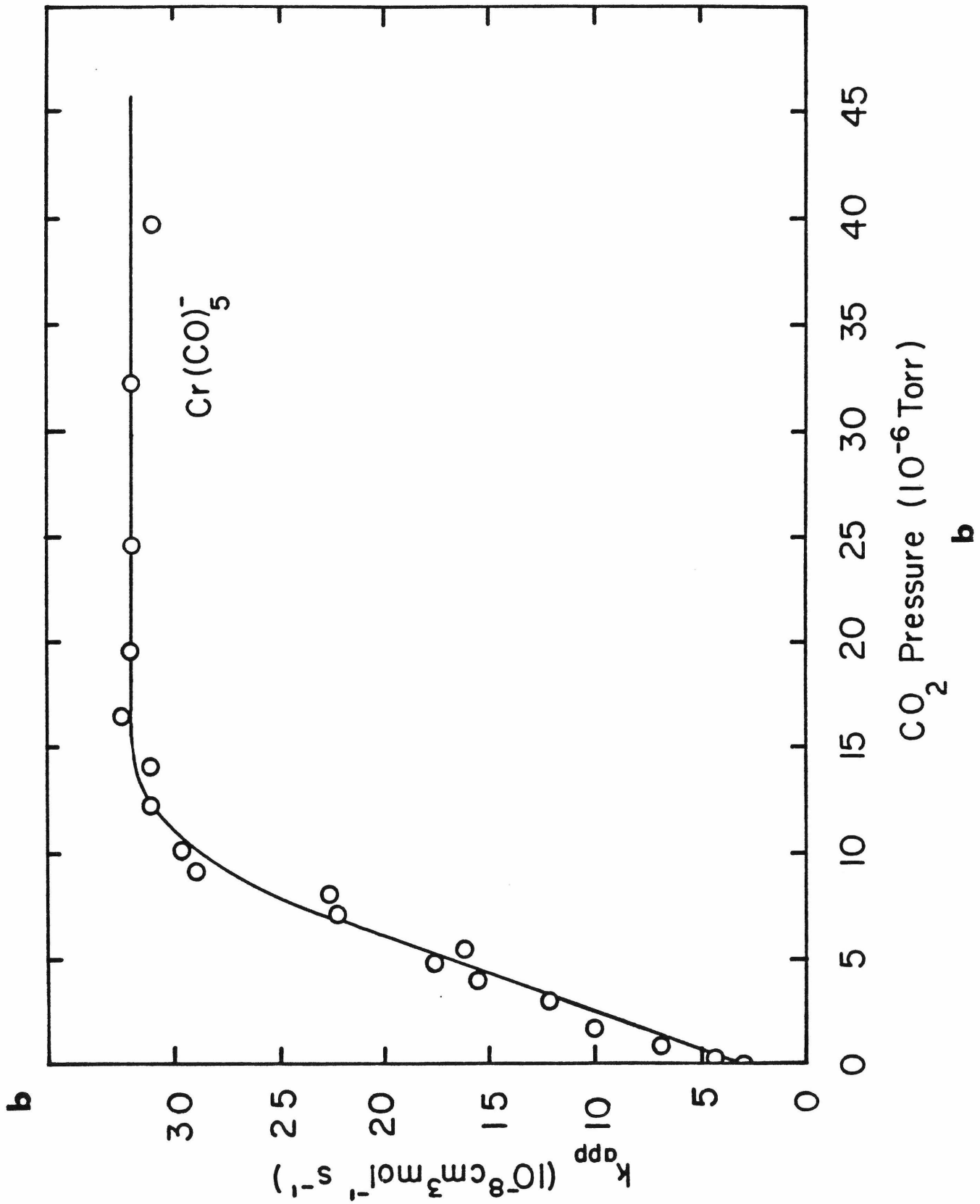
b
k_{app} (10^{-8} cm^3 mol^{-1} s^{-1})
0
5
10
15
20
25
30
$Cr(CO)_5^-$
0
5
10
15
20
25
30
35
40
45
CO_2 Pressure (10^{-6} Torr)
b

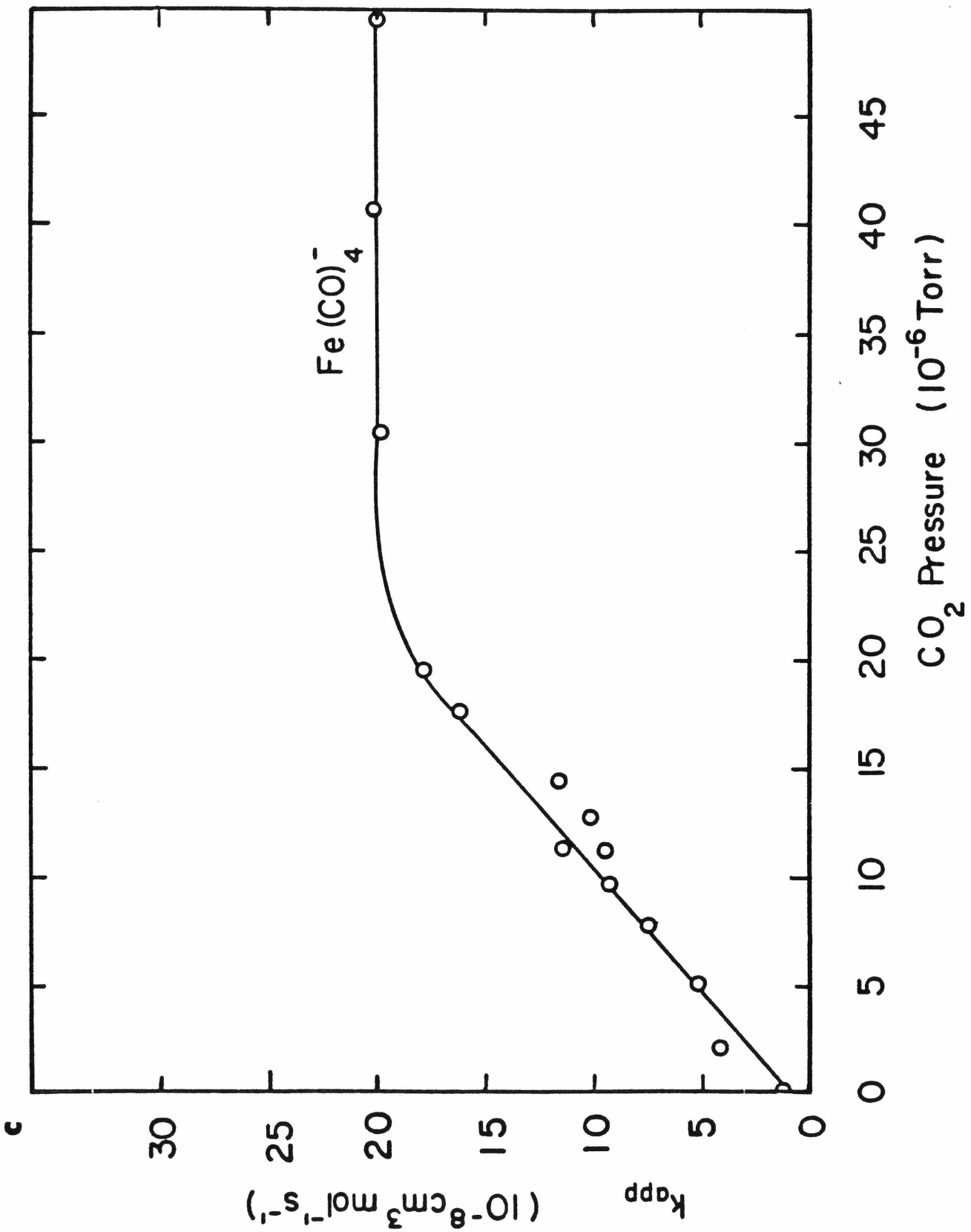
Fe(CO)$_4^-$
k_{app} (10^{-8}cm^3 mol^{-1}s^{-1})
CO_2 Pressure (10^{-6}Torr)
0
5
10
15
20
25
30
35
40
45

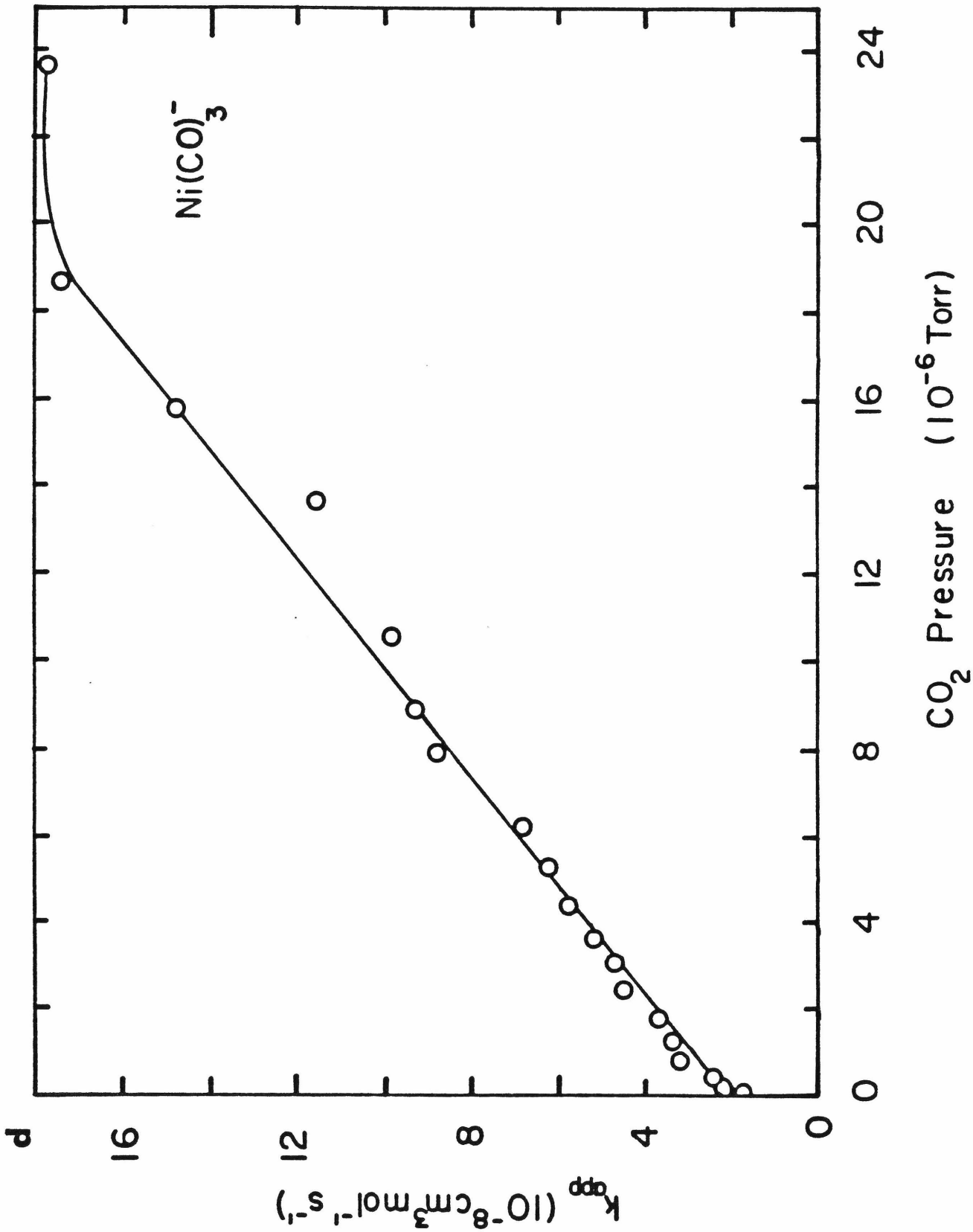
$Ni(CO)_3^-$
k_{app} (10^{-8} cm^3 mol^{-1} s^{-1})
CO_2 Pressure (10^{-6} Torr)
0
4
8
12
16
20
24

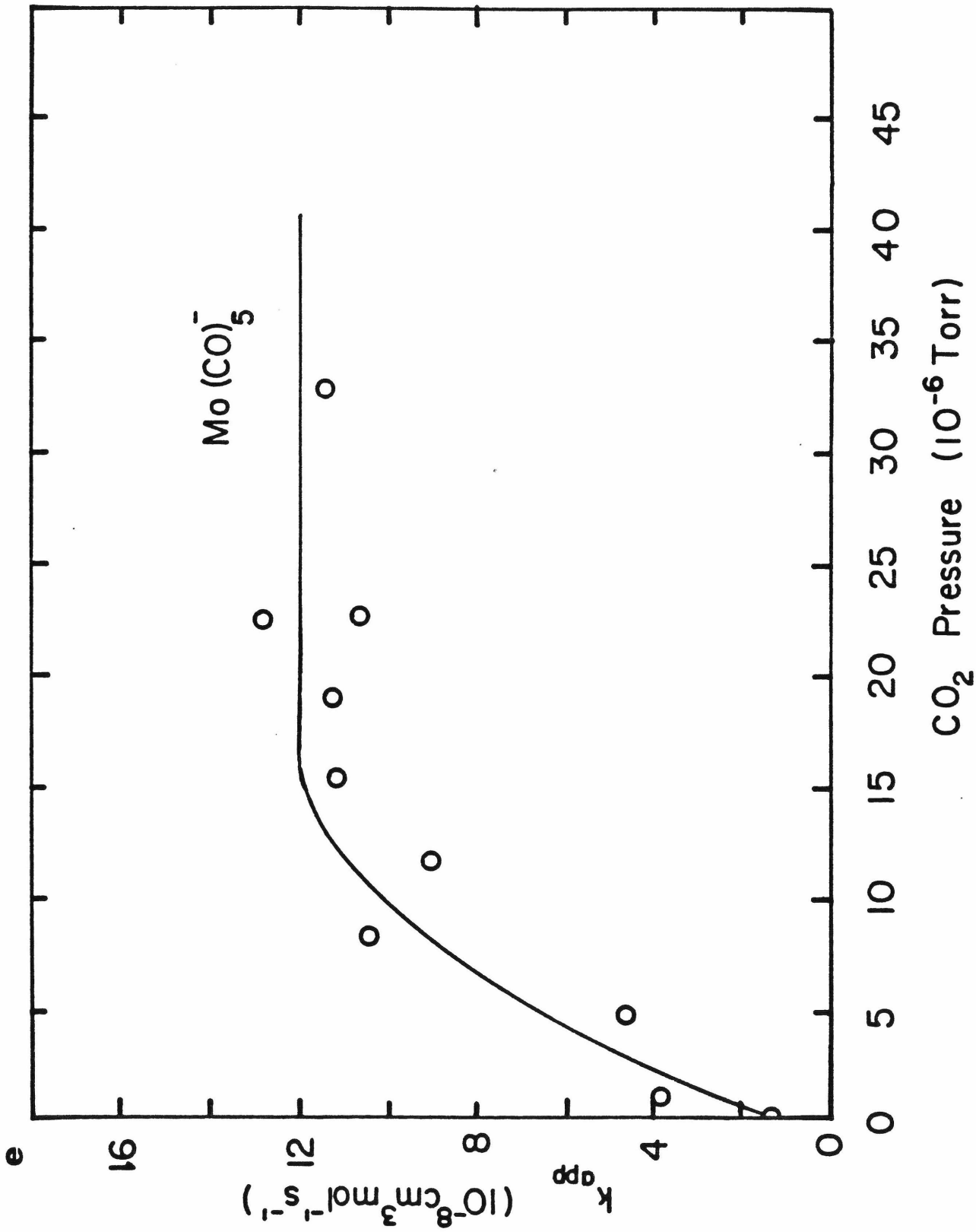
e
16
12
8
4
0
k_{app} (10^{-8} cm^3 mol^{-1} s^{-1})
$Mo(CO)_5^-$
0
5
10
15
20
25
30
35
40
45
CO_2 Pressure (10^{-6} Torr)

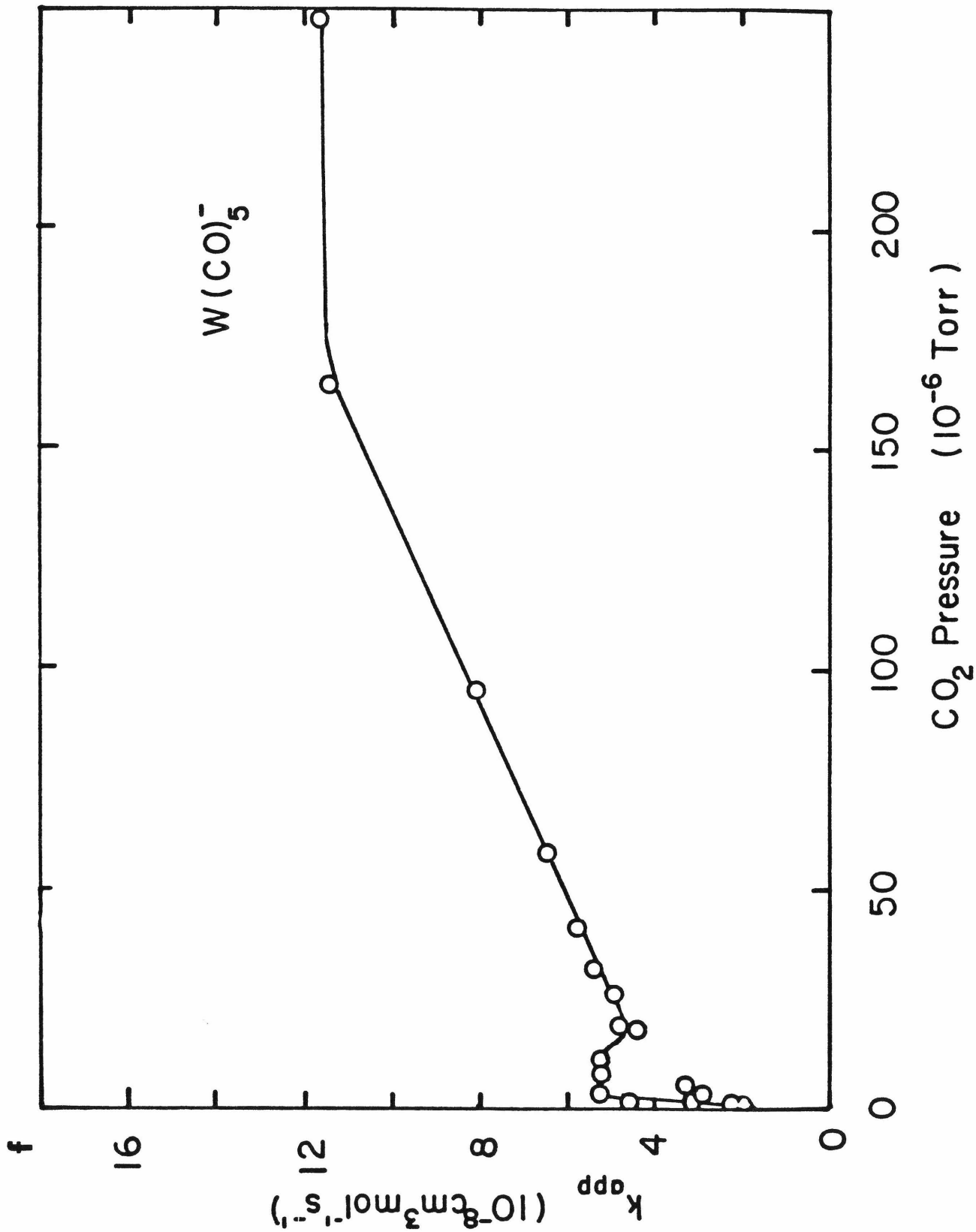
W(CO)$_5^-$
k_{app} (10^{-8} cm^3 mol^{-1} s^{-1})
CO_2 Pressure (10^{-6} Torr)
0
4
8
12
16
0
50
100
150
200

longer than for the remaining carbonyls where the extra electron occupies an antibonding orbital. This suggests that the attachment rate reflects the stability of the molecular anion with regard to dissociation.

The results in Table 1 also show that CO_2 moderates the electron energy with an apparent range of rate constants varying from 1×10^{-11} to 3.2×10^{-8} cm^3 $molecule^{-1}$ s^{-1}. This suggests that the apparent rate of thermalizing electrons is not independent of the species used to monitor the relaxation process. This is not unreasonable since each dissociative electron capture process has a specific and distinc dependence on electron energy. The maximum cross section for each ion is different and occurs at different electron energies with varying peak widths. It is to be expected, therefore, that removal of electrons in a particular energy range by molecules exhibiting different cross sections appears to change the relaxation rate of CO_2. Thus if the cross-section peak is sharp and occurs at low energies, e.g., CCl_4 (which has a sharp dissociative attachment peak at thermal energies[14]) the apparent relaxation rate of CO_2 increases. For example, in CCl_4 the apparent rate of thermalization of electrons is as high as 5.8 a 10^{-9} cm^3 mol^{-1} s^{-1}. Also if the maximum dissociative attachment cross section occurs at an energy significantly closer to the peak of the initial electron energy distribution, the relaxation rate of CO_2 can appear much higher since little or no relaxation is required before dissociation occurs.

The inherent CO_2 relaxation rate does not change but the use of anion formation as a monitor of relaxation rate provides an imprecise measurement. Thus Warman and Sauer[4] were correct when they noted that CCl_4 possibly distorts the CO_2 thermalization due to rapid removal

of electrons at the low end of the energy spectrum. The energy dependence of the cross section is critical in using a specific dissociative electron capture process to monitor rela ation by CO_2. This is especially important in the transition metal carbonyl systems as in CCl_4, because of the very large cross sections for electron attachment.

As an example of the above discussion it can be seen that $Fe(CO)_4^-$ is formed with electrons in the range 0-3 eV (Fig. 5b). The apparent CO_2 relaxation rate constant is 3.1×10^{-10} cm^3 molecule^{-1} s^{-1}. $Fe(CO)_3^-$, however, is formed at higher energies and the apparent rate of thermalization of electrons by both CO_2 and by $Fe(CO)_5$ alone become almost comparable to the electron attachment rate observed at high CO_2 pressures. That is, very little or no thermalization is required to react a 0-1.3 eV electron distribution with $Fe(CO)_5$ in order to lose two CO ligands. This is in good agreement with observations[10] that onset of $Fe(CO)_3^-$ formation occurs at zero electron energy but continues rising until a maximum is reached at ~ 1.3 eV. Thus the exact effect of the anion involved on the relaxation rate depends on the specific ion involved and the particular electron energy range required for its formation.

It is noted, however, that the rate constants for CO_2 thermalization of electrons obtained with some of the metal carbonyls do correlate well with the values calculated from Christophorou's[3] studies on thermalization times as a function of mean electron energy. In fact, the values of 3×10^{-10} cm^3 molecule^{-1} s^{-1} obtained when $Fe(CO)_4^-$, $Mo(CO)_5^-$ and $Ni(CO)_3^-$ were the monitoring species agree very well with the 3.8×10^{-10} cm^3 molecule^{-1} s^{-1} calculated for an average electron

energy of 0.7 eV. This suggests that very little distortion of relaxation rates is occurring in these systems, while $Cr(CO)_5^-$ and $W(CO)_5^-$ have fairly large effects. To understand the reasons for this it would be valuable to examine the dependence of these cross sections as a function of electron energy. This would also be useful in explaining the plateau observed in Figs. 7e and 7f for k_{app} as a function of CO_2 pressure, since this may be attributed to the presence of two peaks (or a shoulder and a peak) in the yield of those ions as a function of electron energy.

V. CONCLUSION

The high dissociative electron attachment rate constants for the transition metal carbonyls appear to reflect the stability of the molecular anion to dissociation. Results suggest that the molecular anions of $Cr(CO)_6$, $Fe(CO)_5$, $Ni(CO)_4$, $Mo(CO)_6$ and $W(CO)_6$ have approximately the same stability, although a trend toward increasing stability is observed with increasing size of the metal. As mentioned earlier, $V(CO)_6^-$ has been observed mass spectroscopically in very small quantities. The rate constants are all very close to the maximum (s-wave) thermal attachment rate constant of 5×10^{-7} cm^3 $molecule^{-1}$ s^{-1} at 298 K.[14]

The apparent CO_2 relaxation rate is found to change with varying anions. Thus it is concluded that monitoring anion formation provides an imprecise measurement of the CO_2 relaxation rate. This is probably due to the rapid removal of electrons within a particular energy range, and is particularly true for transition metal carbonyls since they have

very high electron attachment rates. Detailed investigations of the formation of metal carbonyl ions as a function of electron energy would help clarify these results.

References

[1]M. S. Foster and J. L. Beauchamp, Chem. Phys. Lett. 31(3), 482 (1975).

[2]R. L. Woodin, M. S. Foster and J. L. Beauchamp, J. Chem. Phys. 72(7), 432 (1980).

[3]L. G. Christophorou, K. S. Gant and J. K. Baird, Chem. Phys. Lett. 30(1), 104 (1975).

[4]J. M. Warman and M. C. Sauer, Jr., J. Chem. Phys. 62(5), 1971 (1975).

[5]G. J. Schultz in "Principles of Laser Plasmas", G. Bekefe, ed., John Wiley and Sons, N.Y. (1976).

[6]R. L. Sullivan and R. N. Kiser, J. Chem. Phys. 49, 1978 (1968).

[7]R. N. Kiser, R. L. Sullivan and M. S. Lupin, Anal. Chem. 41, 1958 (1969).

[8]R. E. Winters and R. N. Kiser, J. Chem. Phys. 44, 1964 (1966).

[9]R. L. Sullivan, M. S. Lupin and R. W. Kiser, Chem. Commun. 655 (1969).

[10]R. N. Compton and J. A. D. Stockdale, Int. J. Mass Spectrom. Ion Phys. 22, 51 (1976).

[11]P. C. Engelking and W. C. Lineberger, J. Am. Chem. Soc., 101, 5569 (1979).

[12]T. B. McMahon and J. L. Beauchamp, Rev. Sci. Inst. 43(3), 509 (1972).

[13]L. G. Christophorou and J. A. D. Stockdale, J. Chem. Phys. 48(5), 1956 (1968).

[14]R. P. Blauenstein and L. G. Christophorou, J. Chem. Phys. 49(4), 1526 (1968).

References (continued)

[15]L. G. Christophorou and R. P. Blauenstein, Chem. Phys. Lett. 12(1), 173 (1971).